This is to certify that the
dissertation entitled

FORWARD AND INVERSE PROBLEMS IN NONINVASIVE IMAGING TECHNIQUES

presented by

YIMING DENG

has been accepted towards fulfillment
of the requirements for the

Ph.D. degree in Electrical Engineering

Major Professor's Signature

08/24/2009

Date

# FORWARD AND INVERSE PROBLEMS IN NONINVASIVE IMAGING TECHNIQUES

By

Yiming Deng

A DISSERTATION

Submitted to
Michigan State University
in partial fulfillment of the requirements
for the degree of

DOCTOR OF PHILOSOPHY

Electrical Engineering

2009

# ABSTRACT

## FORWARD AND INVERSE PROBLEMS IN NONINVASIVE IMAGING TECHNIQUES

By

Yiming Deng

Noninvasive imaging techniques are used in both engineering and clinical fields to determine the state or internal conditions of structures and human body on the basis of information contained in measured signals and images without the use of invasive approaches. Development of the forward and inverse models for non-invasive imaging not only helps to understand the physics and biological processes better, but also enables development of efficient, low-cost and accurate algorithms for early detection and diagnosis of anomalies. Recent developments in two noninvasive imaging applications, Electromagnetic imaging including Magneto Optic (MO) and Giant Magneto Resistive (GMR) methods and Positron Emission Tomography (PET) imaging in biomedical field are covered in this dissertation. For MO and GMR Imaging, the element free forward model as well as fast image reconstruction and automated classification approaches are presented. In biomedical imaging application, the PET modality is described and in particular the degradation of PET images due to the patients' thoracic (including cardiac and respiratory) motion is addressed. In contrast to the other approaches for correcting motion artifacts in the image space, an innovative framework for motion correction in the raw projection space (Sinogram) is introduced based on the forward Monte Carlo model.

To my wife Dr. Xin Liu, daughter Joanna and parents

# ACKNOWLEDGEMENTS

I would like to express my sincere appreciation to my major advisor and mentor, Dr. Lalita Udpa, for her guidance, support, and encouragement throughout my Ph.D. study She also encouraged me in teaching and other academic activities. Dr. Lalita Udpa inspires me so much through her own passion in research, excellence in teaching and professionalism in service.

I would like to express my sincere gratitude and thanks to Dr. Satish S. Udpa for his continuous support and guidance as my professor within the NDEL and as the Dean in the College of Engineering. I would like to thank Dr. Kevin L. Berger for his invaluable help during my biomedical research and continuous support during my PhD study. I would like to thank Dr. David C. Zhu for his guidance in medical imaging research and encouragement in my professional development. I would like to thank Dr. Robert J. McGough for his support and help; especially his comprehensive and interesting Medical Imaging and Acoustics classes which help me discover my passion in medical imaging and choose my future research areas afterwards. I would also like to thank Dr. V. Mandrekar for being my committee member, and providing valuable help in completing my study.

I would particularly like to thank my wife and colleague, Dr. Xin Liu for her numerous support, encouragement and love. Finally, I would like to thank my beloved parents, friends, Ms. Linda Clifford and the other colleagues of NDEL. Thank you!

# TABLE OF CONTENTS

# LIST OF TABLES

# LIST OF FIGURES

# CHAPTER 1. INTRODUCTION

## 1.1 Motivation & Objectives

In the past decades, there has been a tremendous increase in interest in imaging, the formation of images, and related physics, image processing and analysis for both engineering and clinical applications. Due to the inter-disciplinary or multi-disciplinary research fields that imaging covers, there are many unsolved problems. Numerous imaging methodologies have been developed, viz, medical imaging, electromagnetic imaging, molecular imaging, optical imaging, geophysical imaging, etc. based on the technologies and underlying imaging physics. Imaging techniques can also be simply divided into two categories: invasive and noninvasive methods. Noninvasive imaging methods reveal the internal conditions of object of interest without destroying or cutting/opening the test object. Such techniques are widely used in both engineering and medicine where the objects are structures/materials or in-vivo subjects, like human body. To understand the noninvasive imaging better, both the forward models that simulate the image formation and the inverse techniques that process and analyze the imaging data are crucial. This dissertation comprises two parts, electromagnetic (EM) imaging for metallic aircraft body inspection and positron emission tomography (PET) imaging for in-vivo human subject imaging and diagnosis.

The first application is related to EM methods for nondestructive inspection of airframe structures. Eddy current (EC) testing is the most widely used method for aluminum structures. However it is limited by skin depth in detecting defects in multi-layered complex structures. Electromagnetic noninvasive imaging techniques in this dissertation, namely, magneto optic (MO) imaging and giant magneto resistive (GMR) imaging offer much higher sensitivity that allow detection of defects located deep in the test object. MO imaging is a technology, based in part on the Faraday rotation effect that uses eddy current induction techniques along with a MO sensor, which generates real-time analog images of the magnetic fields associated with induced eddy currents interactions with structural anomalies. GMR imaging sensor is unipolar in nature and is sensitive to the magnetic fields along the "easy" axis of the sensor. The local magnetic fields measured by the GMR sensors are converted into electric voltages, which are also associated with the induced current interactions with structural anomalies. However, MO imaging measurement suffers severe background noise and lack of quantification and automated analysis. GMR imaging data suffers from relative lower signal to noise ratio due to lower frequencies applied for overcoming the skin depth effect; and lack of systems and sensors configuration optimization due to little knowledge of actual electromagnetic field distribution and sensor-field interaction. Positron Emission Tomography (PET) imaging is both a clinical and a research imaging modality first introduced in 1970s. However, patient motion, including body movement, head movement and thoracic motion due to respiratory and cardiac cycles, is a major source of artifacts in PET imaging. In the motion-corrupted PET imaging data, various phases of motion information are

superposed and make the reconstructed images blurred. The motivation for motion correction was not initiated, however, until recently when the spatial resolution of PET scanners was greatly improved. The motion-corrupted blurring is relatively larger and unbearable in the new generation of PET scanners. Also, the clinical applications of PET have been emphasized more in thorax scans and tumor detection, in contrast to the early research of the brain. The effects of the thoracic motion, including cardiac and respiratory motion, are much more severe than the head movement. Current compensation algorithms are performed after or during image reconstruction process, e.g. multiple frame acquisition, gating methods, and image registration. Also due to the trends in the combination of PET and Computed Tomography (CT), the correction of anatomical motion in PET is essential for the image fusion of PET and CT modalities and accurate attenuation corrections for PET from CT acquisition.

The principle objective of this dissertation is to develop forward mathematical models for noninvasive imaging and also develop inversion techniques and image processing methods to interpret the measurement and reconstruct the true object accurately. More specifically, in MO and GMR imaging application, a real-time reconstruction and automated image classification approaches are presented. In the PET imaging application, the specific aim is to develop a motion correction technique based on the sinogram data prior to the image reconstruction. In order to study the effects of motion on PET image, we need to develop an accurate and reliable computational model that allows controlled variation of motion due to respiratory and cardiac cycles.

## 1.2 Scope and Organization of the Dissertation

There are nine chapters in this dissertation and is composed two parts. Part I related to noninvasive imaging of engineering structures comprises Chapter 3 to Chapter 5, and is referred to as nondestructive evaluation (NDE). Chapter 1 and Chapter 2 are the introduction and background of the dissertation, including the basic ideas of forward and inverse problems in noninvasive imaging. Chapter 3 presents the fundamentals of electromagnetic imaging including magneto optic and giant magneto resistive imaging principles and challenges. Chapter 4 introduces the forward finite element models for electromagnetic imaging techniques. System optimization and sensor design are also investigated based on the numerical models. Chapter 5 discusses image processing, characterization, classification and enhancement algorithms for inversion techniques. Part II comprises Chapter 6 to Chapter 8 is devoted to biomedical imaging, particularly PET. Chapters 6 to 8 discusses the biomedical imaging application, namely, positron emission tomography imaging. Its history, physical principles, instrumentation and challenges are discussed in Chapter 6. Chapter 7 presents the forward 2D and 3D emission tomography models. The patient motion is also considered and introduced in the models in this Chapter. Chapter 8 proposes the innovative motion correction methodology in the projection space, i.e. sinogram. The advantage and disadvantage of this method are discussed. Major accomplishments and future work are summarized in the last chapter, Chapter 9, followed by the Appendix and References.

# CHAPTER 2. NONINVASIVE IMAGING

## 2.1 Introduction

Imaging, simply speaking, is the formation of images. Imaging science is concerned with the formation, collection, duplication, analysis, modification, and visualization of images.

A typical NDE/Noninvasive imaging system is illustrated in Figure 2.1, where the detector/sensor makes measurement on the surface of the test objects, i.e. structures and human body. Noninvasive imaging techniques are used in both engineering and medicine to determine the state or internal conditions of the objects on the basis of information contained in measured images or signals.

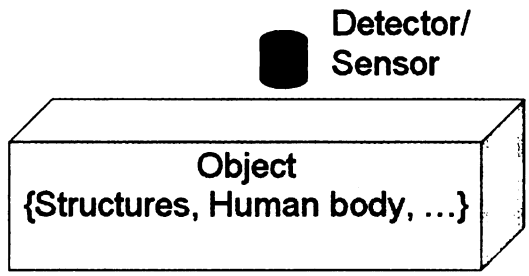


Figure 2.1 Noninvasive imaging techniques

Noninvasive imaging is an interdisciplinary research field that combines methodologies from Electrical Engineering, Biomedical Engineering, Medicine, Radiology and Statistics. This dissertation covers two major research fields: 1)

electromagnetic imaging methods that deal with the materials and structures, commonly referred to as NDE, and 2) biomedical imaging of human body or small animals. Although the physical principles for these imaging techniques are different, they can be unified by a common goal: both of them search for solutions of inverse problems from the observed images/signals. A brief description of the theory and applications of various imaging modalities are in the following sections of this Chapter.

## 2.2 Electromagnetic imaging

EM imaging is essential for detecting anomalies or defects in conducting materials based on the electromagnetic principles. To understand EM imaging techniques, this section is organized as following: the fundamental of electromagnetism is first introduced; then the introduction of image processing is briefly discussed followed by a general approach to processing and understanding the electromagnetic images. The details of two electromagnetic imaging techniques, MO Imaging and GMR imaging, are discussed in Chapter 3.

A generic electromagnetic (EM) imaging system is shown in Figure 2.2. The excitation transducer couples the EM energy into the test objects. The receiving sensors measure the response of energy/material interaction. This is the forward imaging procedure. Different EM sensors are used for different applications, e.g. eddy current, microwave imaging, Terahertz imaging, etc. After acquiring and storing the

EM images, those data are passed through the inversion techniques, which involve the object reconstruction.

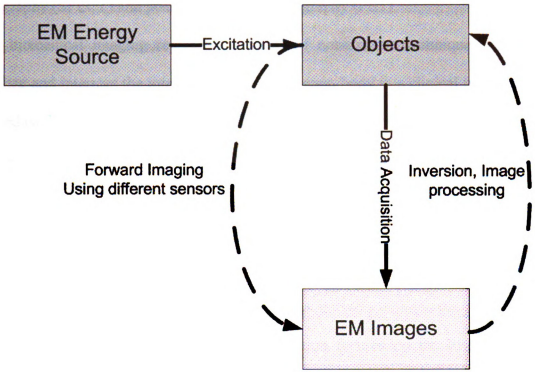


Figure 2.2 A generic EM imaging system

## 2.3 Biomedical imaging

Biomedical imaging is the imaging of human body (or parts of body) for clinical purposes and is essential for medical diagnosis procedures to detect and treat diseases. The different modes of generating biomedical images are referred to as modalities and each modality is characterized by its own form of energy, data acquisition process, physical principles of generating images, instruments and applications in medicine. Commonly used biomedical imaging modalities include: conventional radiography

such as X-rays, computed tomography (CT), ultrasound, magnetic resonance imaging (MRI) and nuclear medicine applications such as single photon emission computed tomography (SPECT) and positron emission tomography (PET).

Thus biomedical imaging represents a series of noninvasive techniques that can visualize and interpret the internal condition of human body in a clinical perspective. Biomedical imaging is in some restricted mathematical sense seen as the solution of inverse problems because the internal properties of human body is evaluated by from the observed signals or images using different modalities. More introduction of biomedical imaging can be found in Webb's book [1].

### 2.3.1 Nuclear Medicine Imaging

Biomedical imaging application in this dissertation focuses on the PET imaging, which is one of the nuclear medicine imaging modalities. In contrast to the conventional planar X-ray imaging, CT, Ultrasound and MRI, nuclear medicine imaging techniques focus on the distribution of radiopharmaceuticals injected or ingested into the body and physiologic or metabolic interactions between the radioactive compounds and living tissues are imaged. These "radiopharmaceuticals", also termed radiotracers or radioisotopes, are compounds consisting of a chemical substrate linked to a radioactive element. The way to introduce radioactive compounds into human body include: inhalation into the lungs, direct injection into the bloodstream, subcutaneous administration or oral administration [1]. The abnormal rate of change at which the radiopharmaceutical accumulates and distributes strongly indicates diseases in some particular tissues, which usually leads to a higher

contrast in the final images for diagnosis and distinguishes diseased from healthy tissue. In nuclear medicine imaging, there are planar projection imaging techniques, e.g. the anger scintillation camera and emission tomography imaging, like PET and SPECT that depict the activity distribution in single cross sections of the subjects.

The nuclear medicine images are typically generated as follows: first, the radioactive compounds undergo decay and the radiation, usually in the form of $\gamma$ rays is detected using a gamma camera. Secondly, rather than using film as in X-ray imaging, scintillation crystal is widely used to convert the energy of the $\gamma$ rays into light. Third, the light photons are converted into electrical signals by photomultiplier tubes (PMT) [1]. The signals are stored and analyzed by computers and the final nuclear medicine images are produced and visualized. Positron emission tomography produces emission images as opposed to transmission images, i.e. X-ray imaging, because the energy of $\gamma$ rays emitted by the radioisotopes from inside the human body. A general schematic of the nuclear medicine imaging system is shown in Figure 2.1 [7] and the schematic for PET system is illustrated in Figure 2.3.

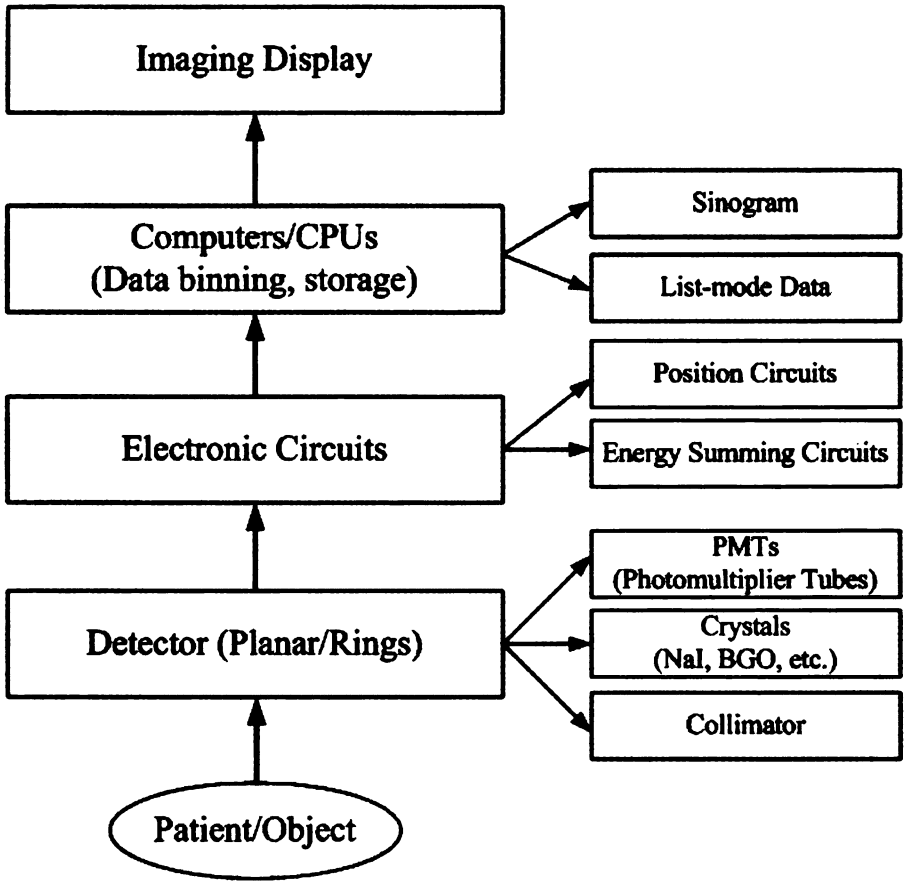


Figure 2.3 Schematic of SPECT/PET imaging system

### 2.3.2 Positron Emission Tomography Imaging

Positron emission tomography imaging belongs to the class of nuclear medicine imaging and provides functional information in patients by imaging the distribution of positron emitting nuclides. In contrast to another nuclear medicine emission tomography, SPECT, the PET system incorporates annihilation coincidence detection (ACD) instead of collimation. The popular nuclides include $^{11}C$, $^{15}O$, $^{18}F$, and $^{13}N$ that are incorporated into metabolically relevant compounds. Although there are many

radiopharmaceuticals suitable for PET imaging, for the applications discussed in this dissertation such as cardiac imaging and lung tumor detection, $^{18}$F-FDG, fluorine-18-fluorodeoxyglucose is more widely adopted. $^{18}$F-FDG is a glucose analog that can differentiate not only malignant tumors from benign lesions, but also differentiate severely hypo-perfused but viable myocardium from scar. More details of PET imaging are discussed in Chapter 6 and Chapter 7.

## 2.4 Forward and inverse problems

The common goal of the noninvasive imaging applications is to interpret the internal condition of the test object. This is referred to as the inverse problems in both Engineering and Medicine. The measurement and image acquisition is referred to as the forward problems. A schematic of the forward and inverse problems in imaging techniques is depicted in Figure 2.4. There are two spaces involved in this loop, one is the subject space and the other is the imaging space. For various imaging techniques, the subject space includes all kinds of subjects with different properties to be imaged; while the imaging space is a set of data, i.e. images, signals that are directly measured or acquired by simulation. After understanding the concepts of subject space and imaging space, it is straightforward to define the forward problems and inverse problems in imaging techniques.

Forward problems involve the procedures and methods that the imaging space data are obtained from test objects with various properties. The procedures can involve direct measurement, forward system modeling and simulation based on underlying

governing equations and so on. On the other hand, the inverse problems are the procedures that the true properties of test objects in subject space are revealed from the imaging space dataset. The concept of inversion techniques is actually very broad in imaging, which includes image reconstruction, image classification, pattern recognition, image visualization, etc. As we can see from Figure 2.4, the forward and inverse procedures are crucial in imaging techniques because they are the bridges that connect the test object space and the imaging space.

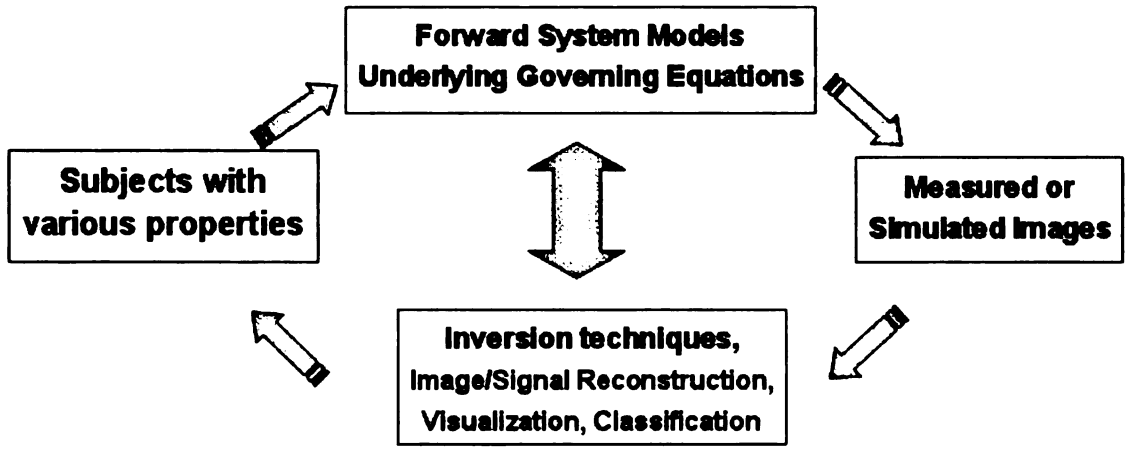


Figure 2.4 Relationship between the test object space and image space

### 2.4.1 Forward problems in imaging

As we discussed earlier, forward problems in imaging are the procedures that acquire images or signals from subjects in subject space, either by direct measurement or modeling. In this dissertation, we focus on the forward system models that can be represented as mathematical equations and explain the underlying physics. Simply speaking, the imaging process is modeled by the forward models.

### 2.4.2 Inverse problems in imaging

The inverse problems and the forward problems inverse of one another, which means the forward models input becomes the inverse output and vice versa. For historical reason, the forward problems, not only in imaging but also in mathematics, physics or mechanics, have been studied more extensively than the inverse problems. In this chapter, we will spend more time on discussing the general ideas, issues and techniques of inversion in imaging. More general introduction on inverse problems in imaging, the readers can refer to the book by M. Bertero [4]. The inverse problems in noninvasive imaging basically include reconstructing and/or interpreting an image of conditions inside the test objects from noninvasive or nondestructive evaluation.

### 2.4.3 Mathematical description of inverse problems

The system of interest can be simply specified by input variables X and output measurement Y. The measurement Y are functions of the input variables, which are also called the system state variables, and their relationship is shown as equation 2.1.

$$Y = A(X) \tag{2.1}$$

The map $A: X \to Y$ can be linear or nonlinear depending on the applications. In this chapter, we will mainly discuss the linear problems and the inversion of equation 3.1 becomes simply the inversion of $A$. By assuming we are working on a finite dimensional system and the map is linear and can be simplified into matrix form, we have the following equation:

$$Y = AX \tag{2.2}$$

By assuming $A$ is invertible, so the inverse problem is easily described as:

$$X = A^{-1}Y \tag{2.3}$$

Although equation 2.3 is straightforward mathematically, it is not always realistic due to the ill-posed problem in inversion.

# CHAPTER 3. ELECTROMAGNETIC IMAGING

## 3.1 Introduction

Detection and characterization of cracks under fastener holes (CUF) in aging aircraft is a significant challenge in nondestructive evaluation (NDE) applications. Figure 3.1 shows the geometry of the multi-layered structure in the CUF problem. Eddy current (EC) testing has been widely used for detecting such cracks for decades. However ECT has its own limitations: difficulty in detecting deeper defects due to skin depth, time consuming inspection process and cumbersome process of interpreting the complex impedance plane signal. Advanced electromagnetic imaging methods, such as eddy current Magneto Optic imaging and Giant Magneto Resistive imaging technique have recently found widespread use in inspection of airframe structures. Both these methods use eddy current excitation with the difference being in the sensors used to detect the magnetic field associated with the induced eddy currents.

Figure 3.1 Geometry of Crack under Fastener (CUF) problem

In this chapter, we start from the fundamental of electromagnetism, which helps us to understand the physics of Electromagnetic (EM) imaging. Principles of the two EM imaging, MO imaging and GMR imaging are then discussed. Challenges for these

two EM imaging are then brought up with the proposed solutions using the forward models and inversion techniques are presented in the following Chapters 4 and 5.

## 3.2 Fundamental of Electromagnetism

This section begins with a brief introduction of Electromagnetism, Electrical Field and Magnetic Field. Then the Maxwell's equations and related topics are discussed. For more detailed introduction for fundamental of Electromagnetism, readers may refer to [5] and [6].

The relationship between the magnetic field and electric field can be described by the Maxwell's equations, whose differential form are given by

$$\nabla \times \boldsymbol{E} = -\frac{\partial \boldsymbol{B}}{\partial t} \tag{3.1}$$

$$\nabla \times \boldsymbol{H} = \boldsymbol{J}_s + \boldsymbol{J} + \frac{\partial \boldsymbol{D}}{\partial t} \tag{3.2}$$

$$\nabla \cdot \boldsymbol{B} = 0 \tag{3.3}$$

$$\nabla \cdot \boldsymbol{D} = \rho \tag{3.4}$$

with the constitutive relations:

$$\boldsymbol{B} = \mu \boldsymbol{H} \tag{3.5}$$

$$\boldsymbol{D} = \varepsilon \boldsymbol{E} \tag{3.6}$$

$$\boldsymbol{J} = \sigma \boldsymbol{E} \tag{3.7}$$

In Equation (3.1) through (3. 7),

$\boldsymbol{E}$ = electric field intensity (volts/meter)

$\boldsymbol{D}$ = electric flux density (coulombs/square meter)

$\boldsymbol{H}$ = magnetic filed intensity (amperes/meter)

$\boldsymbol{B}$ = magnetic flux density (webers/square meter)

$\boldsymbol{J_S}$= source current density (amperes/square meter)

$\boldsymbol{J}$ = conduction current density (amperes/square meter)

$\rho$ = electric charge density (coulombs/cubic meter)

$\mu$ = permeability (henrys/peter)

$\varepsilon$ = permittivity (farads/meter)

$\sigma$ = conductivity (siemens/meter)

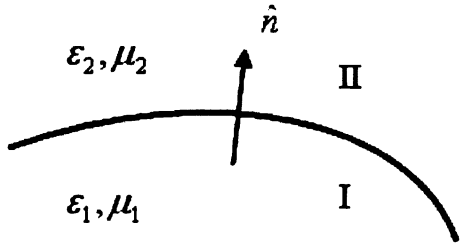


Figure 3.2 A boundary between two materials

Maxwell's equations should be satisfied everywhere in space, including the interface joining different materials. Applying equations (3.1) – (3.4) to the material interface shown in Fig 3.1 gives the boundary conditions: equations (3.8)-(3.11),

$$(E_{II} - E_I) \times \hat{n} = 0 \tag{3.8}$$

$$(H_{II} - H_I) \times \hat{n} = J_S \tag{3.9}$$

$$(B_{II} - B_I) \cdot \hat{n} = 0 \tag{3.10}$$

$$(D_{II} - D_I) \cdot \hat{n} = \rho_s \tag{3.11}$$

where $\hat{n}$ is defined as the unit vector normal to the interface pointing from medium I to medium II. This implies that only the tangential component of the electric field

intensity $E$ and the normal component of the magnetic flux density $B$ are always continuous on inter-material boundaries. The discontinuity of the tangential component of $H$ and the normal component of $D$ are characterized by the surface current $J_s$ and the surface charge $\rho_s$.

Time-harmonic analysis plays an important role in various engineering applications. A time-harmonic quantity refers to a variable which varies sinusoidally with time. A time-harmonic quantity can be expressed in exponential form

$$E(t) = E_p e^{j\omega t} \tag{3.12}$$

So, for time-harmonic fields, the Maxwell-Faraday's law (3.1) and Maxwell-Ampere's law (3.2) become

$$\nabla \times E = -j\omega B \tag{3.13}$$

$$\nabla \times H = J + j\omega D \tag{3.14}$$

In this way, a time domain problem can be considered in the frequency domain.

Both MO and GMR imaging applications are quasi-static problems. As can be seen from equations (3.2) or (3.14), there are two kinds of currents: conduction current and

displacement current. The conduction current is proportional to the electric field intensity, as stated by Ohm's law,

$$J = \sigma E \tag{3.15}$$

The displacement current is defined as the time varying rate of electric flux density.

$$J_d = \frac{\partial D}{\partial t} = j\omega\varepsilon E \tag{3.16}$$

In many circumstances, the time varying rate is low enough such that $\sigma >> \omega\varepsilon$. In such a case, the displacement current can be neglected and the quasi-static approximation is said to apply to the Maxwell-Ampere's law, i.e.

$$\nabla \times H = J \tag{3.17}$$

This equation implies that

$$\nabla \cdot J = 0 \tag{3.18}$$

Consequently, in steady state, electric current density is divergence free, since there is no accumulation of net charges. Two electromagnetic imaging applications: Magneto optical imaging and Giant magneto resistive imaging are discussed in the following sections.

## 3.3 Principle of Magneto optic imaging

Magneto optic (MO) imaging [27] [28] [29] is a relatively recent method used for inspecting aging metallic airframes for cracks and corrosion. MO imaging is a technology, based in part on the Faraday rotation effect, uses eddy current induction techniques along with a MO sensor, which generates real-time analog images of the magnetic fields associated with induced eddy currents. The MO imaging is used in aircraft inspection of rivet sites where data (images) from a large number of rivets need to be analyzed.

MO imaging technology uses an induction foil for inducing eddy currents in the conducting test sample and an MO sensor for detecting the magnetic flux density associated with the induced eddy currents. The MO sensor consists of a thin film of bismuth-doped iron garnet grown on a substrate of gadolinium gallium garnet with its easy axis perpendicular to the sensor surface.

The Faraday rotation effect observed by Faraday in 1845 states the plane of polarization of a linearly polarized light transmitted through a MO material (MO sensor) is rotated in the presence of a magnetic field as shown in Figure 3.3.

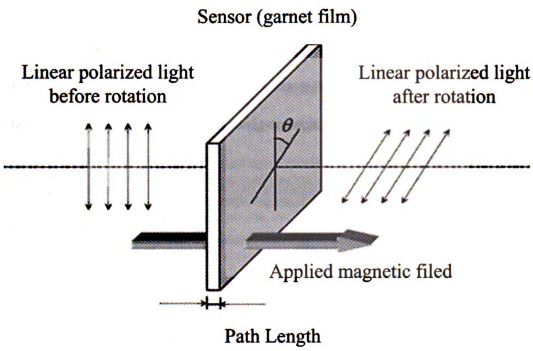


Figure 3.3 Faraday rotation effect in MO sensor

In a defect free specimen the induced current is uniform and the associated magnetic field is in the plane of the sensor. Anomalies in the specimen, such as fasteners and surface and subsurface cracks result in generating a normal magnetic flux density along the easy axis of the sensor. If linearly polarized light is incident on the sensor, the polarization plane of light is rotated by an angle θ that is proportional to the sensor thickness, given approximately by [28]:

$$\theta \approx \theta_f (\vec{k} \cdot \vec{M}) l / (|\vec{k}||\vec{M}|) \tag{3.19}$$

where $k$ is the wave vector of the incident light, $l$ is the sensor thickness, $M$ is the local state of magnetization of the sensor. Note that $M$ is always directed parallel to

the 'easy' axis of the magnetization of the sensor which is perpendicular to the sensor surface. When the reflected polarized light is viewed through the analyzer, the presence of normal magnetic field is seen as a 'dark' area in the MO image. A schematic of the MO imaging system using reflection mode geometry is illustrated in Figure 3.4.

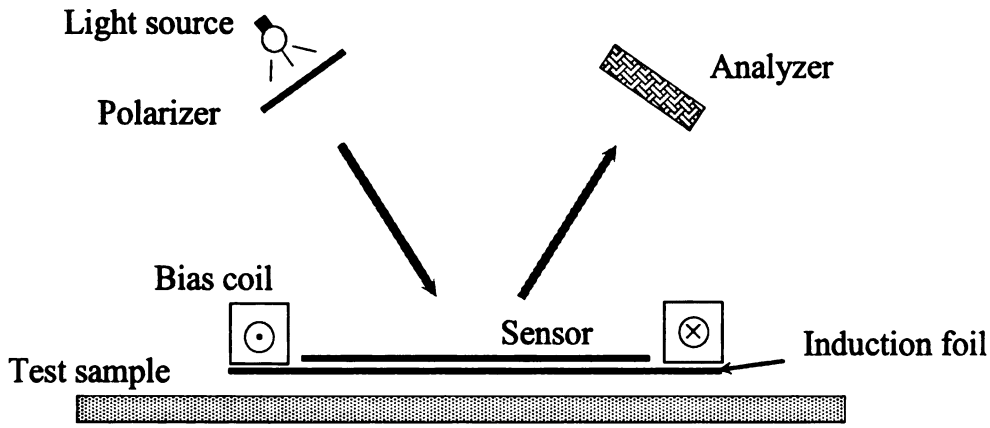


Figure 3.4 A schematic of MO imaging instrument

An intrinsic property of MO materials is the domain structure [30]. The MO images contain the images produced by these domain structures that must be accounted for in automated image processing schemes.

## 3.4 Principle of Giant Magneto Resistive (GMR) imaging

Among sensors that are capable of measuring the field due to induced currents directly, giant magneto-resistive (GMR) imaging sensors appear to be very promising because GMR imaging sensors offer exceptional levels of sensitivity, small size and

low cost. A simple GMR imaging sensor configuration, in which a linear excitation current sheet is applied, is shown in Figure 3.5, where the DC biased coil encircles the GMR sensor. The layout of the current sheet for inducing uniform current in the central region is shown in Figure 3.6. The GMR imaging sensor with biasing coil is located along the line of symmetry of current sheet, so that the output of GMR imaging sensor without sample discontinuity is always zero. The lift-off of the GMR sensor above the multi-layered structure with subsurface defects for the particular problem is 0.0095 inches in this dissertation.

Figure 3.5 A simple GMR imaging sensor configuration

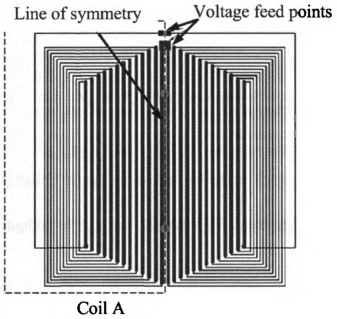


Figure 3.6 Layout of the excitation current sheet

The magnetic field generated by the excitation coil induces currents in the specimen. The induced currents are distorted if a crack is encountered. The GMR imaging sensor picks up perturbations in the fields associated with the induced eddy currents. Signal processing algorithms may be required to demodulate the signal detected by the GMR imaging sensor.

GMR sensor is unipolar in nature and is sensitive to the magnetic fields along the "easy" axis of the sensor. A typical response of GMR sensor to a field applied in the direction of "easy" axis is obtained experimentally by the GMR system [54] and shown in Figure 3.7. To quantitatively measure the magnetic flux density, the sensor needs to be biased using the dc biasing coil (shown in Figure 3.5) to work around the center of its linear range. The mathematical forms of the input and output signals of the GMR system are given as:

$$S_r = A_0 \sin(\omega t) \tag{3.20}$$

$$S_m = A_n \sin(\omega t + \varphi_n) \tag{3.21}$$

where $S_r$ is the excitation signal (also the reference signal) with the excitation frequency $\omega$ and amplitude $A_0$. For the sake of simplicity, the initial phase is assumed to be zero.

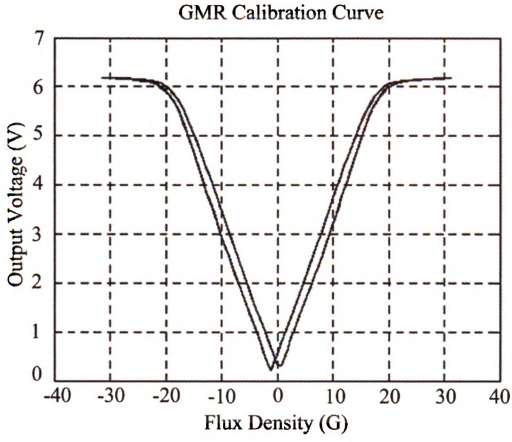


Figure 3.7 Response of GMR sensor to a field applied in the direction of "easy" axis that is obtained experimentally in GMR system

$S_m$ is the measurement GMR signal with the same frequency but different output amplitude $A_n$ and phase $\varphi_n$. The signal demodulation [59] first entails multiplying the two signals together and results in a high frequency AC term and a DC component, shown in Equation 3.22. Low pass filtering is applied to filter out the AC component by integrating over a couple of cycles. More generally, an arbitrary initial phase $\delta$ is introduced in this process as shown in Equation 3.23.

$$S_r(t) \cdot S_m(t) = A_0 A_n \sin(\omega t)\sin(\omega t + \varphi_n) = -\frac{A_0 A_n}{2}\cos(2\omega t + \varphi_n) + \frac{A_0 A_n}{2}\cos(\varphi_n) \tag{3.22}$$

$$\{S_r(t)\cdot S_m(t)\}_\delta = -\frac{A_0A_n}{2}\frac{\int_0^{n\pi/\omega} dt\cos(2\omega t+\varphi_n+\delta)}{\int_0^{n\pi/\omega} dt} + \frac{A_0A_n}{2}\cos(\varphi_n-\delta)\frac{\int_0^{n\pi/\omega} dt}{\int_0^{n\pi/\omega} dt}$$

$$= \frac{A_0A_n}{2}\cos(\varphi_n-\delta)$$

(3.23)

From Equation 3.23, the in-phase component $S_I$ and quadrature component $S_Q$ are easily obtained by setting the initial phase into $0°$ and $90°$.

$$S_I = \{S_r(t)\cdot S_m(t)\}_0 = A_oA_n\int_0^{nT} dt\sin(\omega t)\sin(\omega t+\varphi_n) = \frac{A_oA_n}{2}\cos(\varphi_n)$$

(3.24)

$$S_Q = \{S_r(t)\cdot S_m(t)\}_{90} = \frac{A_oA_n}{2}\sin(\varphi_n)$$

(3.25)

From the two components, both the amplitude $A_n$ and phase $\varphi_n$ could be extracted. The magnitude of the sensor signal can also be calculated as

$$S_M = \sqrt{{S_I}^2+{S_Q}^2}$$

(3.26)

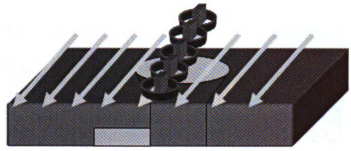

Figure 3.8 GMR sensor array with sheet current excitation foil

Figure 3.8 shows an alternative approach to using the GMR imaging sensor where the sinusoidal excitation current is applied to an induction foil. An array of GMR imaging sensors can be used to pick up the normal component of magnetic flux density generated by the induced currents. In the absence of any discontinuity, the magnetic flux is tangential to the specimen surface resulting in a null signal. Anomalies in the specimen result in a normal component of the magnetic flux density. The normal component of the magnetic field is sensed by the GMR imaging sensor. Alternately, a pulse excitation current can be applied to the induction foil and an array of GMR imaging sensors can be used to measure the transient magnetic field at different locations simultaneously. The output signals from the GMR sensor array contain time and space information. The information can be used to estimate the defect depth and location. Typical output magnitude images obtained using the GMR imaging sensor are shown in Figure 3.9(a), where the Box 1 shows the defect-free image and Box 2 shows the image of a fastener with a radial crack. The line plots across the center of the images in Figure 3.9(b) clearly show the difference between the defective fastener signal (solid line) and defect-free signal (dashed line) [54].

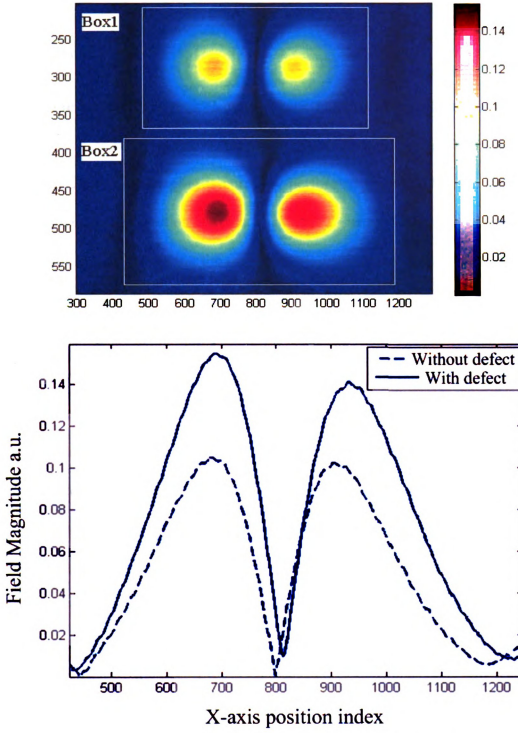


Figure 3.9 Typical GMR output images: defect-free (Box1) and defective (Box2) and central line plots: defect-free (dashed) and defective (solid)

## 3.5 Issues in Electromagnetic Imaging

### 3.5.1 MO Imaging

The proposed research objective is electromagnetic imaging of this dissertation is the development of a reliable, efficient, fully automated system for the inspection of aging airplane skins. MO imaging is currently performed manually by scanning the MO imager over the inspection surface. "Detection" using MOI depends on the judgment of the inspector viewing the displayed MOI image. Even with training, this is a subjective decision; therefore, this can produce varying results from inspector to inspector depending on their ability to discern a defect. Another problem is the inspector's inevitable ennui as only a very small percentage of the images show any anomalies. The MO images are 2D analog images of the 3D magnetic field distribution. The image processing in MO imaging requires one to quantify the asymmetry in the 2D images to determine the defect size and shape.

These problems can be mitigated with the application of modern image processing and pattern recognition technologies to provide automated defect detection. An automated real-time method for evaluating the MO images for structural defects can reduce human error and increase accuracy and speed of the inspection. Such a method will require the elimination of the background (image) noise due to magnetic domain walls in the MO sensor and enhancing the image for subsequent interpretation.

### 3.5.2 GMR Imaging

GMR imaging technique offers much higher sensitivity enabling detection of defects located deep in the test object. The interpretation and analysis of GMR data is crucial to eliminate the operator variability and subjectivity and maximize the probability of detection (POD). The GMR images are complex requiring higher computational power for analyzing the images. This dissertation presents development of new mathematical forward models, efficient image processing and crack detection algorithms for GMR data. Through the forward and inverse techniques development, the GMR imaging sensor can also be optimized to increase the GMR imaging system detectability.

# CHAPTER 4. FORWARD MODELS FOR ELECTROMAGNETIC IMAGING

## 4.1 Introduction

Forward models using computational methods play an important role in nondestructive evaluation (NDE). Numerical models serve many purposes such as understanding the underlying physics, visualizing the fields, conducting a parametric study and serving as a test bed to generate signals due to complex defect shapes.

Computational methods for modeling electromagnetic imaging problems fall into two major classes, namely, analytical and numerical approaches. Analytical models are capable of providing ideal, closed form solutions to problems. However, such analytical models are, in general, limited in their application to simple specimen and defect geometries, such as infinite half plane samples and regular, rectangular or hemispherical crack geometry. Numerical models have gained popularity in recent years due to their ability to simulate arbitrary shaped defects in complex sample geometries. Numerical models can simulate problems with high dimensionality as well as nonlinearity, anisotropy and inhomogeneous material properties.

With the development of faster and more powerful computers, the development and implementation of the numerical models have become a major research focus in nondestructive evaluation (NDE) [37] [38]. Several numerical modeling methods

have been developed for solving the governing equations describing various NDE phenomena, such as finite difference method (FDM), finite element method (FEM), boundary element methods (BEM), boundary integral methods (BIM) and volume integral methods (VIM). Each method has its own advantages and limitations and is appropriate for different kinds of numerical problems [39] [40] [41].

The finite difference method is a simple and intuitive numerical modeling method for solving partial differential equations (PDE). The major advantage is its relative ease for approximating partial derivatives by corresponding finite difference formulation. It is widely applied for direct current, quasi-static, transient fields, and linear problems. A limitation of the finite difference technique is its poor convergence property, particularly in the case of irregular geometries. Also, finite difference formulations do not lend themselves easily for modeling distributed parameters such as the current densities, conductivities and permeability [42].

FEM evolved in the late 1950s as a numerical technique in structural analysis and was quickly adapted as a major numerical modeling method in various engineering fields to solve PDE. The finite element domain discretization scheme allows modeling of complex shapes, making it efficient and relatively more accurate. Compared with FDM, FEM has many advantages including its ease of imposing essential boundary conditions and modeling complex geometries. FEM formulations can be easily extended to handle higher order approximation and thereby lead to faster convergence and better accuracy. The resulting matrix equations are in general sparse, banded and diagonally dominant making the solutions process very stable [45]. FE models have

been developed and used for a variety of two and three-dimensional eddy current NDE problems [43][46].

The drawbacks of FEM include large computer resources especially for nonlinear and time-dependent problem. Also, the finite element method is not well suited for open region problems [45] encountered in wave regimes. In the area of antenna and electromagnetic wave propagation, integral equation based approaches are more commonly used. BEM and VIM methods based on the integral equations [45] along with absorbing boundary conditions are typically used in wave propagation problems where the Green's function is readily available.

Boundary integral methods solve Maxwell's equations by integrating the appropriate Green's function over the boundary using the given boundary conditions. Hence there is a need to discretize only the boundary surface in the integral equations, rather than the entire solution domain. In the post-processing phase, the integral equation is used again to calculate the required physical quantity at any point in the solution domain.

In the case of inhomogeneous problems, VIM is commonly applied to discretize the volumetric source for solution. In VIM, the field is determined at a point by summing the effects of the sources at all points. The volume integral computes a convolution of the source points with the appropriate Green's function. The advantage is it is only necessary to construct a mesh over the test sample and solve for the currents in the test sample. But this method also requires computation of the Green's function which in itself may not be trivial.

Integral equation based formulation is in general more efficient than differential equation model with regard to computer resources but the resulting global stiffness matrix equation is generally fully populated and ill conditioned leading to instabilities [45]. More importantly VIM and BEM are inherently linear and can be used to solve linear homogeneous problems. Lastly these methods are useful only when the Green's function for the problem is easily available.

In this dissertation, we use the finite element method for modeling the multi-layered geometry largely due to the ease of modeling ferrite and non-ferrite fasteners and complex defect shapes, as well as the inherent stability and accuracy of the solution.

## 4.2 Finite element methods

The finite element method (FEM) is one of the most widely used tools for solving field problems. The method finds applications in diverse areas of engineering and science largely due to its ability to model intricate geometries efficiently and accurately. In the last few decades, FEM has been applied with great success in such areas as the study of DC and low frequency electromagnetic fields in electrical machines, design of structures, modeling thermal fields and nondestructive evaluation.

A formulation of the problem from first principles derived from Maxwell's equations governing the differential equations to be solved in the model is provided by Jin [45]. Two- and three-dimensional electromagnetic finite element models for

electromagnetic imaging applications have been developed [43][46][47][48][49]. More details of the MO imaging and GMR imaging modeling efforts can be found in [55][62]. The major steps in finite element modeling are described briefly below. Maxwell's equations in differential form are given in Chapter 3, Equations 3.1 to 3.7.

The Vector potential formulation, A-V Formulation is used in this dissertation. From Equation 3.3, the magnetic flux density is divergence free and can be expressed in Equation 4.1 as the curl of a vector

$$\boldsymbol{B} = \nabla \times \boldsymbol{A} \tag{4.1}$$

where A is the magnetic vector potential. The magnetic field intensity can also be expressed in terms of A, as

$$\boldsymbol{H} = \frac{1}{\mu} \nabla \times \boldsymbol{A} \tag{4.2}$$

Substituting (4.1) into the Faraday's Law (3.1), we get

$$\nabla \times \boldsymbol{E} = -\nabla \times \frac{\partial \boldsymbol{A}}{\partial t} \tag{4.3}$$

$$\nabla \times \left( \boldsymbol{E} + \frac{\partial \boldsymbol{A}}{\partial t} \right) = 0 \tag{4.4}$$

The electric field intensity can be express as

$$\boldsymbol{E} = -j\omega\boldsymbol{A} - \nabla V \tag{4.5}$$

The $j\omega$ term is introduced since we are dealing with the time-harmonic problems. Equation 4.5 tells us that the electric field intensity $\boldsymbol{E}$ can be expressed in terms of the magnetic vector potential $\boldsymbol{A}$ and the scalar function $V$.

### 4.2.1 Sample Geometry and Mesh Generation

The detailed test geometry simulated in EM imaging is described in Section 3.3, which has a multilayer geometry and consists of two layers of aluminum shown in Figure 4.1. Only the general geometry is shown in this dissertation, without detailed information

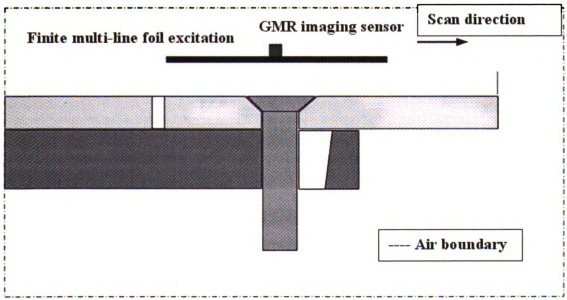


Figure 4.1 Modeling geometry for test sample in EM imaging

The sample contains a top layer and second layer edges close to the fastener. Notches are introduced at the fastener holes as shown in Figure 4.1. The three dimensional domain is discretized using brick or hexahedral elements interconnected at 8 nodes. The mesh size and complexity increases particularly when a small air gap of 0.005 inch is introduced between the layers and also between the fastener and plate. The density of mesh elements were optimized and validated by comparing the model prediction with experimental measurements.

### 4.2.2 Interpolation/Shape functions and Global Matrix Assembly

The magnetic vector $A$ and electric scalar potential $V$ in an element e is expressed in terms of selected linear or quadratic interpolation functions as follows

$$A^e = \sum_{j=1}^{8} N_j^e A_{xj}^e \hat{x} + N_j^e A_{yj}^e \hat{y} + N_j^e A_{zj}^e \hat{z} = \sum_{k=1}^{24} N_k^e A_k^e \tag{4.6}$$

$$V^e = \sum_{j=1}^{8} N_j^e V_j^e \tag{4.7}$$

where

$$\boldsymbol{N}_k^e = \begin{cases} N_j^e \hat{x} & k = 3j-2 \\ N_j^e \hat{y} & k = 3j-1 \\ N_j^e \hat{z} & k = 3j \end{cases}$$

(4.8)

and

$$A_k^e = \begin{cases} A_{xj}^e & k = 3j-2 \\ A_{yj}^e & k = 3j-1 \\ A_{zj}^e & k = 3j \end{cases}$$

(4.9)

where $A_{xj}, A_{yj}, A_{zj}$ and $V_j$ are the three Cartesian components of the vector potential and the scalar potential at node j; and $N_j$ is the shape function associated with node j that assumes the value of one at this node and the value of zero at any other node. The vectors $\hat{x}, \hat{y}, \hat{z}$ are the Cartesian unit vectors.

Using the Galerkin formulation [45], and imposing the Coulomb gauge on Equation 4.1 and 4.6, we obtain

$$\sum_{j=1}^{24} \{ \int_{\Omega_e} (\frac{1}{\mu} \nabla \times \boldsymbol{N}_i^e) \cdot (\nabla \times \boldsymbol{N}_j^e) + (\frac{1}{\mu} \nabla \cdot \boldsymbol{N}_i^e)(\nabla \cdot \boldsymbol{N}_j^e) dV \} A_j^e +$$

$$\sum_{j=1}^{24}\{\int_{\Omega_e} j\omega\sigma \boldsymbol{N}_i^e \cdot \boldsymbol{N}_j^e dV\}A_j^e + \sum_{j=1}^{8}\{\int_{\Omega_e} \sigma \boldsymbol{N}_i^e \cdot \nabla \boldsymbol{N}_j^e dV\}V_j^e -$$

$$\int_{\partial\Omega_e} \boldsymbol{N}_i^e \cdot (\frac{1}{\mu}\nabla \times \boldsymbol{A}^e \times \hat{n})dS - \int_{\partial\Omega_e} \boldsymbol{N}_i^e \cdot (\hat{n}\frac{1}{\mu}\nabla \cdot \boldsymbol{A}^e)dS = \int_{\Omega_e} \boldsymbol{N}_i^e \cdot \boldsymbol{J}_s^e dV \tag{4.10}$$

, for $i = 1,2,\cdots,24$.

$$\sum_{j=1}^{24}\{\int_{\Omega_e} j\omega\sigma \nabla N_k^e \cdot \boldsymbol{N}_j^e dV\}A_j^e + \sum_{j=1}^{8}\{\int_{\Omega_e} \sigma \nabla N_k^e \cdot \nabla N_j^e dV\}V_j^e +$$

$$\int_{\partial\Omega_e} \sigma N_k^e(-j\omega \boldsymbol{A} - \nabla V)\cdot \hat{n} dS = 0 \tag{4.11}$$

for $k = 1,2,...,8$ where $\hat{n}$ is the outward unit vector and $\partial\Omega_e$ is the boundary of the sub-domain $\Omega_e$. Combining these equations together, we obtain a $32 \times 32$ matrix equation,

$$[G]^e\,[U]^e = [Q]^e \tag{4.12}$$

The global stiffness matrix is obtained by assembling each element matrix $[G]^e$ together. The value at each entry is the sum of values contributed by all the connected elements.

$$GU = Q \tag{4.13}$$

where $G$ is a complex, symmetric sparse matrix, $U$ is the vector of unknowns consisting of the electric scalar potential and the three components of the magnetic vector potential at each node and $Q$ is the load vector incorporating the current source.

### 4.2.3 Boundary and Interface Conditions

In order to obtain a unique solution, appropriate boundary conditions need to be imposed before solving the system of equations. Either Dirichlet boundary conditions (values of $A$ or $V$ on the boundary) or Neumann boundary conditions (values of the magnetic flux density $B$ or the magnetic field intensity $H$ on the boundary) need to be specified. Since Neumann boundary conditions are usually included implicitly in the finite element formulation, we only need to impose Dirichlet boundary conditions. Current continuity conditions will be explicitly imposed at the interface boundaries to avoid spurious solutions.

### 4.2.4 Matrix Solution

The finite element procedure results in a linear algebraic system of equations that must be solved to determine the unknown coefficients of the shape functions. The equations can be solved using either direct or iterative methods. The Gaussian elimination method is a direct approach that can be used to solve either full or sparse

matrix equations. In the finite element method, the stiffness matrix is usually sparse and banded. In such cases, it is more advantageous to employ iterative methods since they are more efficient with respect to computational cost and data storage. A number of iterative methods have been proposed over the years. However, only a small number of them can be used for solving the complex-valued matrix equations arising in quasi-static electromagnetic problems.

An important issue in iterative methods is its convergence properties. The convergence of iterative process depends on the properties of the matrix, such as its eigen values, the singular value or condition number. Usually a large condition number will result in a large solution error or sometimes even failure to converge. Thus the process of "preconditioning" is essential for the success of iterative methods. The overall solution procedure requires $O(N)$ multiplications and additions [50].

### 4.2.5 Post-Processing

After we solve for the potentials, physical and measurable quantities of interest, such as the magnetic flux density $B$, coil impedance and induced current density $J$, can be calculated using:

$$\boldsymbol{B} = \nabla \times \boldsymbol{A} \tag{4.14}$$

$$\boldsymbol{E} = -j\omega \boldsymbol{A} - \nabla V \tag{4.15}$$

$$\boldsymbol{J} = \sigma \boldsymbol{E}$$

(4.16)

Where Equations 4.14 through 4.16 are the same as Equations 4.1, 4.5 and 3.7 and presented here again for the reader's convenience. GMR imaging sensors measure the normal component of the magnetic flux density $B$. The different components of the magnetic flux density can be obtained from the nodal values of magnetic vector potential as:

$$B_x = \frac{\partial A_z}{\partial y} - \frac{\partial A_y}{\partial z}$$

(4.17)

$$B_y = \frac{\partial A_x}{\partial z} - \frac{\partial A_x}{\partial x}$$

(4.18)

$$B_z = \frac{\partial A_y}{\partial x} - \frac{\partial A_x}{\partial y}$$

(4.19)

The current density $J$ inside element e is determined at the element center from the relation in Equation 4.20 and the components $J_y^e, J_z^e$ can be calculated similarly.

$$J_x^e = -j\omega\sigma A_x^e - \sigma\frac{\partial V^e}{\partial x} = -j\omega\sigma\sum_{i=1}^{8} N_i^e A_{xi}^e - \sigma\sum_{i=1}^{8}\frac{\partial N_i^e}{\partial x}V_i^e$$

(4.20)

### 4.2.6 Modeling MO and GMR sensors with Induction Foil Excitation

The excitation source in this project is applied to an infinite planar induction foil located parallel to the surface of the specimen. For a linear sinusoidal current excitation with angular frequency of $\omega$, the source current is

$$j_{lin} = \mathrm{Re}[J_0 e^{j\omega t}] = J_0 \cos\omega t$$

(4.21)

where $J_0$ is the magnitude of the current. However a probe with a linear excitation current flow pattern is sensitive only to cracks that are perpendicular to the current direction. In this project, to best detect a crack oriented in the x direction the current flow is assumed to be along the y direction, i.e., $J_{in} = \hat{y}J_0$ where $\hat{y}$ is the unit vector along the y-axis. The normal component of magnetic flux density $B_Z$ is measured by the GMR imaging sensor array.

## 4.3 Forward model results

Although difference imaging sensors are used in the MO and GMR imaging, the EM fields generated by the excitation current are the same. Hence the same forward model results can be used for simulating both MO and GMR signals. We start from a two dimensional validation using a simple geometry and finally analysis the EM field of the real testing sample.

### 4.3.1 Validation Results

The finite element model developed for electromagnetic imaging inspection of multilayer test samples was first validated using experimental GMR measurements from the calibration notch sample.

The validation sample is made of standard aluminum, which is a plate of dimensions 16 inches times 10 inches and of thickness 0.625 inch. A notch of dimensions 0.05 inch width and 0.25 inch depth is machined at the center of the sample. A photograph of the sample is shown in Figure 4.2.

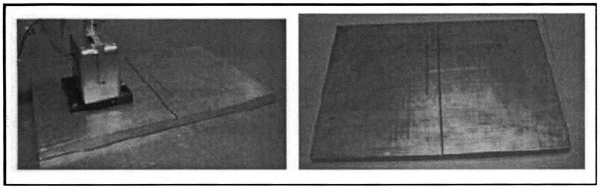

(a) (b)

Figure 4. 2 Photographs of (a) the sensor head at the zero-balancing calibration position and (b) an overhead view of the calibration sample with slot down the middle. The imaging sensors and excitation current are aligned parallel to the slot

The three dimensional domain of the finite element model and the corresponding mesh are shown in Figures 4.3 and 4.4 respectively.

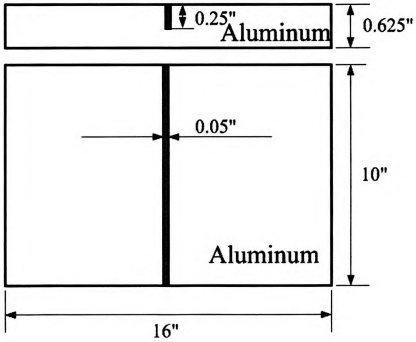


Figure 4.3 Sample Geometry used in the model

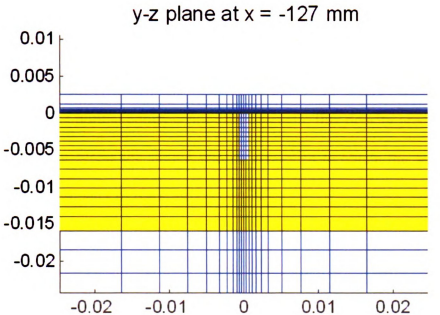


(a)

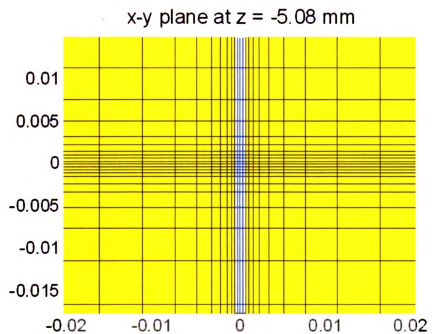


(b)

Figure 4.4 (a) Side view and (b) top view of the finite element mesh

The FEM model solutions produce the electric scalar potential $V$ and magnetic vector potential $A$ at each node in the solution region. The magnetic flux density $B = \nabla \times A$ is computed and its normal component is compared with the measured GMR signal. Figure 4.5 shows the normal component of the magnetic flux density predicted by the model. The 2D scan across the slotted sample is applied to obtain the sensor signal. Figure 4.6 shows geometry of the scan.

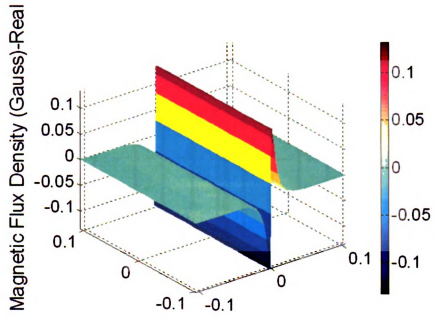


(a)

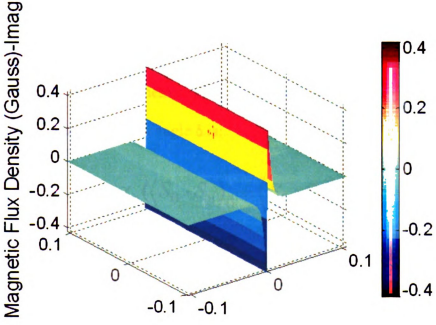


(b)

Figure 4.5 Modeling results of the normal component of the magnetic flux density (a) real part (b) imaginary part

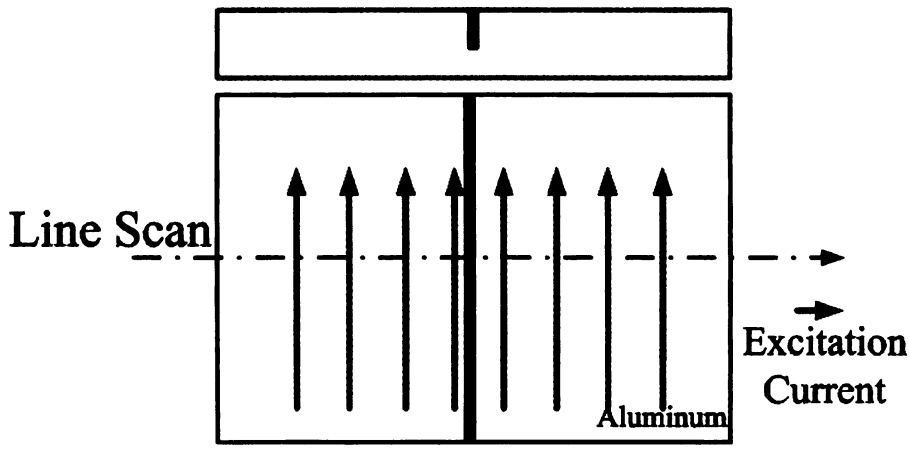


Figure 4.6 Geometry of scan plan with excitation current parallel to the slot

Experimental signals for the sample were available for various demodulation angles as described in Section 3.4, principle of GMR imaging. The in-phase and quadrature components were demodulated to generate a mixed signal using varying demodulation angle δ. The mathematical form for the calibrated demodulated signal for sensor n at arbitrary detection angle δ is:

$$\langle S_0 \cdot S_n \rangle_\delta = \alpha_n (\langle S_0 \cdot S_n \rangle_0 - \langle S_0 \cdot S_n{}^0 \rangle_0) \cos(\delta)$$
$$+ \alpha_n (\langle S_0 \cdot S_n \rangle_{\pi/2} - \langle S_0 \cdot S_n{}^0 \rangle_{\pi/2}) \sin(\delta) \qquad (4.22)$$

where $\langle S_0 \cdot S_n \rangle_\delta = \frac{A_0 A_n}{2} \cos(\phi_n - \delta)$

In finite element modeling, the zero balancing term $\left\langle S_0 \cdot S_n^{\,0} \right\rangle_{\delta}$ and the scaling factor $\alpha_n$ are 0 and 1 respectively since these two terms are only useful in experimental data analysis. From the validation results show in Figure 4.7, we can conclude that the model result accurately predicts the experimental measurements.

Figure 4.7 Comparison of demodulated and calibrated signal across the calibration slot

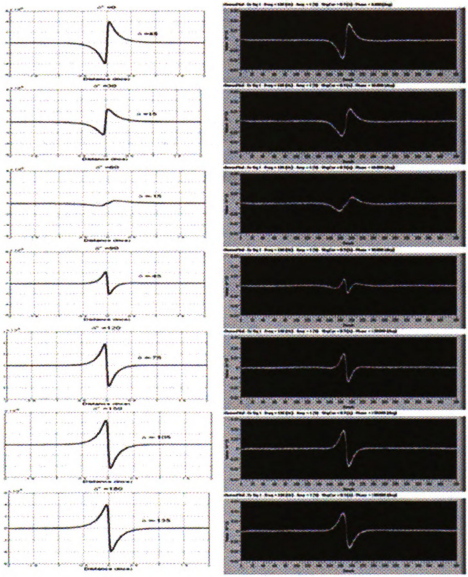

(a)

Figure 4.7 continued

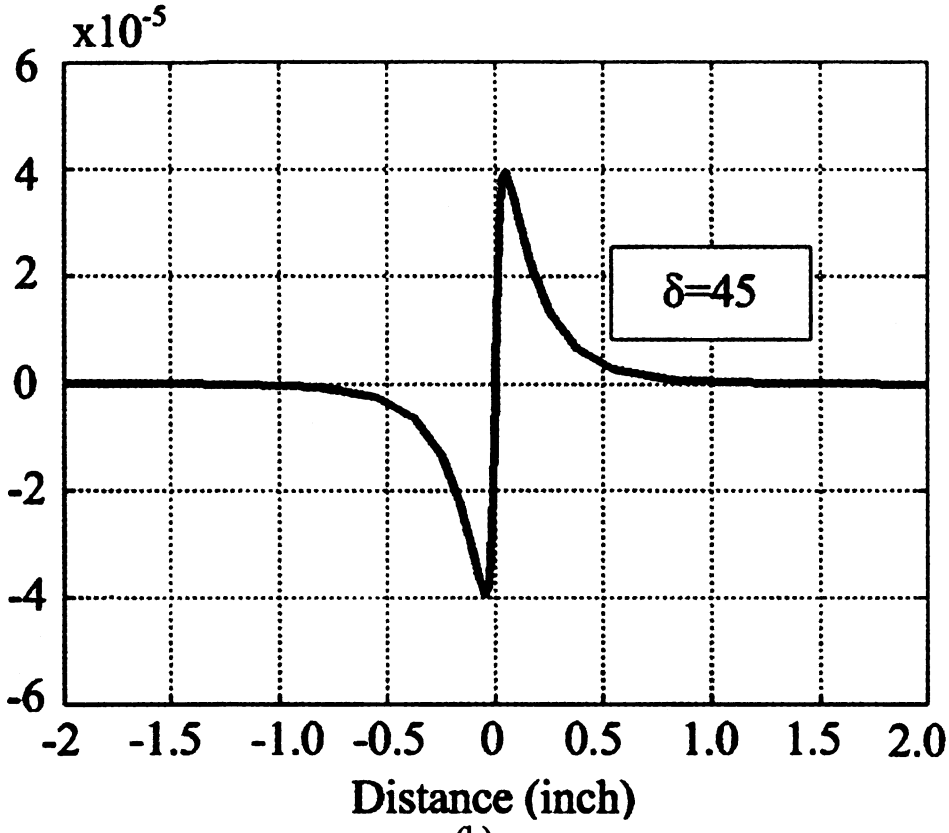


(b)

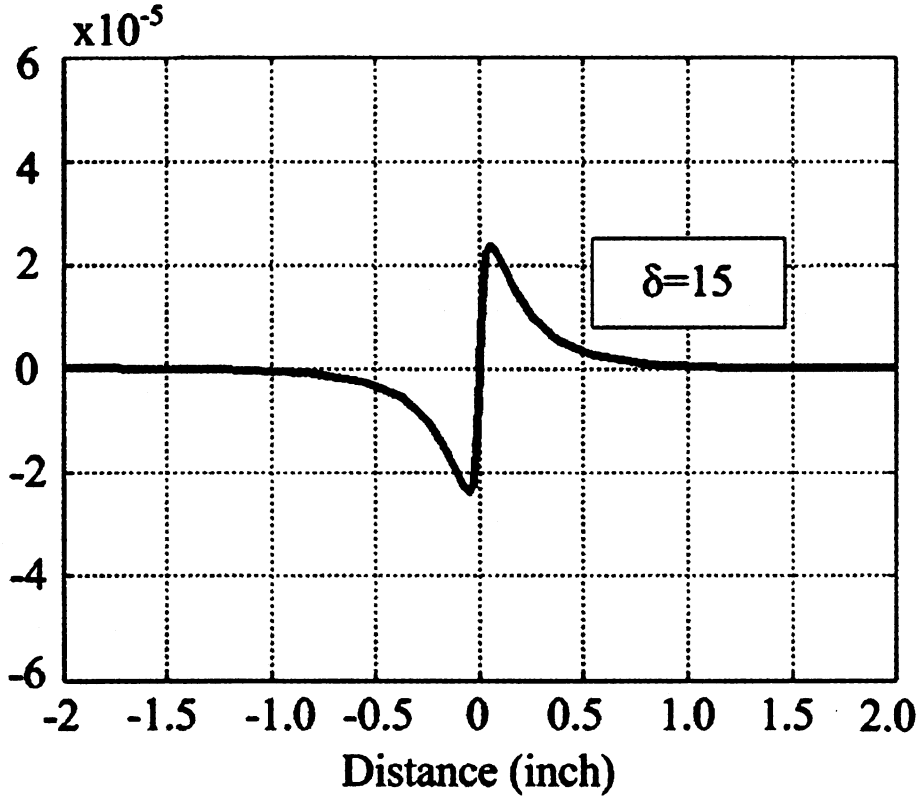


(c)

Figure 4.7 continued

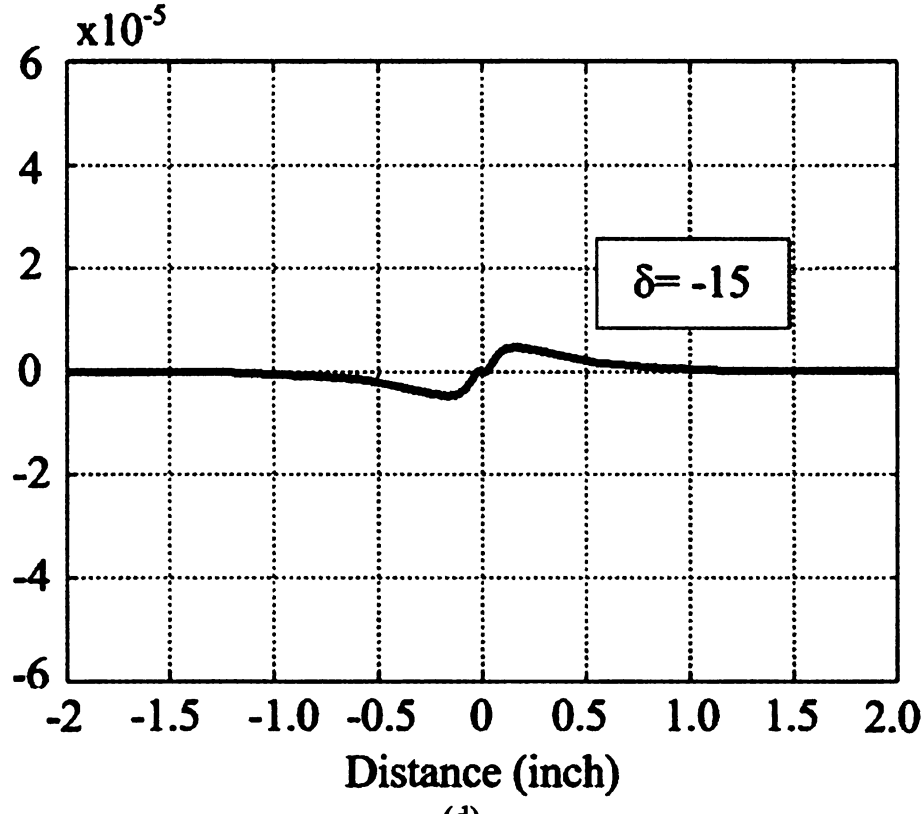


(d)

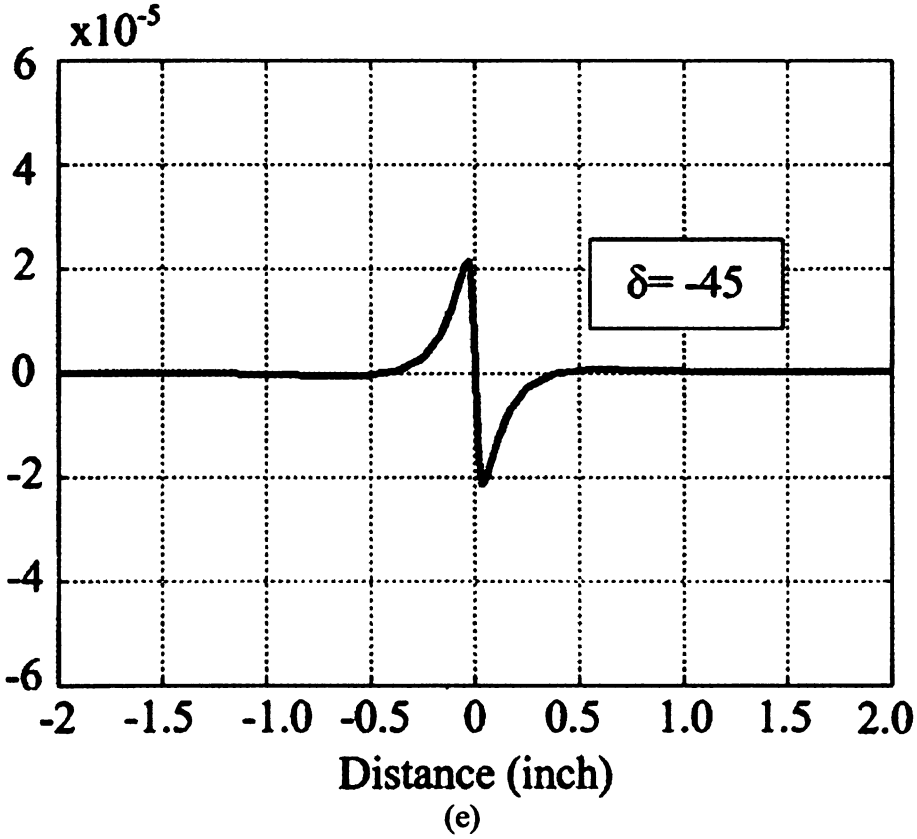


(e)

Figure 4.7 continued

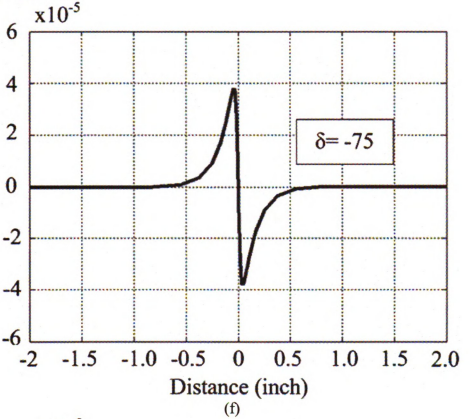


(f)

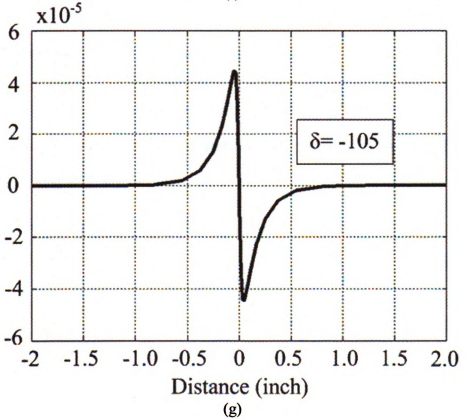


(g)

Figure 4.7 continued

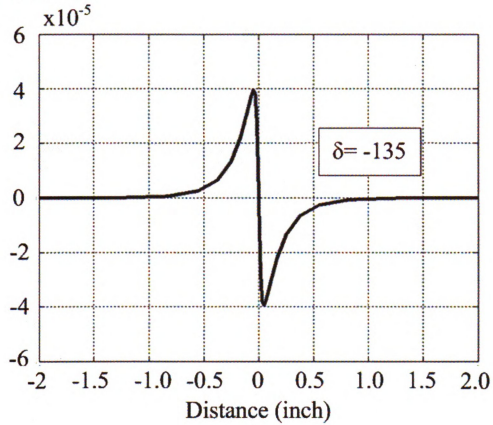


(h)

### 4.3.2 3D Results

A schematic of the three dimensional (3D) geometry of the sample with subsurface crack, imaging sensor configuration and scan direction are shown in Figure 4.8, which is the same as Figure 4.1.

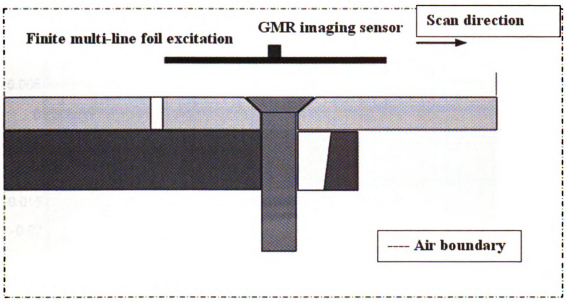


Figure 4.8 Geometry of the test sample

The fastener material in this sample is Titanium. The side view shows top layer truncated in accordance with the sample geometry. The model also simulates the gap between the two top skins of the test sample. The current is parallel to the notch length and the scan direction is perpendicular to it. The optimized 3D finite element mesh for this sample with edge is shown in Figure 4.9.

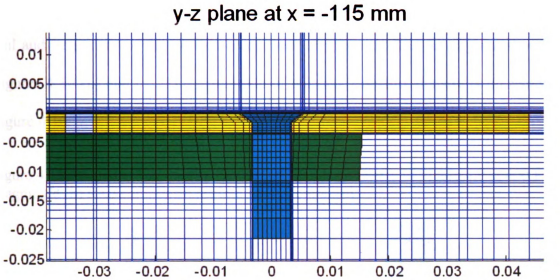


(a)

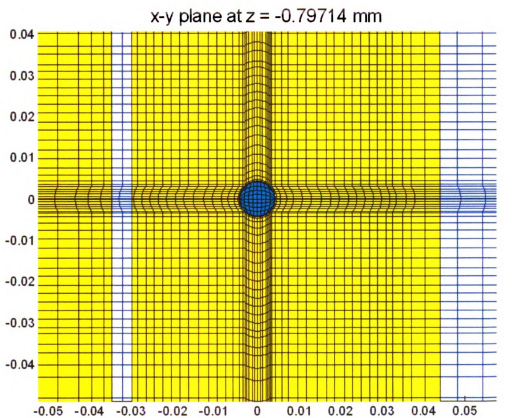


(b)

Figure 4.9 FE mesh for the test sample: (a) side view (b) top view

The modeling results at 400Hz excitation frequency are shown in Figure 4.10. The real and imaginary of the normal component of magnetic flux density are shown in Figures 4.10 (b) and (c). The magnitude of the magnetic flux density is presented in Figure 4.10

Figure 4.10 Magnetic flux density for the test sample geometry in Figure 4.9 at 400 Hz (a) Magnitude (b) Real component (c) Imaginary component

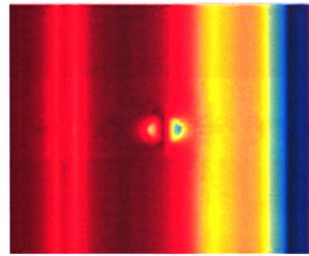

(a)

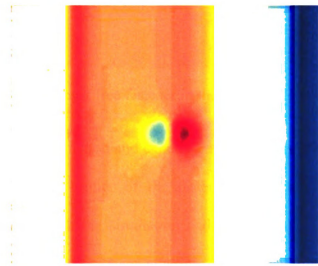

(b)

Figure 4.10 continued

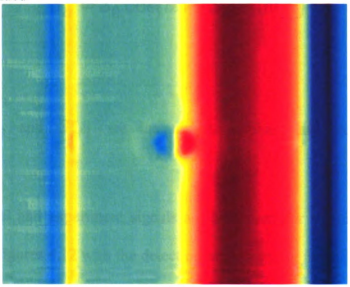

(c)

The corresponding experimental data from the rivet is shown in Figure 4.11.

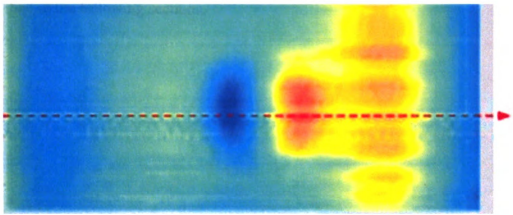

Figure 4.11 GMR data for crack free fastener in the test sample at 400 Hz (The line scan is marked by the red dashed line)

A comparison between simulation and experimental results is presented. Line scans in the x-direction across the center of the fastener is extracted from the real and imaginary image data (both the simulation and experiment) which are then mixed using different demodulation or detection angles. The detection angle $\alpha$ and the mixed GMR sensors signal is given by

$$S_\alpha = S_0 \cos(\alpha) + S_{\pi/2} \sin(\alpha)$$

(4.23)

where $S_\alpha$, $S_0$ and $S_{\pi/2}$ are the mixed, in-phase and quadrature signals respectively.

The mixed model and experiment signals are compared for a number of detection angle values in Figures 4.12 with the detection angle varying from 80 to 190 degrees. Both the magnitude and shape of the signals are remarkably similar. The results in Figure 4.12 indicate the use of the model in conducting a parametric study as described in the following sections.

Figure 4.12 Comparison between experimental and modeling signal with varying detection angles

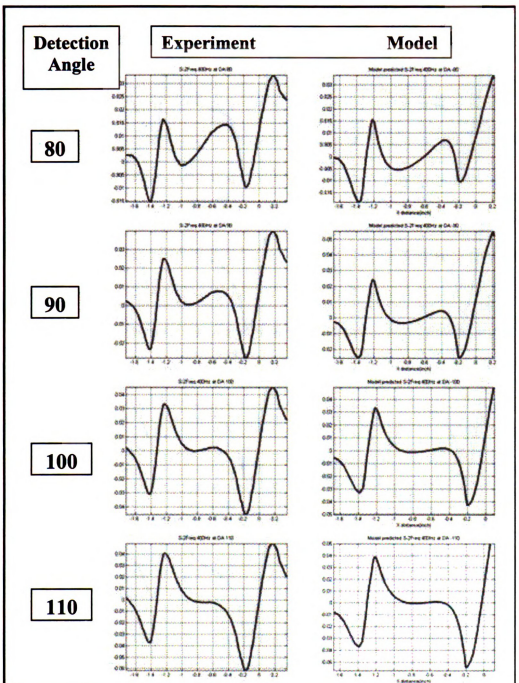


(a)

Figure 4.12 continued

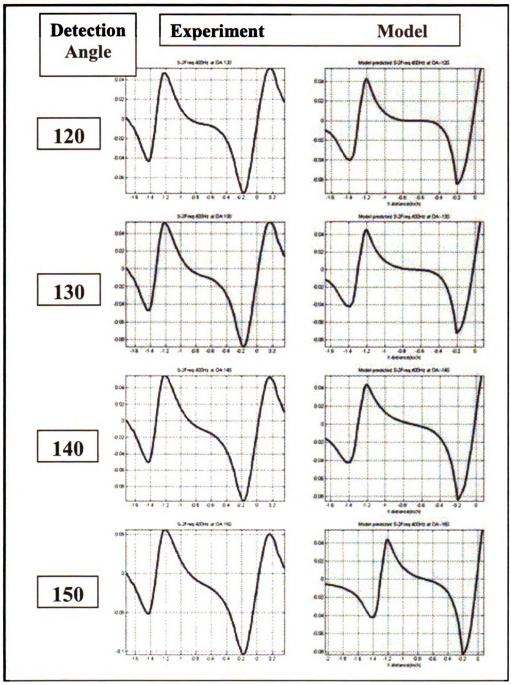


(b)

Figure 4.12 continued

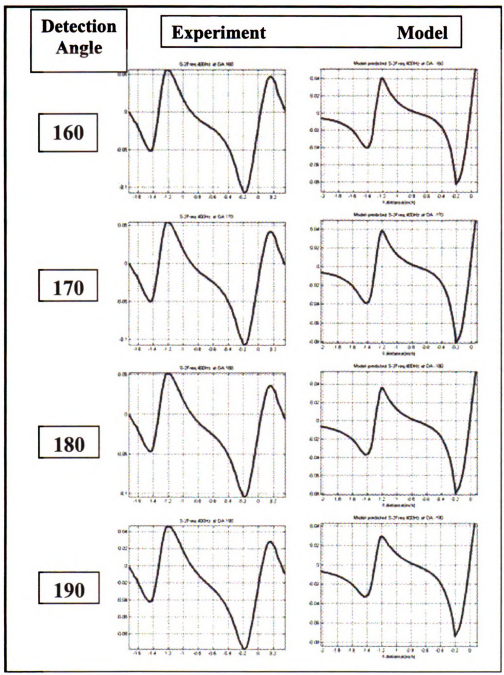


(c)

## 4.4 Electromagnetic Imaging Parameters

The validated FEM model was used to study the effect of various experimental parameters on the GMR signal. Table 4.1 lists parameters along with the rage of values.

Table 4.1 Electromagnetic GMR imaging sensor parameters

| PARAMETER | RANGE OF VALUES |
|---|---|
| Frequency (kHz) | 0.1, 0.2, 0.4, 0.5, 0.7, 1.0, 2.0, 3.0, 5.0, 7.0 |
| Sensor liftoff (inch) | 0.0050, 0.0095, 0.015, 0.1, 0.15, 0.2 |
| Conductivity of top layer (%IACS) | Between 28 and 33 |
| Conductivity of bottom layer (%IACS) | Between 30 and 36 |
| Conductivity of fastener (%IACS) | Titanium (6Al, 4V): 1.0, 2.2, 3.1 |
| Fastener to edge distance (inch0 | 0.40, 0.50, 0.60, 0.70, 0.80 |
| Crack dimensions (inch) | 0.20, 0.22, 0.25, 0.30 |

### 4.4.1 Frequency

Since most aircraft geometry contains multiple layers with cracks in second and third layer the operating frequencies is largely at the low end. The range of frequencies considered in this study is: 0.1, 0.2, 0.4, 0.5, 0.7, 1.0, 2.0, 3.0, 5.0 and 7.0 kHz. The geometry of the test sample and sensor configuration and finite element mesh are shown in Figures 4.8 and 4.9. A 0.3 inch second layer defect is introduced under the

fastener through the second layer on the side of the stringer edge. The normal component of magnetic flux density $B_z$ is calculated for each frequency, for both, the crack free case and 0.3 inch crack case.

Figure 4.13 shows the simulation results at a frequency of 0.1 kHz. The images in Figure 4.13(a), 4.13 (c) and 4.13 (e) are the magnitude, real and imaginary parts of the normal component of flux density for crack free case at a lift-off of 0.0095 inch. Images in Figure 4.13 (b), 4.13 (d) and 4.13 (f) are the corresponding magnitude, real and imaginary parts of the normal component of flux density for 0.3 inch crack geometry. Figures 4.14 to 4.18 present similar model predicted results for frequencies of 400, 500, 700, 2000 and 7000 Hz. The real, imaginary and absolute magnitude of the normal component magnetic flux density for both defect free and 0.3 inch crack are presented.

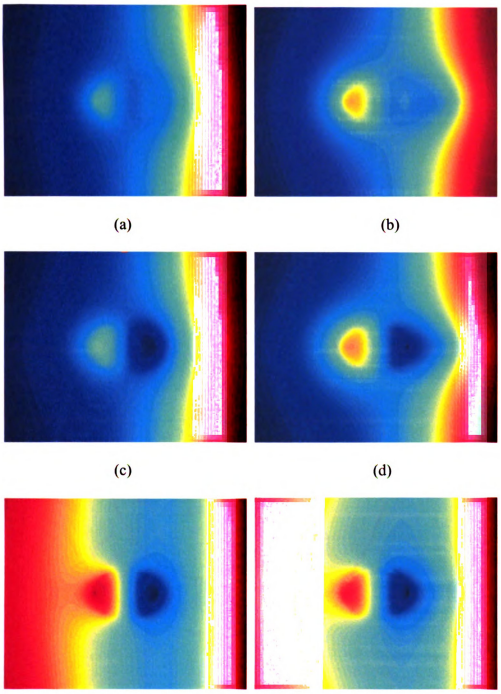


Figure 4.13 Frequency Parameter: simulation results at 100 Hz

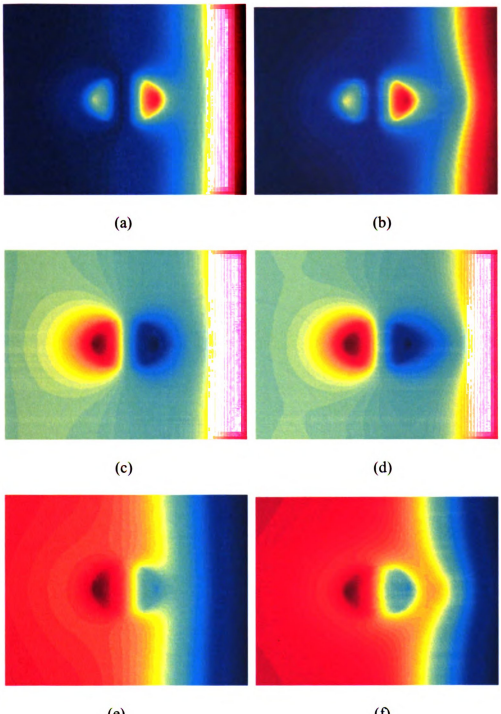


Figure 4.14 Frequency Parameter: simulation results at 400 Hz

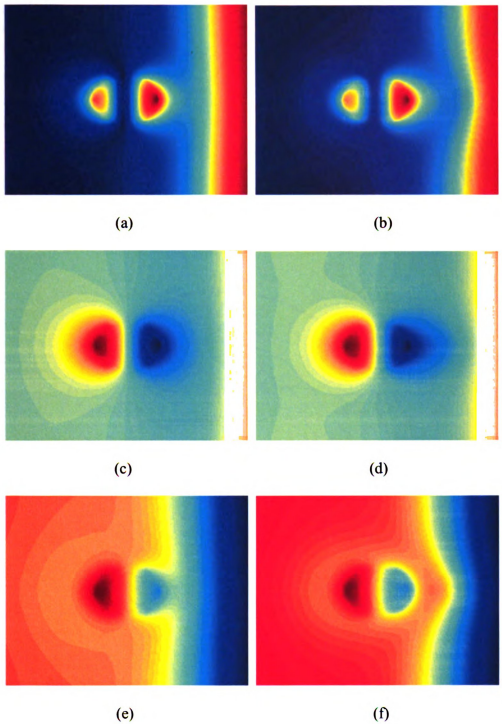


Figure 4.15 Frequency Parameter: simulation results at 500 Hz

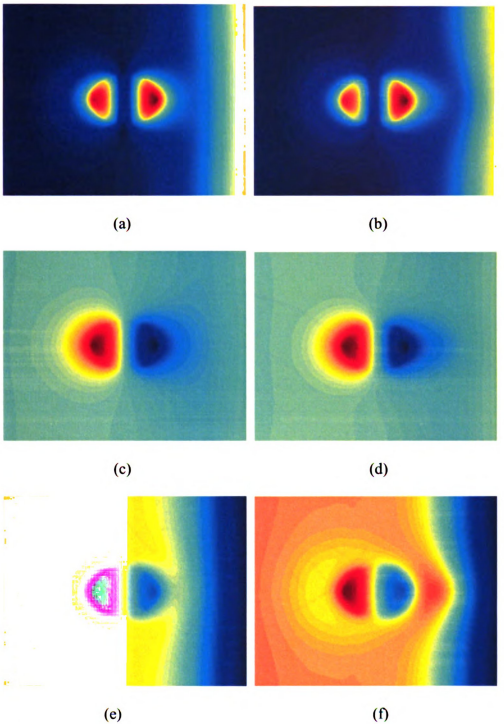


Figure 4.16 Frequency Parameter: simulation results at 700 Hz

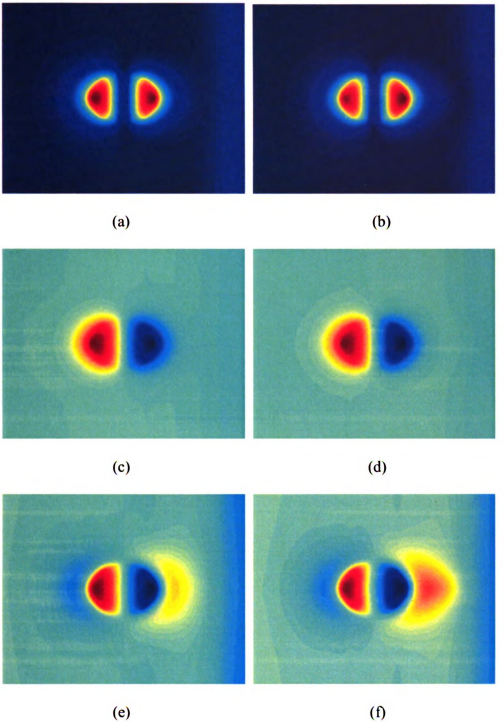


Figure 4.17 Frequency Parameter: simulation results at 2 kHz

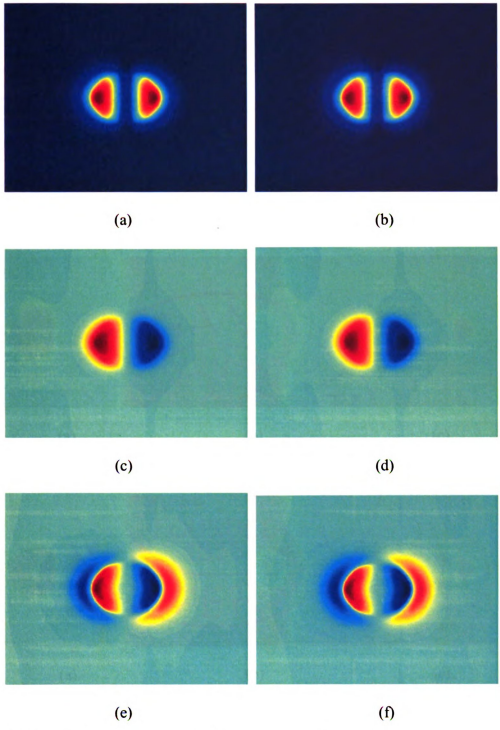


Figure 4.18 Frequency Parameter: simulation results at 7 kHz

### 4.4.2 Sensor Liftoff

The parametric effect of sensor lift-off on the signals was studied. Liftoff values varying from 0.0050, 0.0095, 0.0150, 0.1, 0.15, and 0.2 inches were considered. The geometry and finite element mesh of the test sample and sensor configuration are shown in Figures 4.8 and 4.9. A 0.3 inch second layer defect is introduced under the fastener.

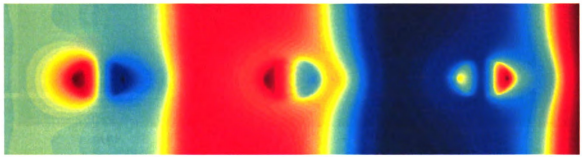

(a) (b) (c)

Figure 4.19 Liftoff Parameter: 0.0050 inch liftoff (a) real, (b) imaginary, (c) magnitude

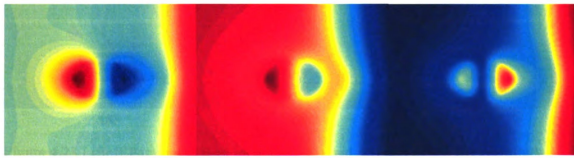

(a) (b) (c)

Figure 4.20 Liftoff Parameter: 0.0095 inch liftoff (a) real, (b) imaginary, (c) magnitude

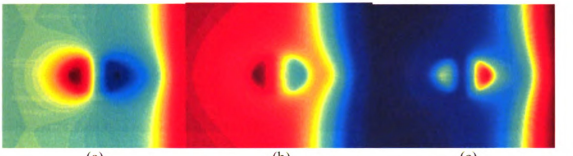

(a) (b) (c)

Figure 4.21 Liftoff Parameter: 0.0150 inch liftoff (a) real, (b) imaginary, (c) magnitude

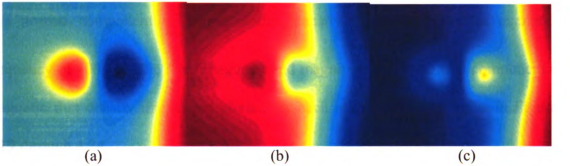

(a) (b) (c)

Figure 4.22 Liftoff Parameter: 0.1 inch liftoff (a) real, (b) imaginary, (c) magnitude

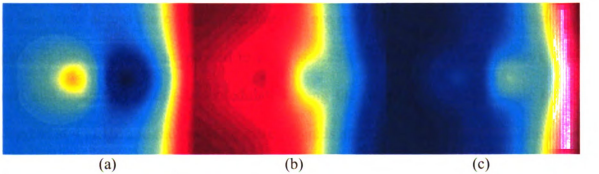

(a) (b) (c)

Figure 4.23 Liftoff Parameter: 0.15 inch liftoff (a) real, (b) imaginary, (c) magnitude

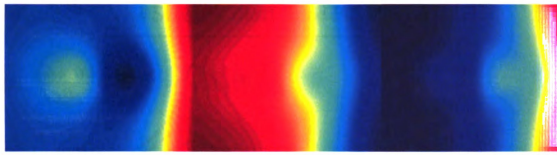

(a) (b) (c)

Figure 4.24 Liftoff Parameter: 0.2 inch liftoff (a) real, (b) imaginary, (c) magnitude

The normal component of magnetic flux density $B_z$ is calculated at excitation frequency of 400 Hz. The real, imaginary and magnitude of the normal component of magnetic flux density images are plotted for each individual liftoff value in Figures 4.19 through 4.24.

In order to see the variation in the signals with sensor liftoff, the peak to peak values in line scans across the center of the fastener are considered. The real and imaginary parts of the line scans are plotted in Figures 4.25 (Real) and 4.26 (Imaginary). The real and imaginary data are demodulated using the optimum detection angle of 70 degrees at 400 Hz and the resulting mixed signals are shown in Figure 4.27. The peak to peak values of $B_z$ (real, imaginary, magnitude and mixed) at each liftoff are listed in Table 4.2 and plotted in Figure 4.28.

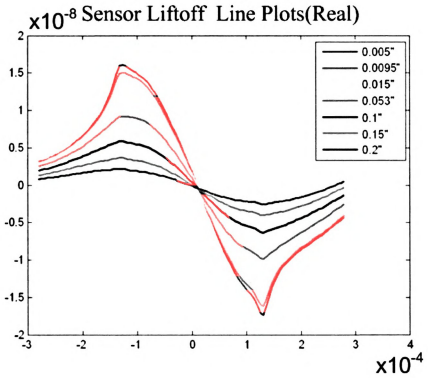


Figure 4.25 Line scans of real component (across the center of fastener)

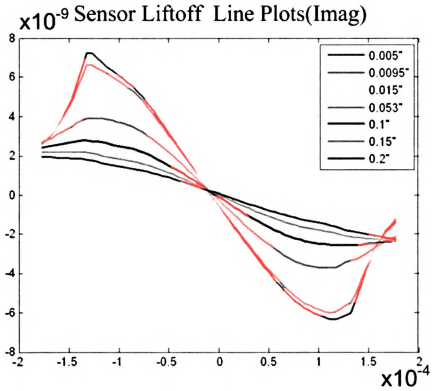


Figure 4.26 Line scans of imaginary component (across the center of fastener)

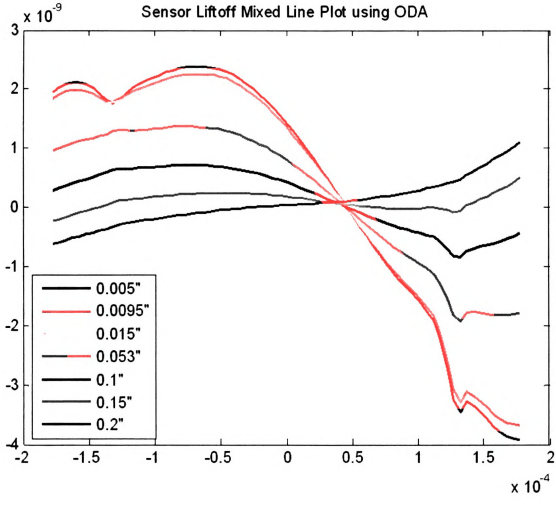


Figure 4.27 Mixed line scans using optimum detection angle (across the center of fastener)

Table 4.2 Peak to peak values of Magnetic flux density (z component) for various sensor liftoffs

| SENSOR LIFTOFF (INCH) | REAL COMPONENT (TESLA) | IMAGINARY COMPONENT (TESLA) | MIXED AFTER ODA (TESLA) |
|---|---|---|---|
| 0.005 | 3.3484e-008 | 1.3586e-008 | 6.3119e-009 |
| 0.0095 | 3.1232e-008 | 1.2620e-008 | 5.9523e-009 |
| 0.015 | 2.8929e-008 | 1.1657e-008 | 5.5312e-009 |
| 0.053 | 1.9075e-008 | 7.6667e-009 | 3.2867e-009 |
| 0.1 | 1.2221e-008 | 5.3627e-009 | 1.5625e-009 |
| 0.15 | 7.7481e-009 | 4.5275e-009 | 7.3745e-010 |
| 0.2 | 4.7604e-009 | 4.2386e-009 | 1.7312e-009 |

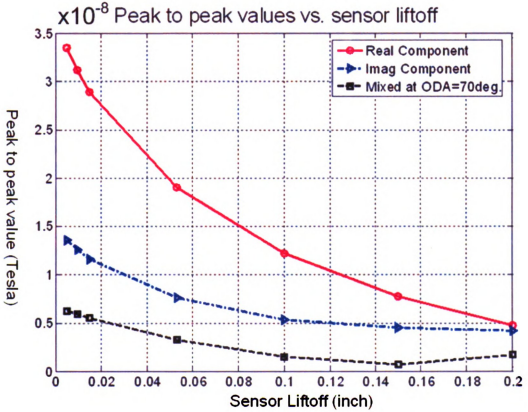


Figure 4.28 Peak values of Real, Imaginary, and Mixed MR signals vs. liftoff

### 4.4.3 Conductivity of Top Layer

The conductivity values for the top layer were selected according to the Parametric Table presented earlier. The operation frequency is chosen as 400 Hz and liftoff is chosen as 0.0050 inch. The nominal conductivity for top layer plate for test sample is 29.6% IACS, and the range of conductivity of the top layer plate is assigned values from 28% to 33% IACS. Figures 4.29 through 4.34 present simulation results of real, imaginary and magnitude values of the normal component of magnetic flux density for different values of top layer conductivity. Table 4.3 shows the peak value of the signal magnitude at different values of conductivity.

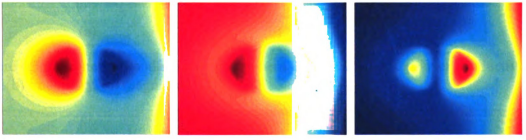

(a) (b) (c)

Figure 4.29 Magnetic flux density (z component) for 28% IACS top layer conductivity (a) real, (b) imaginary, (c) magnitude

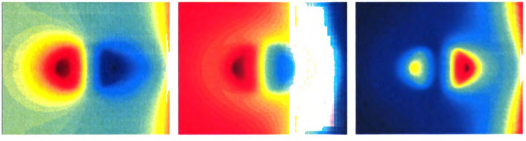

(a) (b) (c)

Figure 4.30 Magnetic flux density (z component) for 29% IACS top layer conductivity (a) real, (b) imaginary, (c) magnitude

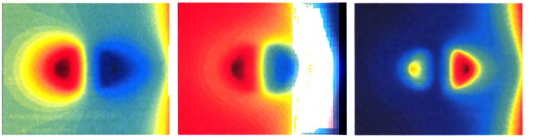

(a) (b) (c)

Figure 4.31 Magnetic flux density (z component) for 30% IACS top layer conductivity (a) real, (b) imaginary, (c) magnitude

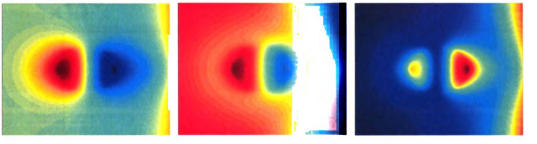

(a) (b) (c)

Figure 4.32 Magnetic flux density (z component) for 31% IACS top layer conductivity (a) real, (b) imaginary, (c) magnitude

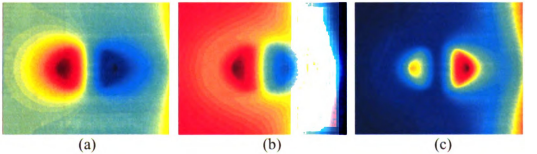

(a) (b) (c)

Figure 4.33 Magnetic flux density (z component) for 32% IACS top layer conductivity (a) real, (b) imaginary, (c) magnitude

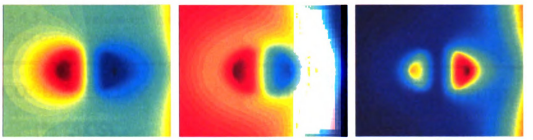

(a) (b) (c)

Figure 4.34 Magnetic flux density (z component) for 33% IACS top layer conductivity (a) real, (b) imaginary, (c) magnitude

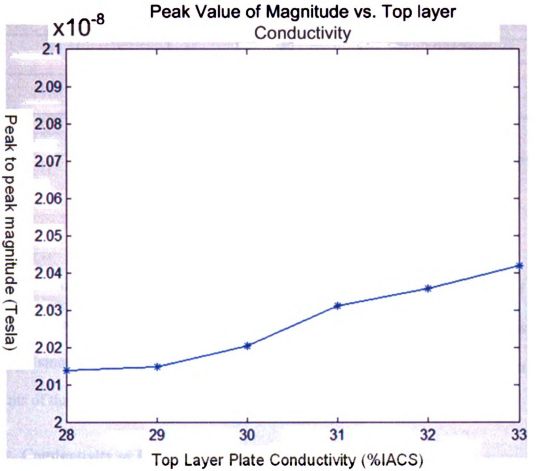


Figure 4.35 Peak value of the signal magnitude verses top layer plate conductivity

Table 4.3 Peak values of magnetic flux density (z component) Magnitude for various top-layer conductivity

| CONDUCTIVITY (% IACS) | CONDUCTIVITY (SIEMENS/M) | MAGNITUDE (TESLA) |
|---|---|---|
| 28 | 1.6240e7 | 2.0141e-8 |
| 29 | 1.6820e7 | 2.0150e-8 |
| 30 | 1.7391e7 | 2.0206e-8 |
| 31 | 1.7980e7 | 2.0312e-8 |
| 32 | 1.8560e7 | 2.0358e-8 |
| 33 | 1.9140e7 | 2.0419e-8 |

Figure 4.35 shows a plot of peak value of magnitude signal magnitude verses top layer plate conductivity.

From the results in Table 4.3 and the Figure 4.35, it is seen that the peak value of the signal increases slightly when top layer plate conductivity increases. This is as expected since increase in the top layer plate conductivity increases the induced eddy currents of that layer thereby increasing the amplitude of the measured signal.

### 4.4.4 Conductivity of Bottom Layer

The conductivity values for the bottom layer were selected according to the Parametric Table presented earlier. For bottom layer plate, the conductivity value ranges from 30% IACS to 36% IACS. The operation frequency is chosen as 400 Hz and liftoff is chosen as 0.0050 inch. The nominal conductivity for bottom layer is

taken as 33.5% IACS, and the range of the bottom layer conductivity is chosen to vary from 30% IACS to 36% IACS. Figures 4.36 through 4.42 present results of real, imaginary and magnitude value of the normal component of magnetic flux density for different values of bottom layer conductivity. Table 4.4 shows the peak value of the signal magnitude at different values of conductivity. Figure 4.43 shows the plot of peak value of the signal magnitude verses bottom layer plate conductivity.

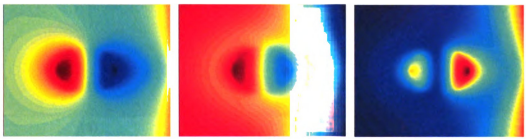

(a) (b) (c)

Figure 4.36 Magnetic flux density (z component) for 30% IACS bottom layer conductivity (a) real, (b) imaginary, (c) magnitude

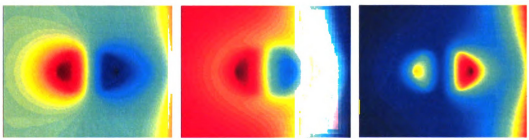

(a) (b) (c)

Figure 4.37 Magnetic flux density (z component) for 31% IACS bottom layer conductivity (a) real, (b) imaginary, (c) magnitude

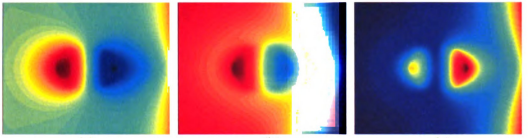

(a) (b) (c)

Figure 4.38 Magnetic flux density (z component) for 32% IACS bottom layer conductivity (a) real, (b) imaginary, (c) magnitude

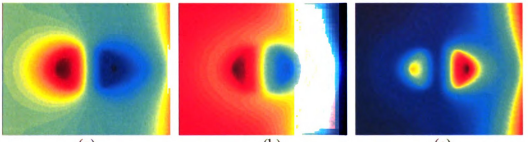

(a) (b) (c)

Figure 4.39 Magnetic flux density (z component) for 33% IACS bottom layer conductivity (a) real, (b) imaginary, (c) magnitude

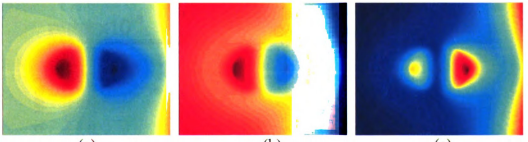

(a) (b) (c)

Figure 4.40 Magnetic flux density (z component) for 34% IACS bottom layer conductivity (a) real, (b) imaginary, (c) magnitude

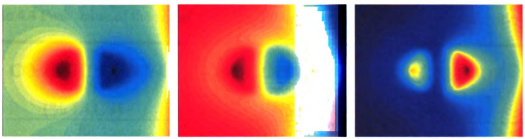

(a) (b) (c)

Figure 4.41 Magnetic flux density (z component) for 35% IACS bottom layer conductivity (a) real, (b) imaginary, (c) magnitude

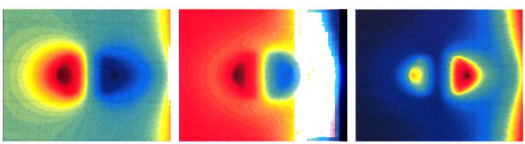

(a) (b) (c)

Figure 4.42 Magnetic flux density (z component) for 36% IACS bottom layer conductivity (a) real, (b) imaginary, (c) magnitude

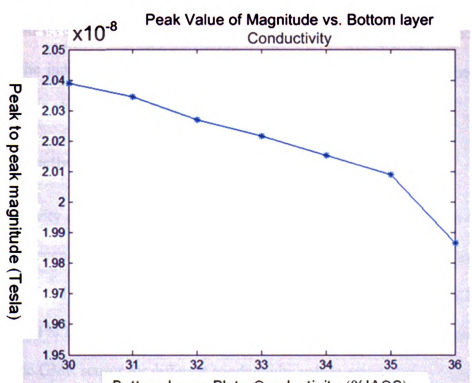


Figure 4.43 Peak value of the signal magnitude vs. bottom layer plate conductivity

Table 4.4 Peak value of the signal magnitude verses bottom layer plate conductivity

| CONDUCTIVITY (% IACS) | CONDUCTIVITY (SIEMENS/M) | MAGNITUDE (TESLA) |
|---|---|---|
| 30 | 1.7391e7 | 2.0390e-8 |
| 31 | 1.7980e7 | 2.0346e-8 |
| 32 | 1.8560e7 | 2.0271e-8 |
| 33 | 1.9140e7 | 2.0216e-8 |
| 34 | 1.9710e7 | 2.0153e-8 |
| 35 | 2.0290e7 | 2.0091e-8 |
| 36 | 2.0869e7 | 1.9867e-8 |

From the results presented above, it is seen that the peak value of the signal decreases when bottom layer conductivity increases. When the bottom layer plate conductivity increases, the induced eddy current becomes more concentrated around the bottom surface and the observed signal on the top surface is reduced.

### 4.4.5 Conductivity of Fastener

The conductivity of fastener was varied as described in the parameter Table 4.1. The operation frequency is chosen as 400 Hz and liftoff is chosen as 0.005 inch. The different conductivity values for the fastener were chosen to be 1.0% IACS, 2.2% IACS, and 3.1% IACS. The real, imaginary and magnitude values of magnetic flux density at the GMR sensor for different conductivity values are plotted in Figure 4.44.

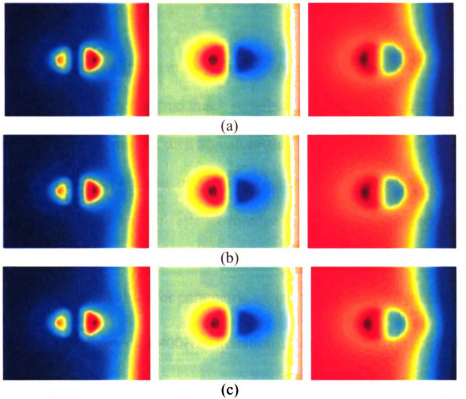

Figure 4.44 Magnitude, Real, and Imaginary components of magnetic flux density for conductivity values of Ti fastener: (a) 1.0% IACS, (b) 2.2% IACS, and (c) 3.1% IACS

The variation of the peak values are summarized in Table 4.5. The fastener conductivities considered in this study does not affect the signals with any significance.

Table 4.5 Effect of fasterner conductivity on peak values of signal magnitude

| FASTENER CONDUCTIVITY (% IACS) | MAGNITUDE (TESLA) |
|---|---|
| 1.0 | 2.0185e-008 |
| 2.2 | 2.0212e-008 |
| 3.1 | 2.0187e-008 |

### 4.4.6 Fastener to Edge Distance

A commonly encountered problem in airframe geometry is the influence of surface and subsurface edge on fastener and crack signals. The edge discontinuity behaves as a large defect and generates its own signature that can affect the defect signal and thereby lead to misinterpretation of GMR imaging data. This section describes a systematic study of the effect of fastener-to-edge distance on the defect signal. The edge is in the second layer and the nominal "fastener to edge" distance for test sample is 0.6 inch. The range of values for parametric variations is 0.4 to 0.8 inch.

Simulations were performed at 400Hz excitation frequency and 0.0095 inch lift-off. The normal component of the magnetic flux density $B_z$ is calculated at the prescribed liftoff and the resulting image data are plotted for each simulation. The real, imaginary, magnitude and demodulated images are presented. The demodulated image is derived using optimum detection angle (ODA) which is 70 degrees. Figures 4.45 to 4.49 show the real, imaginary, magnitude and demodulated images for varying "fastener to edge" distance in the range 0.4 to 0.8 inch.

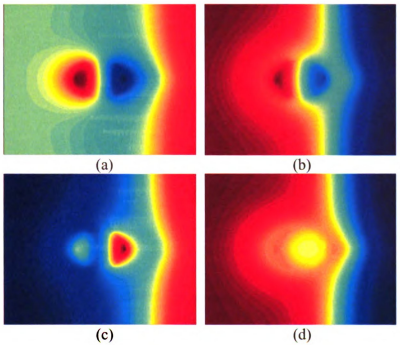


Figure 4.45 Real(a), Imaginary(b), Magnitude(c), Demodulated(d) magnetic flux density (z component) for fastener edge distance equals to 0.4 inch

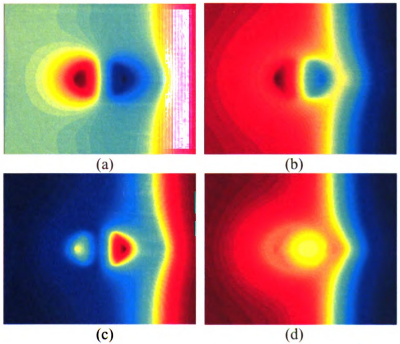


Figure 4.46 Real(a), Imaginary(b), Magnitude(c), Demodulated(d) magnetic flux density (z component) for fastener edge distance equals to 0.5 inch

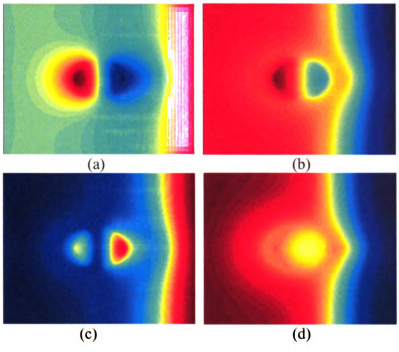


Figure 4.47 Real(a), Imaginary(b), Magnitude(c), Demodulated(d) magnetic flux density (z component) for fastener edge distance equals to 0.6 inch

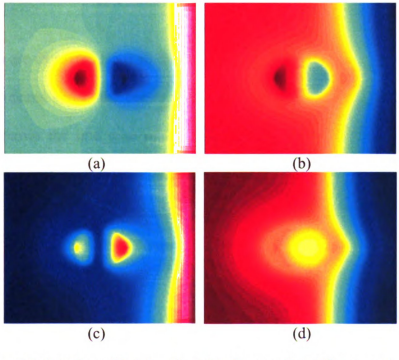


Figure 4.48 Real(a), Imaginary(b), Magnitude(c), Demodulated(d) magnetic flux density (z component) for fastener edge distance equals to 0.7 inch

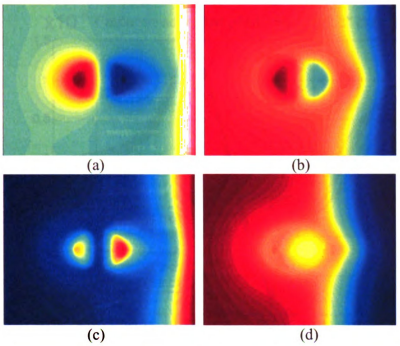


Figure 4.49 Real(a), Imaginary(b), Magnitude(c), Demodulated(d) magnetic flux density (z component) for fastener edge distance equals to 0.8 inch

The line plots are extracted from all the image data and plotted. Figures 4.50 and 4.51 show the line scans across the center of the rivet image of real and imaginary parts. Figure 4.52 shows the line scan of the demodulated signal using ODA. When the "fastener edge distance" increases, the edge effect on the right side of the fastener is decreased, so the magnitude of the signal on the right lobe will decrease slightly.

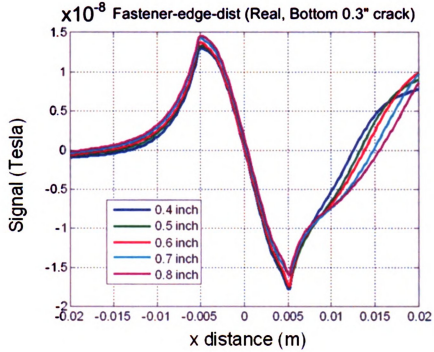


Figure 4.50 Line scans across the center of the fastener for real part of magnetic flux density (z component)

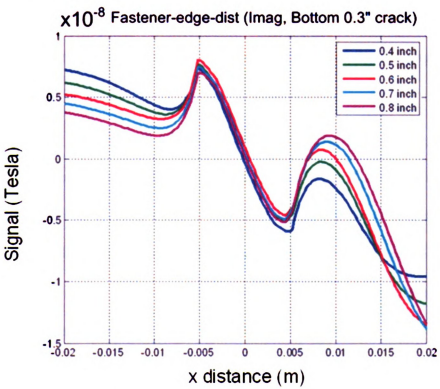


Figure 4.51 Line scans across the center of the fastener for imaginary part of magnetic flux density (z component)

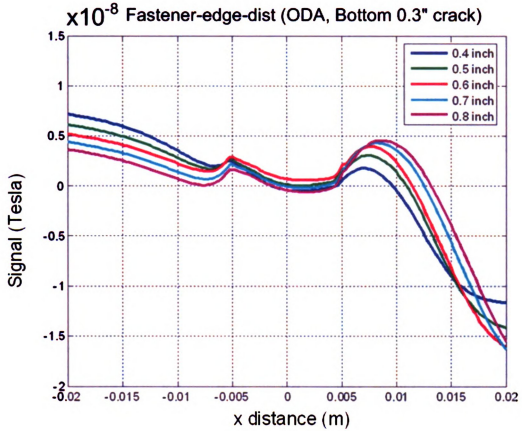


Figure 4.52 Line scans across the center of the fastener for mixed signal using ODA

To further examine the effect of edge on defect signal amplitude, the signal from a defective fastener for the largest fastener-to-edge distance is calculated and subtracted from the defect signal, in each case, at the defect location. Assuming that there is minimal effect on defect signal when the edge is the farthest, this value reflects the effect of an edge in the proximity of the fastener. The defect signal amplitude calculated in this manner is summarized in Table 4.6 and plotted in Figure 4.53.

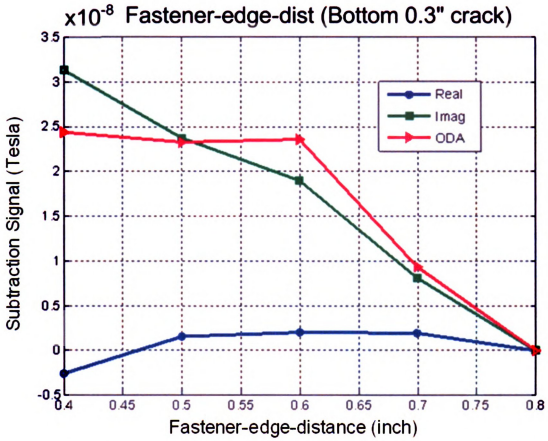


Figure 4.53 Edge effect on defect signal amplitude: Real, Imaginary, and Mixed signals vs. fastener-to-edge distance

Table 4.6 Peak to peak signal magnitude vs. fastener to edge distance

| FASTENER TO EDGE DISTANCE (INCH) | REAL COMPONENT (TESLA) | IMAGINARY COMPONENT (TESLA) | MIXED AFTER ODA (TESLA) |
|---|---|---|---|
| 0.4 | -0.2593 e-7 | 0.3132 e-6 | 0.2430 e-6 |
| 0.5 | 0.1501 e-7 | 0.2369 e-6 | 0.2326 e-6 |
| 0.6 | 0.2031 e-7 | 0.1898 e-6 | 0.2352 e-6 |
| 0.7 | 0.1908 e-7 | 0.0810 e-6 | 0.0936 e-6 |

From Figure 4.53, it is observed that the closer the fastener is to an edge the more effect on defect signal. The signal due to the edge adds to the defect signal which increases with proximity of fastener to the edge.

### 4.4.7 Crack Dimension

Four different trapezoidal crack dimensions were modeled including the case of a crack-free fastener. The radial dimensions of the top of crack top were chosen to be 0.2, 0.22, 0.25 and 0.3 inches. The crack geometry was tapered towards the bottom surface. The sensor liftoff was kept at 0.0095 inch and the frequency was chosen to be 500Hz. The normal component of the magnetic flux density Bz is calculated and plotted. The real, imaginary and magnitude of the complex flux density are plotted in Figures 4.54 through 4.58.

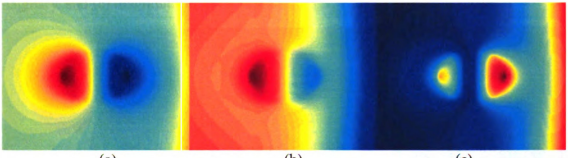

(a) (b) (c)

Figure 4.54 Magnetic flux density (z component) for 0.2 inch crack (a) real, (b) imaginary, and (c) magnitude

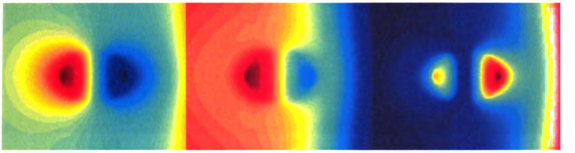

(a) (b) (c)

Figure 4.55 Magnetic flux density (z component) for 0.22 inch crack (a) real, (b) imaginary, and (c) magnitude

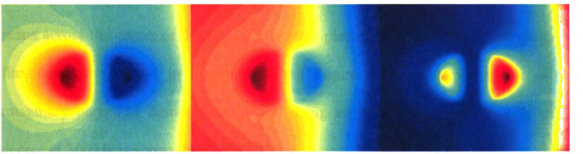

(a) (b) (c)

Figure 4.56 Magnetic flux density (z component) for 0.25 inch crack (a) real, (b) imaginary, and (c) magnitude

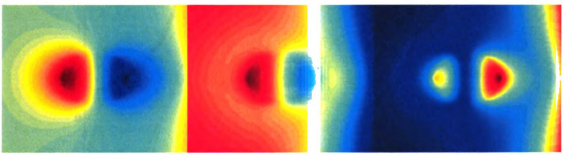

(a) (b) (c)

Figure 4.57 Magnetic flux density (z component) for 0.3 inch crack (a) real, (b) imaginary, and (c) magnitude

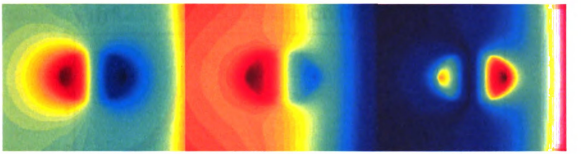

(a) (b) (c)

Figure 4.58 Magnetic flux density (z component) for no crack (a) real, (b) imaginary, and (c) magnitude

In order to see the variation in the signals with increasing crack dimensions, the line scans across the center of the fastener data are plotted. The real part of the magnetic flux density is shown in Figure 4.59 and Figure 4.60 shows the image of the imaginary part. The demodulated signal using an optimum detection angle of 70 degree at 500 Hz is shown in Figure 4.61.

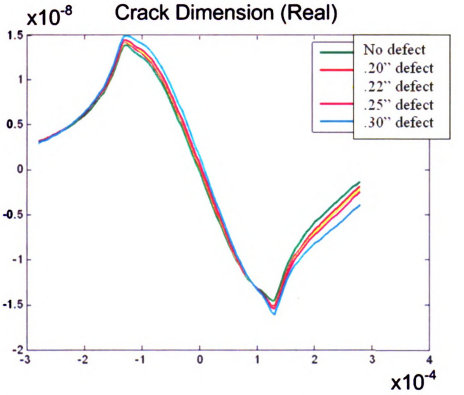


Figure 4.59 Line scans across the center of the fastener for real image data

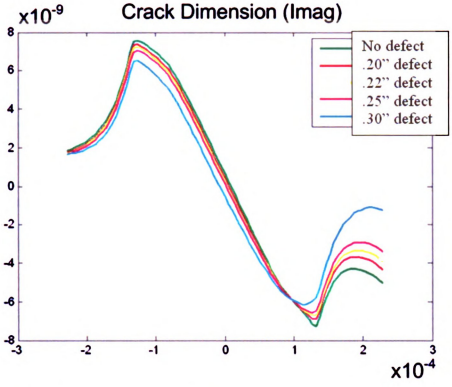


Figure 4.60 Line scans across the center of the fastener for imaginary image data

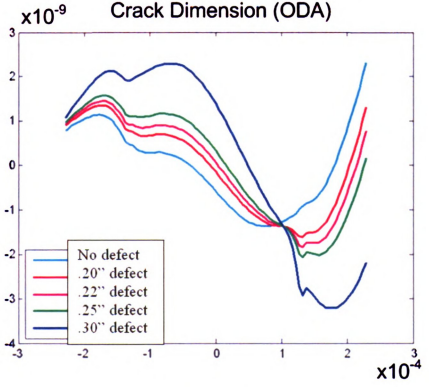


Figure 4.61 Mixed line scans using ODA of 70 degree

The defect signal amplitude is calculated using the peak-to-peak value of all three signals, real, imaginary, and mixed. The defect signal values are also re-calculated after subtracting the value obtained for the crack-free fastener. These values are summarized in Table 4.7 and plotted in Figure 4.62.

Table 4.7 Peak to peak values of Magnetic flux density (z component) for various crack dimensions after substracting the crack-free signal

| CRACK WIDTH ON TOP (INCH) | REAL COMPONENT (TESLA) | REAL COMPONENT (TESLA) | REAL COMPONENT (TESLA) |
|---|---|---|---|
| 0.2 | 9.89e-010 | -5.65e-010 | 4.49e-010 |
| 0.22 | 1.25e-009 | -8.58e-010 | 7.74e-010 |
| 0.25 | 1.508e-009 | -1.199e-009 | 1.1259e-009 |
| 0.3 | 2.612e-009 | -2.163e-009 | 3.0055e-009 |

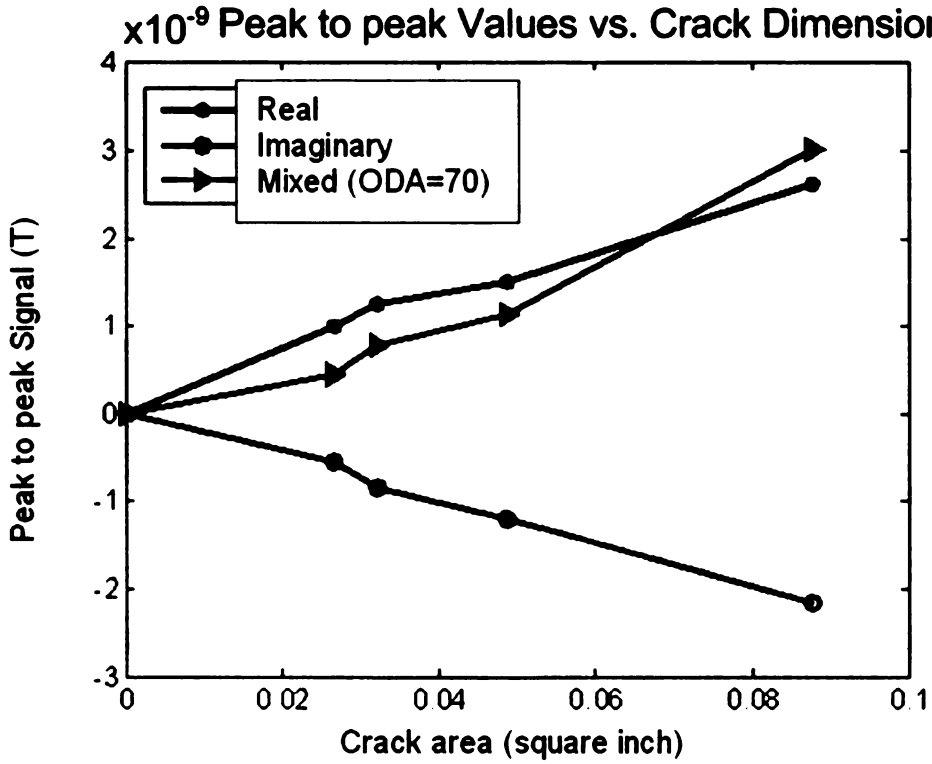


Figure 4.62 Peak-to-peak values of Real, Imaginary, and Mixed MR signals vs. crack area

### 4.4.8 Conclusions

The effect of parametric variations on the GMR measurements, presented in this Chapter can be utilized in optimization of the GMR imaging system. The parameters considered are frequency, sensor liftoff, conductivity of top and bottom layer, conductivity of fastener, fastener to edge distance, and crack dimensions effect. Some of these parameters are controllable, e.g., frequency, liftoff, and other parameters are uncontrollable (material conductivity, fastener tilt, etc.).

The study helps understand the effect of each parameter on the signal. As expected, the model does predict that the measured signal decreases when the sensor liftoff increases. Secondly, since the optimum detection angle is selected based on minimum

peak-to-peak value in the image data of the fastener, it is seen that in the mixed signals the overall spread in the peak value with parametric variation is lower that the variation in raw signal magnitude. This implies that the signal derived using optimum detection angle is relatively insensitive to parametric variations.

Studies on conductivity of sample conductivity show that the peak value of the signal increases when top layer conductivity increases. This is as expected since increase in the top layer conductivity increases the induced eddy currents of that layer thereby increasing the amplitude of the measured signal. When the conductivity of bottom layer increases, the induced eddy current becomes more concentrated in the bottom surface and the observed signal on the top surface is reduced. The fastener conductivities considered in this study does not affect the signals with any significance. In the case of fastener to edge distance, it is observed that the closer the fastener is to an edge the more effect on defect signal. The signal due to the edge adds to the defect signal which increases with proximity of fastener to the edge. Results from parametric study can be quantified in terms of skewness functions and probability of detection curves.

# CHAPTER 5. INVERSE PROBLEMS IN ELECTROMAGNETIC IMAGING

## 5.1 Introduction

The Chapter covers the various inversion techniques using in MO and GMR sensor data. Sections 5.2 to 5.5 present the inverse problems for MO imaging and Sections 5.6 to 5.7 present the corresponding results of inverse problems for GMR imaging. The objective of inverse problems is to detect second and third layer cracks in multilayer structures using MO and GMR sensor measurement.

## 5.2 Data Analysis for MO Imaging

The analysis of MO imaging uses skewness functions defined for quantifying the asymmetry of MO image. These functions are used in classifying a rivet as defect-free or with defect. Classification algorithms were developed and optimized using simulation data obtained via finite element models and the performance was evaluated on experimentally measured MO images thereby substantiating the validity of the skewness definitions and its usefulness in developing automatic MOI classification system.

### 5.2.1 Automatic Rivet Detection

The overall approach for automated rivet classification is depicted in Figure 5.1. The raw image obtained from the MOI image acquisition system is applied to the motion-based filterer [32][33] to remove the background noise associated with domain structures in the MO sensor. The filtered image is enhanced and thresholded to obtain a binary image, which is used in the subsequent rivet detection and classification modules.

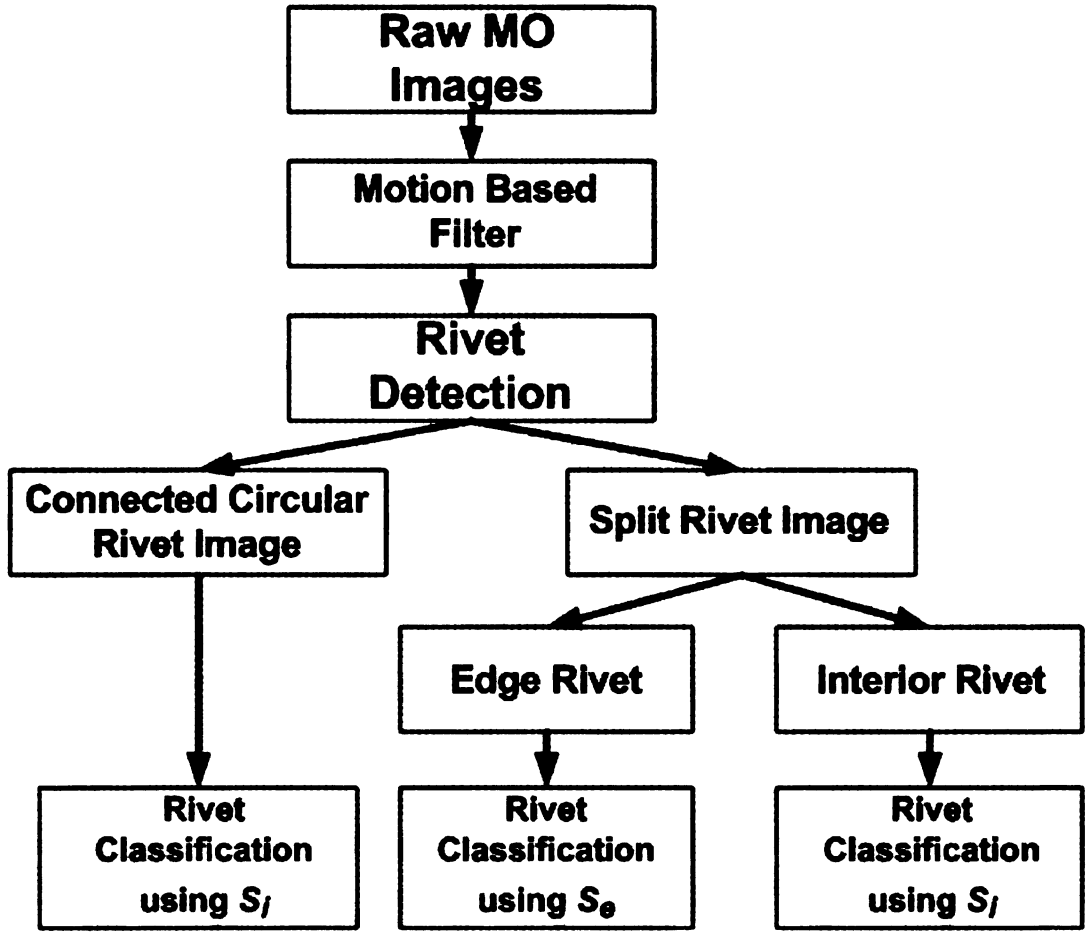


Figure 5.1 The overall approach for automated rivet classification

The detection and classification of a rivet is based on the skewness value associated with the binary image. The rivet center detection is performed using one of two different approaches, namely Hough transformation and morphological image processing [31]. All the classification results in this dissertation are obtained using the morphological image processing operators of dilation and erosion with varying structural elements [2]. Asymmetry quantification is first performed using skewness feature of the data. The ideal rivet image is circular and hence its skewness must be zero. If the computed skewness value is greater than some tolerance, the rivet is classified as defective; otherwise the rivet site is deemed good.

### 5.2.2 Skewness Definition and automated classification

The skewness of the circular MOI rivet image and skewness quantification plays a critical role in the automatic rivet classification. The skewness function should capture the deviation from circularity of the rivet image, be robust under small variations in the measured image and at the same time have discriminatory information between good and defective rivets. This dissertation investigates several definitions of skewness associated with an MO image.

#### *5.2.2.1 Skewness function $S_1$*

The first definition studied was designed to be independent of the frequency of inspection and is expressed as:

wh

or S

ne

th

ad

re

Fig

$$S_1 = \frac{f^{1/3}}{100} \frac{R}{R+B} \frac{\sum_i (D_i - r)^2}{r^2 + \sum_i (D_i - r)^2} \tag{5.1}$$

where $f$ is the frequency parameter which is 50 kHz for the surface defects and 1.5, 3 or 5 kHz for subsurface defects. Here, $B$ is the 'width' of the region outside the rivet in the image, $r$ is the average measured radius of rivet and $\{D_i, i = 1,2,\ldots n\}$ are the distances from the rivet center to the edge pixels. Finally, $R$ is computed by calculating the histogram of $D_i$ and picked at its peak location. All these parameters are illustrated in Figure 5.2.

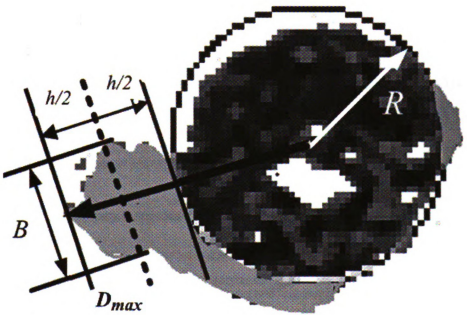


Figure 5.2 Feature Parameters definition in skewness function $S_1$

#### 5.2.2.2 *Skewness function $S_2$*

The second definition of skewness function that was studied is based on the auto-covariance function, cov($D_i$, $D_j$) of the series $\{D_i\}$. The vector-valued skewness function is derived from features in the auto-covariance plot and is hence defined in a two or higher dimensional space for improved separability between classes. Consider a set of $n$ distances denoted by$\{ D_1 D_2 ,D_3 ,\ldots, D_n \}$, as illustrated in Figure 5.3 in which the circle represents the boundary of the binary MO image of a rivet.

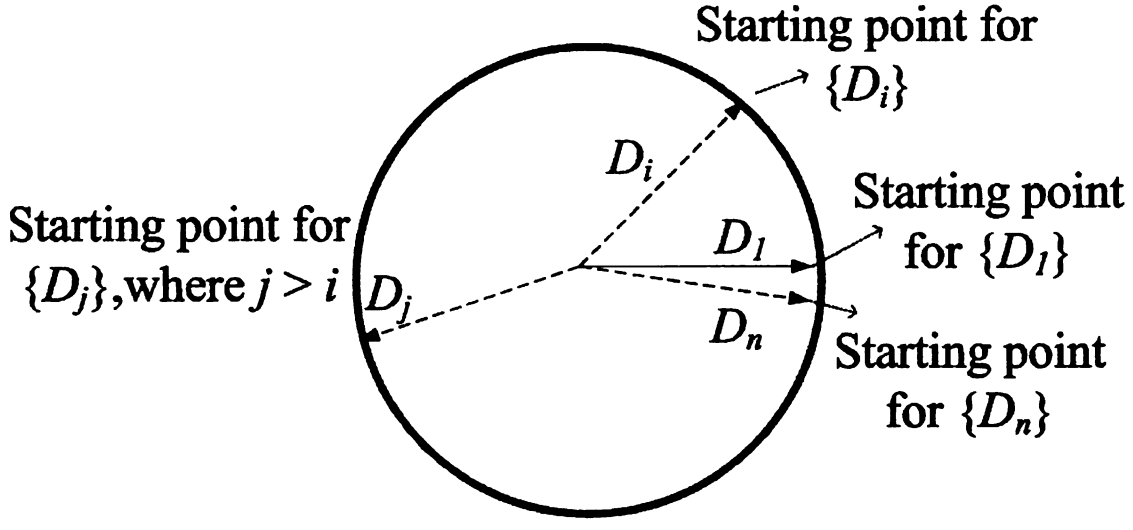


Figure 5.3 A set of boundary distances defined in skewness function $S_2$

The continuous form of normalized covariance definition is as follows:

$$\mathrm{cov}(\theta') = \frac{\int_0^{2\pi} (D(\theta) - r)(D(\theta + \theta') - r) d\theta}{\int_0^{2\pi} D(\theta)^2 d\theta} \tag{5.2}$$

The corresponding discrete form of normalized covariance definition is given by

$$Cov(\theta_k) = \frac{\sum_{i=1}^{n}(D(\theta_i)-r)\cdot(D(\theta_i+\theta_k)-r)\delta\theta_i}{\sum_{i=1}^{n}D^2(\theta_i)\delta\theta_i} \tag{5.3}$$

where $\theta_k = \theta_{k-1} + \delta\theta_k$, $\delta\theta_i$ is the incremental angle between $D_{i+1}$ and $D_i$, and the initial angle $\theta_0$ is set to 0. Typical auto-covariance curves of the series $\{D_i\}$, derived from MO images are shown in Figure 5.4. Three skewness parameters are derived from the auto-covariance function, namely, Central Peak Ratio (CPR), Noise to Signal Ratio (NSR) and Central Peak Width (CPW), shown in Figure 5.4. CPR is the ratio between the central peak height $H_{CP}$ and total height of the covariance curve $H_T$, defined as:

$$CPR = \frac{H_{CP}}{H_T} \tag{5.4}$$

CPW is the width of the central peak at its 50% peak value. NSR is the noise to signal ratio defined from continuous form of normalized covariance definition:

$$NSR = \frac{\int_0^{2\pi}(D(\theta)-r)(D(\theta)-r)d\theta}{\int_0^{2\pi}D(\theta)^2 d\theta} \tag{5.5}$$

which is also the first point of the covariance curve cov(0).

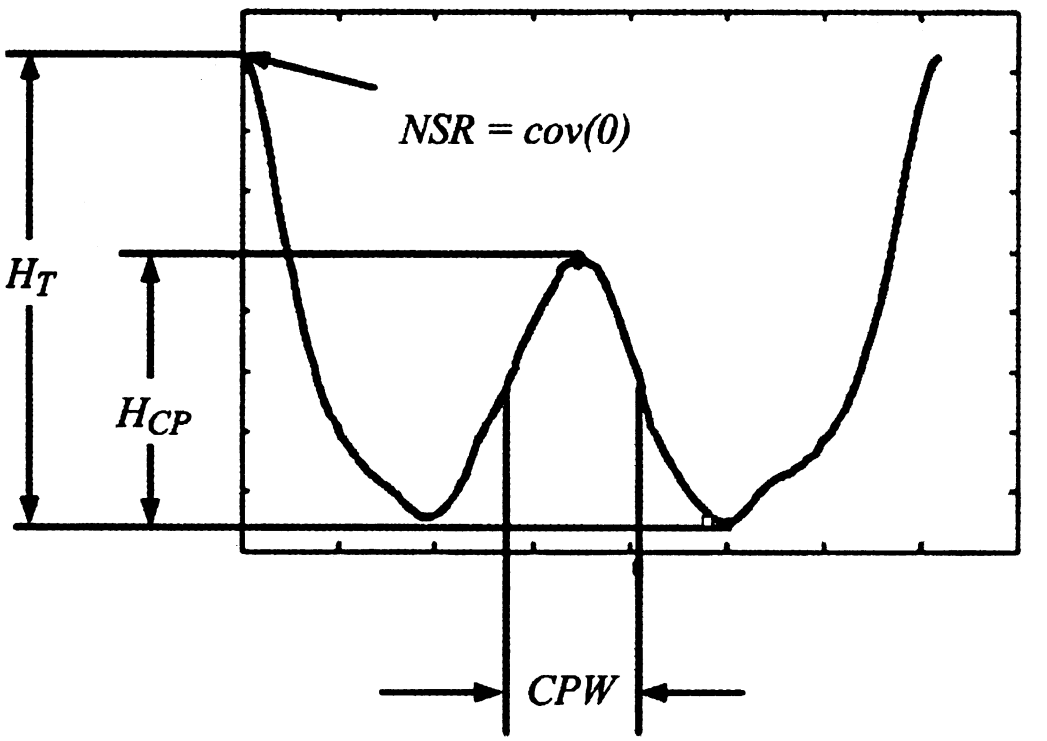


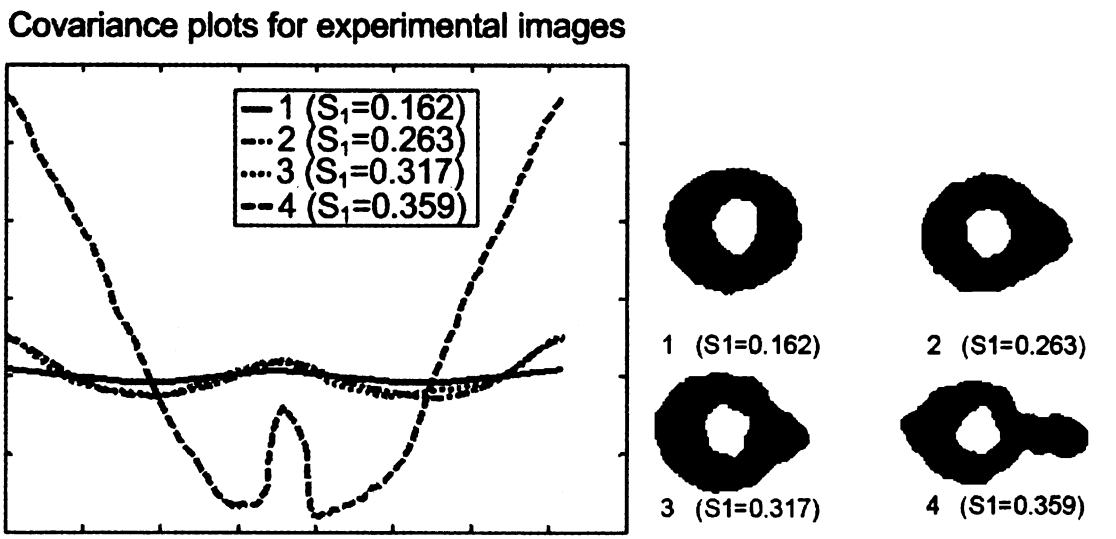


Figure 5.4 Parameters definition in skewness function $S_2$ and corresponding results

Using these skewness parameters, a 2D feature space spanned by CPR and NSR or a 3D feature space spanned by CPR, CPW and NSR can be constructed, where the coordinates in 2D space is (CPR, NSR) and in 3D space is (CPR, CPW, NSR). In

the 2D feature space, according to the definition and characteristic of the MOI binary images, it is seen that for small defects the value of CPR is close to 1.0; also, the value of NSR is proportional to the size (radial length) of the crack. The skewness vector values in this case are defined based on the multi-dimensional coordinates,

$$S_2 = \begin{cases} (CPR, NSR) & for \quad 2D \quad space \\ (CPR, NSR, CPW) & for \quad 3D \quad space \end{cases}$$

(5.6)

#### *5.2.2.3 Skewness function $S_3$*

A third definition of skewness is based on the normalized central moments of two-dimensional (2D) binary valued rivet images [2]. For a 2D digital image function *I(x,y)*, the discrete central moment can be expressed as:

$$\mu_{pq} = \sum_x \sum_y (x_i - \bar{x}_c)^p (y_j - \bar{y}_c)^q I(x, y)$$

(5.7)

where $(\bar{x}_c, \bar{y}_c)$ is the center of the MO rivet image obtained using the morphological image processing operators of dilation and erosion. For the binary valued rivet images after enhancement and thresholding, *I(x,y)* is simplified to

$$I(x, y) = \begin{cases} 1 & (x_i, y_j) \quad is \quad image \quad pixel \\ 0 & otherwise \end{cases}$$

(5.8)

The normalized central moments, denoted $M_{pq}$, is then computed as

$$M_{pq} = \frac{\mu_{pq}}{\mu^{\gamma}_{00}}$$

(5.9)

where $\gamma = \frac{p+q}{2} + 1$, for $p+q = 2,3,\ldots.$

The skewness function $S_3$ was chosen from the various normalized central moments, based on their discriminatory abilities, as the vector S3 in Equation 5.10:

$$S_3 = \{M_{20}, M_{22}, M_{40}\}$$

(5.10)

#### *5.2.2.4 Skewness Function $S_e$*

In the case of the distorted rivet image close to a structural discontinuity, we define the skewness feature as:

$$S_e = k\left(\frac{|A_1 - A_2|}{A_1 + A_2} + \frac{|X_m - Y_m|}{X_T}\right)$$

(5.11)

where $k$ is a scaling factor so that the skewness values for edge rivet images are in the same range as that of interior rivet images. In the current classification procedure, we set $k$ = 0.5. $A_1$ and $A_2$ are the areas of the two largest lobes. $X_m$ and $Y_m$ are the dimensions of the largest lobe calculated from the center in the x and y direction respectively, and $X_T$ is the total dimension of lobes in the x direction.

## 5.3 MO Image Classification

The rivet detection and classification algorithms were applied to experimental video data obtained from scanning rivets on an aircraft panel using the MOI 303 instrument [27][28][29]. The video data was first segmented into single rivet images, which were, then analyzed using the automated signal classification algorithm. The classification results using the skewness functions $S_1$ and $S_2$ are shown in 1, 2 and 3 dimensional skewness spaces in Figure 5.5. The skewness feature corresponding to good rivets are represented by the circles and data points corresponding to cracked rivet images by triangles. It is seen that overlap in the 1D space of $S_1$ is eliminated in the higher order feature space. In the multi-dimensional skewness spaces the classes are better separated and hence provide more accurate detection and classification performance.

Figure 5.5 Classification results in multi-dimensional skewness space: (a) 1D Space (b) 2D Space (c) 3D Space

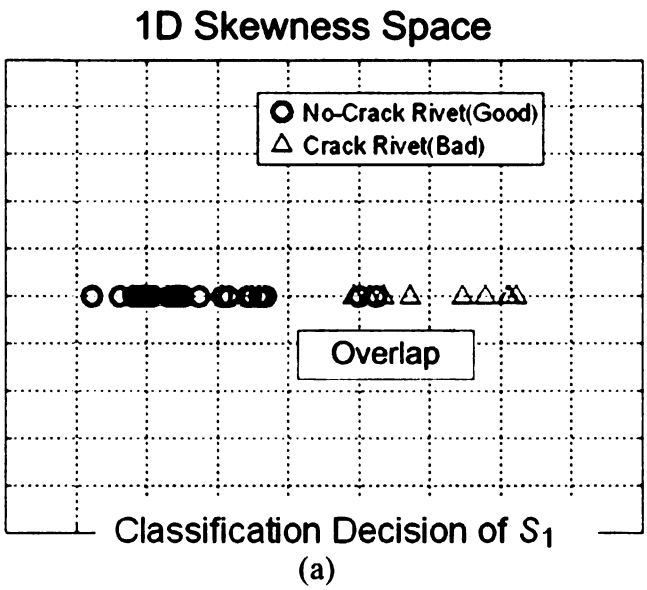


(a)

Figure 5.5 continued

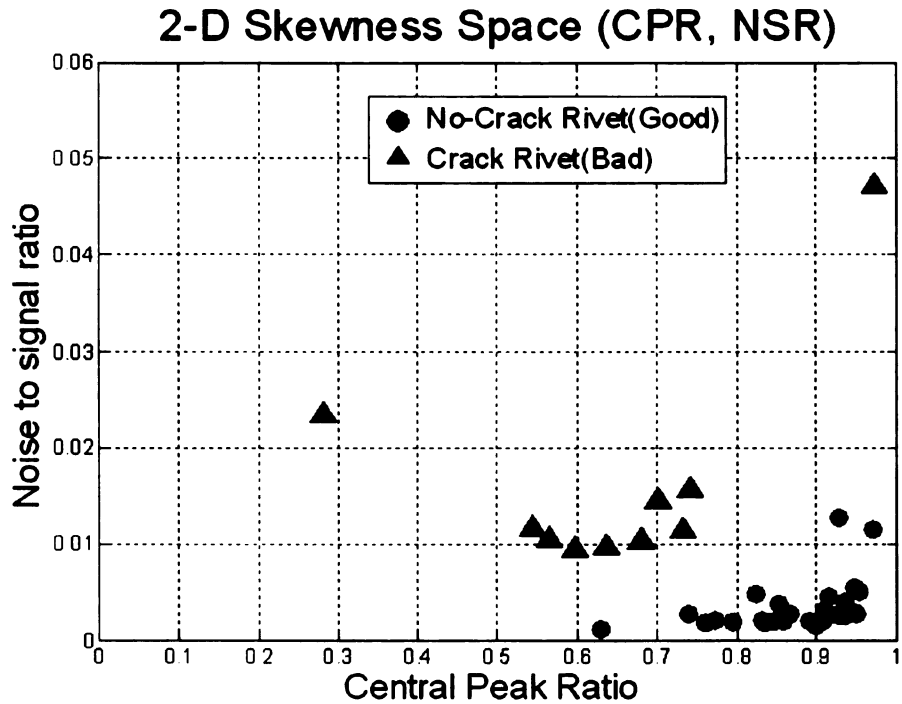


(b)

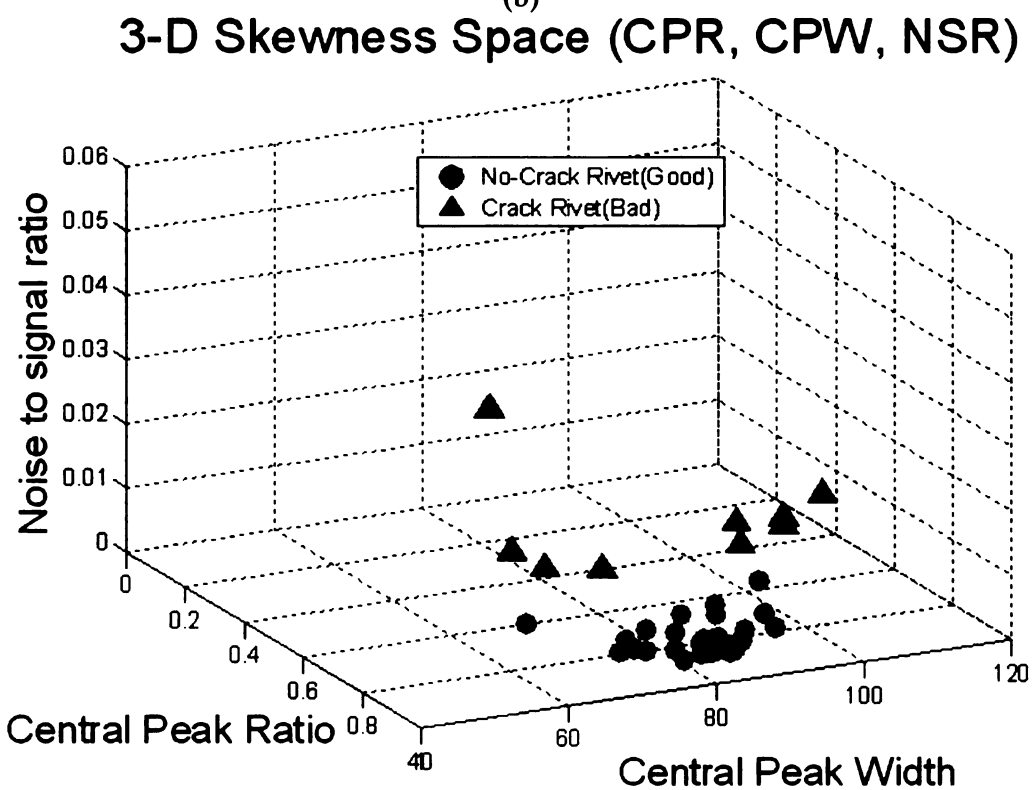


(c)

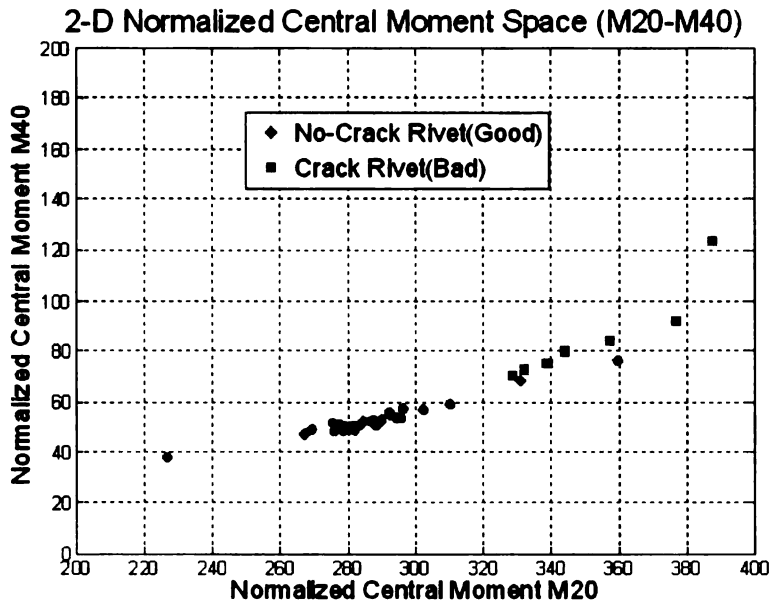


(a)

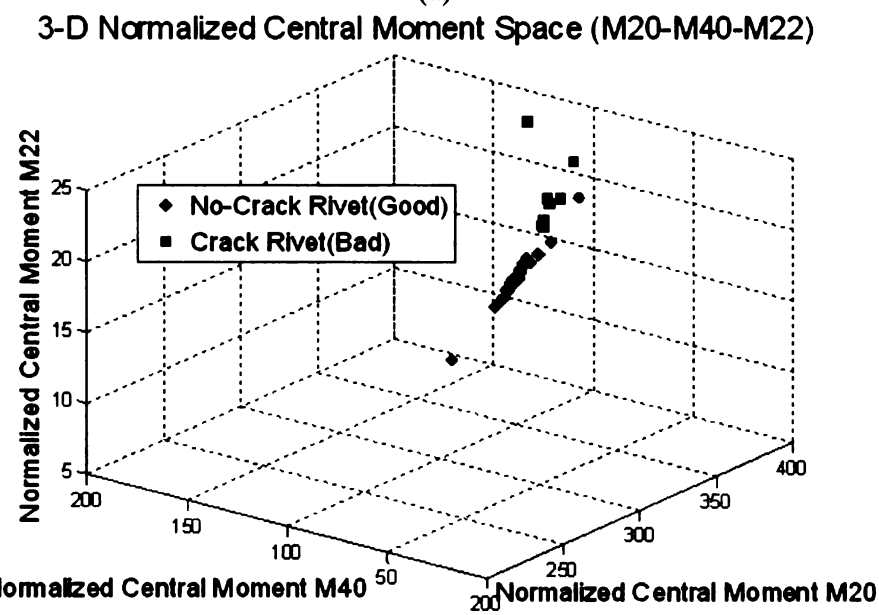


(b)

Figure 5.6 Classification results in normalized central moment space: (a) M20-M40 Space (b) M20-M40-M22 Space

The classification results using the normalized central moment vectors are shown in Figure 5.6. The moments corresponding to good rivets are represented by the circles and data points corresponding to cracked rivet images by squares. The advantage of moment-based features is that it is intuitive and allows fast computation. These results

have also been extended to the calculation of Probability of Detection (POD) of critical flaws along with the associated Probability of False alarm (PFA). The definitions of POD and PFA for the binary image are defined as:

$$POD = \frac{\sum_{i=1}^{N} \alpha_i}{N} \times 100\% \tag{5.11}$$

$$PFA = \frac{\sum_{i=1}^{N} \alpha_i^*}{N^*} \times 100\% \tag{5.12}$$

where $N$ and $N^*$ are the total number of data points corresponding to flawed and good rivet images respectively and $\alpha_i$ , $\alpha_i^*$ are the corresponding classification decisions of the automated rivet classification system. $\alpha_i$=1 implies that the rivet image is classified as flawed where as $\alpha_i$=0 means it is a good rivet. For real aircraft rivet images, statistical analysis was performed using the "POD Version 3.0" software [36], which is a C++ program that interacts with a Microsoft Excel 97 workbook to perform a POD analysis on the results with varying threshold values of $S_1$. When the value of $S_1$ is greater than or equal to the classification thresholds, the rivet site was classified as having a crack. POD plots with varying classification threshold values are shown in Figure 5.7.

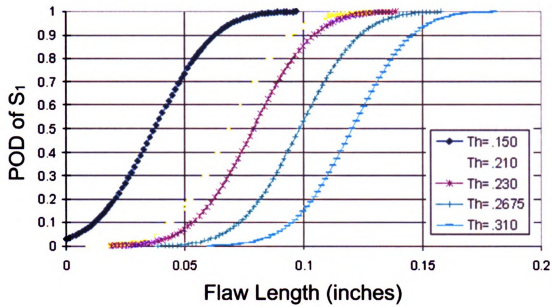


Figure 5.7 POD curves from response data of automated MOI inspections of surface layer cracks around fasteners

POD curves are presented for four different threshold settings, which show how the POD increases with reduction in threshold settings. However it should be kept in mind that the PFA values also increases with increasing POD. The Receiver Operator Curve (ROC) for different flaw sizes a is shown in Figure 5.8.

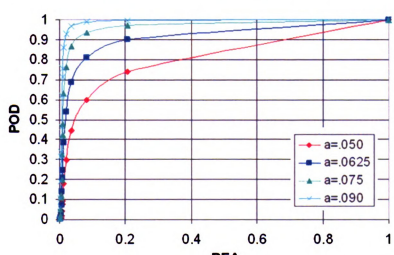


Figure 5.8 ROC curves for Automated MOI on surface cracks with different flaw size a

POD plots for hit/miss data from Automated MOI inspections of surface cracks are presented in Figure 5.9 from the multi-flaw model fits. Note that both 2-parameter and 4- parameter fits were performed. For S1 method, a threshold of 0.210 achieved a 0.9 POD value and a false call rate of about 1% for a flaw of length 0.094 inches. A threshold of 0.150 achieved a 0.9 POD value and a false call rate of almost 21% for a 0.063 inches crack. The $S_2$ method can achieve the same POD value and was shown that it was effective in removing the false calls being made at edges. More image processing and classification results are shown in Figure 5.10 to Figure 5.12. The connected circular images are recognized as interior ones, while split images can be recognized by the proportion of $A_1/A_2$ ($A_1 \leq A_2$) as either rivet images close to the edge when $A_1/A_2$ is great than 0.4 or interior rivet images otherwise. Skewness features $S_i$ and $S_e$ are then applied respectively.

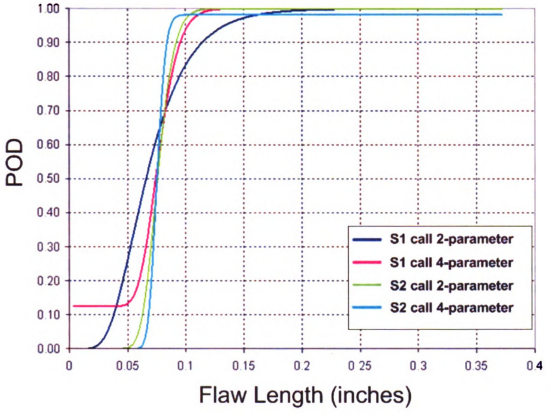


Figure 5.9 POD fits for Automated MOI inspections of surface cracks. (POD for $S_1$ (dark, red), for $S_2$ (green, blue), both 2-parameter and 4-parameter fits were performed)

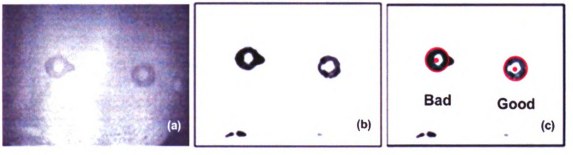


Figure 5.10 Three-step characterization for surface interior MO images (a) raw images (b) enhanced images using motion-based filtering (c) detection and classification of images

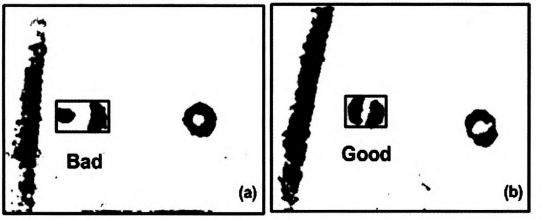


Figure 5.11 Characterization for structural surface edge MO images (a) bad edge rivet image detection and classification (b) good edge rivet image detection and classification

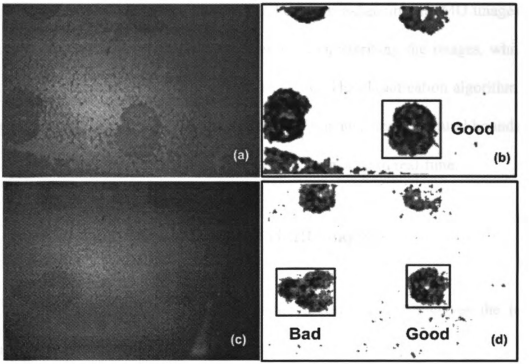


Figure 5.12 Characterization for subsurface interior MO images obtained under 5 kHz frequency and various intensities of magnetic field: (a)-(b) are raw and classified images (high intensity), (c)-(d) are raw and classified images (low intensity)

## 5.4 Inverse Problems of MO imaging Conclusion

This dissertation addresses some of the issues in automatic classification of MO imaging data for aircraft inspections. Three definitions of skewness functions are investigated to automatically quantify and classify aircraft defects. The moment based method is computationally fast and the classification performance is as good as S1 method. The classification algorithms have been tested on experimentally measured MOI aircraft rivet images and were shown to be robust. The performance of the algorithm has been quantified in terms of the POD and PFA values.

The advantages of this method are that in addition to enhancing the MO images, the technique also provides a quantitative basis for characterizing the images, which in turn will yield consistent reject or accept decisions. The classification algorithm also reduces the false calls due to the distortion of MO images near structural boundaries. The overall automated classification system is implemented in real-time.

## 5.5 Inversion and Data analysis for GMR imaging

The inversion for GMR imaging data in the follow sections involves the image classification, enhancement and characterization.

### 5.5.1 Optimization of Frequency Parameter in model predition - Skewness Calculations

Although the defect indication is visible in most of the images, a simple method for determining the optimum value of frequency is presented in this section via a quantitative measure of the asymmetry in the two lobes of the image. A simple skewness function for quantifying the asymmetry is calculated based on the peak values of the two lobes of the fastener image, and is defined in Equation 5.13.

$$S_a = \frac{\max\{|B_1|,|B_2|\}}{\min\{|B_1|,|B_2|\}} \tag{5.13}$$

The parameters of this function are shown pictorially in Figure5.13. The value of $S_a$ is calculated for the fastener image obtained at each frequency and is plotted in Figure 5.14.

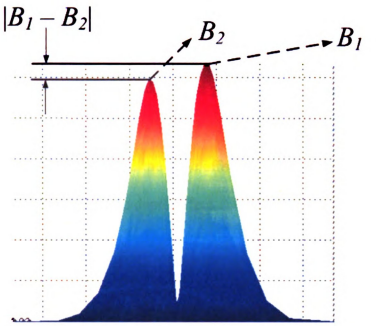


Figure 5.13 Surface plot of the image data showing the asymmetry in two lobes of fastener image

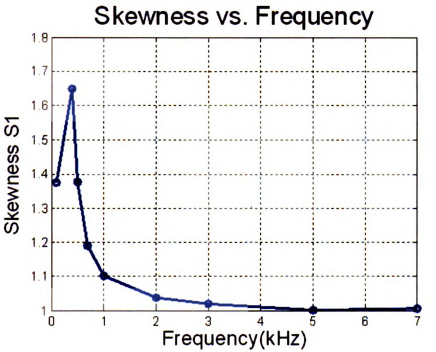


Figure 5.14 Skewness vs. Frequency for results with 0.3" crack

From Figure 5.14 it is seen that at lower frequencies the skewness values are much higher than 1 and the crack is easily detected. At higher frequency, the crack is hard to see due to the skin depth effect. The skewness plots show that the optimal operating frequency is 0.4 kHz. Further, the modeling results indicate that as the frequency increases, the images are sharper and the edge effect vanishes, but the crack detection ability decreases because of the skin depth effect.

### 5.5.2 Optimization of frequency parameter in model prediction-SNR Calculations

An alternate method for optimizing frequency of operation is to select a frequency that maximizes the POD or equivalently the SNR of the signal. In this study, SNR values are calculated with simulation results obtained at frequencies: 100Hz, 400Hz, 500Hz, 700Hz and 1000Hz. Both crack-free fastener and the case of a fastener with 0.3 inch subsurface crack were simulated. The fastener image at each frequency is analyzed using the procedure described in section 5.5.1. The image data was preprocessed using the optimum detection angle at each frequency and the line scans across the center of the fastener was extracted. The MAE and MSE feature defined in Equations 5.14 and 5.15 using experimental data from test sample are applied for simulated signal.

$$F_{MAE} = \frac{1}{N}\sum_{i=1}^{N}\left|L_D[i] - \frac{1}{M}\sum_{j=1}^{M} L_{ND\_j}[i]\right| \tag{5.14}$$

$$F_{MSE} = \frac{1}{N}\sum_{i=1}^{N}(L_D[i] - \frac{1}{M}\sum_{j=1}^{M}L_{ND\_j}[i])^2$$

(5.15)

$F_{MAE}$ is the feature calculated from mean absolute error and the $F_{MSE}$ is calculated from mean square error. In Equations 5.14 and 5.15, $N$ is the length of the mixed 1D data vector, $M$ is the total number of non-defective rivets. $L_D$[i] is the ith pixel of mixed data for different frequencies and $L_{ND\_j}$[i] is set to zero vector as the baseline signal. The line scans at different frequencies for the 0.3" subsurface crack signals are shown in Figure 5.15.

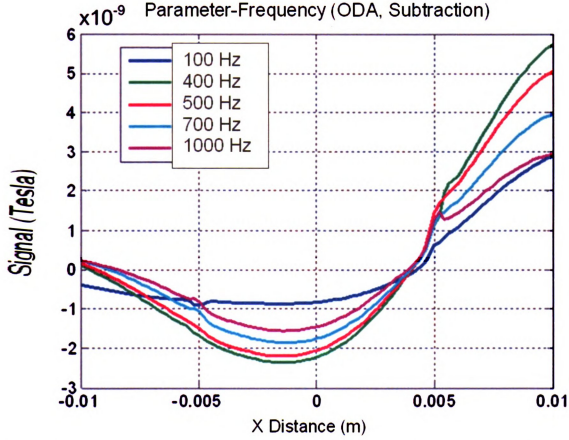


Figure 5.15 Simulated line scans at different frequencies for 0.3" subsurface cracks after ODA processing

The SNR definition used earlier is modified. The definition used in analyzing experimental data is provided in Equation (5.16). The modified equation for analysis of simulated data is given in (5.17), where the mean and variance are set to 0 and 1 respectively.

$$SNR_M = \sqrt{\sum_{i=1}^{M} (F_i - m_{0i})^2 \Big/ \sigma_{0i}^{\,2}} \tag{5.16}$$

$$SNR_M = \sqrt{\sum_{i=1}^{M} F_i^2} \tag{5.17}$$

where $M = 2$ in this case.

A scatter plot of 2D feature vector in the feature space is shown in Figure 5.16. A classification rule can be devised based on partitioning the defect free fastener (green dot) from the feature vector corresponding to the 0.3 inch crack data (red triangle). The SNR value is proportional to Euclidean distance between (0, 0) and the feature at each frequency. The SNR vs. frequency plots are shown in Figure 5.17 and it is seen that the SNR is maximized at 400Hz frequency.

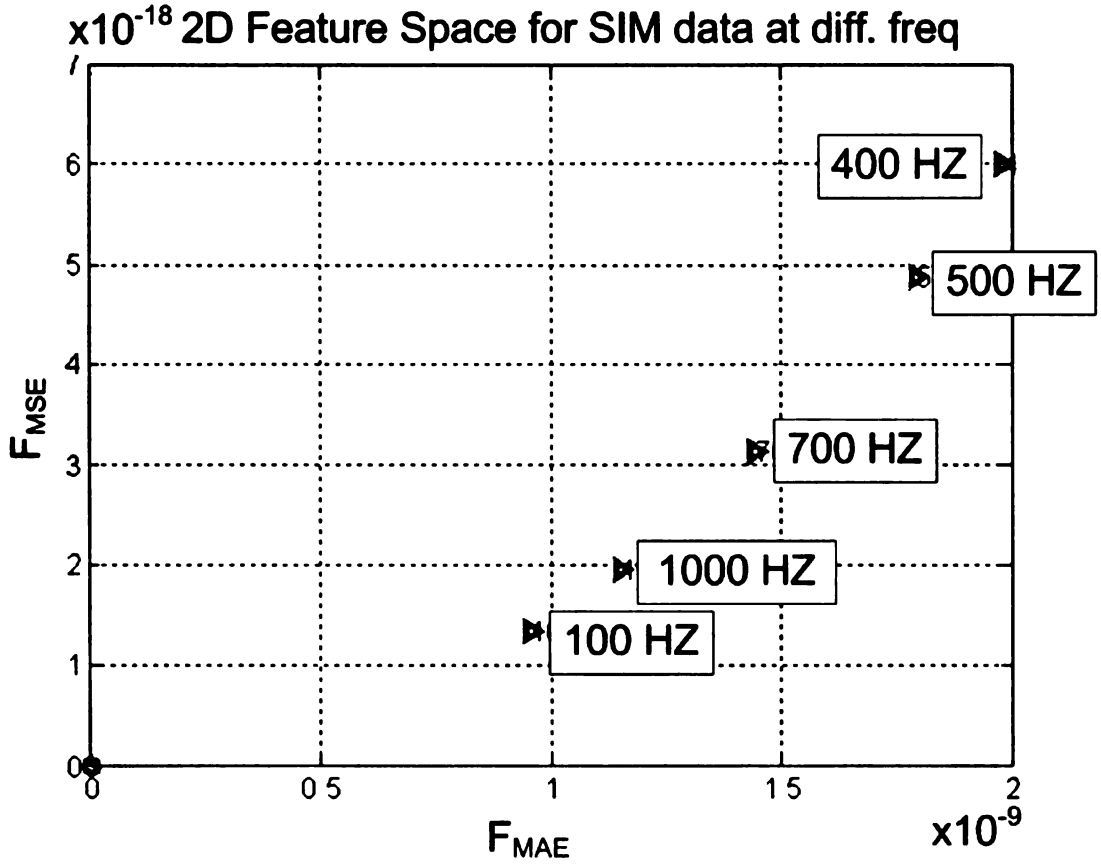


Figure 5.16 2D Feature Space for simulated data at different frequencies

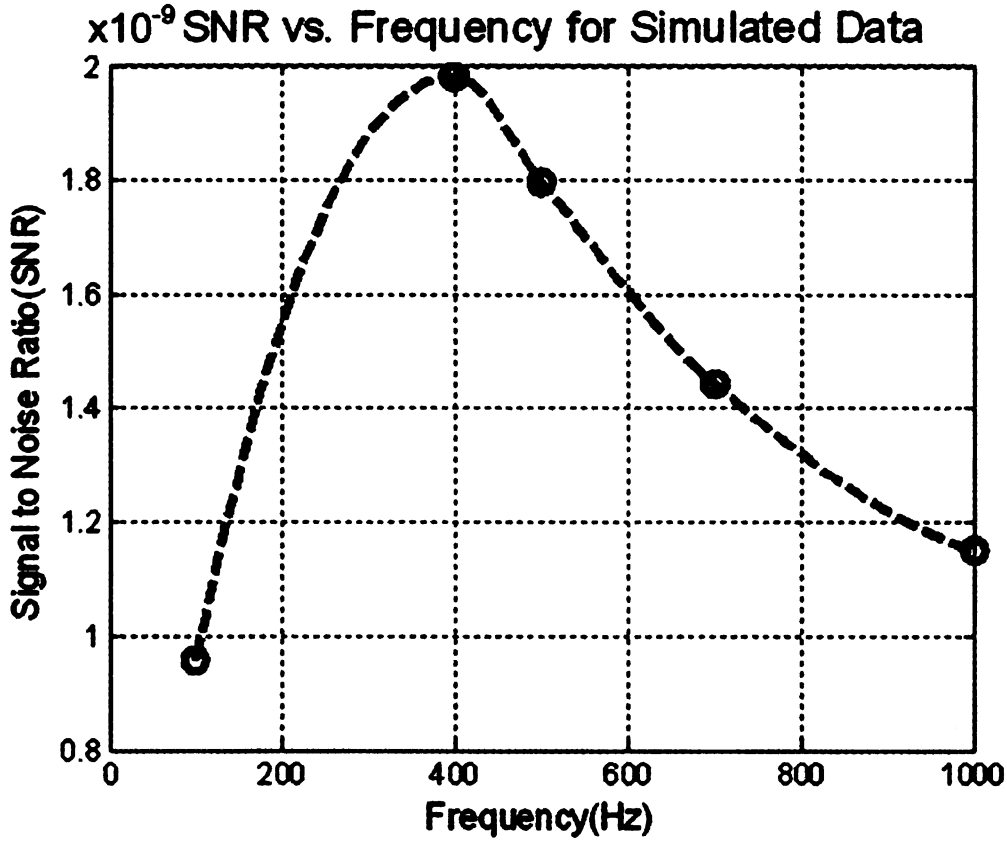


Figure 5. 17 SNR vs. Frequency for simulated signal for test sample with 0.3 inch subsurface crack

From Figure 5.17, the model predicted optimum frequency is 400 Hz, which is close to the optimum frequency of 450 Hz obtained from the experimental signals for test sample.

### 5.5.3 Magnitude Based Approach (MAG) data analysis for experimental data

A schematic of the test samples used in for collecting the GMR imaging data, are shown in Figure 5.18. The wing and stringer parts are Aluminum, which are fastened by flush head Steel (left two columns) or Titanium (right two columns) rivets. The sample has 11 outside Titanium rivets and 10 inside Ti rivets with

various subsurface crack sizes as shown: 0.20 inch, 0.22 inch, 0.25 inch and 0.30 inch. The Steel side has the same layout of rivets and cracks.

The in-phase and quadrature components for test sample obtained at 400Hz are shown in Figure 5.19. The segmented in-phase images at 400Hz for outside Titanium rivets are shown in Figure 5.20 for different crack sizes, from defect-free to the largest one, 0.30 inch subsurface crack. As we can see, it is difficult to differentiate cracks in the raw images.

A simple intuitive Magnitude Based (MAG) approach involves deriving the corresponding "zero-mean" signals (Figure 5.21) in which the progression of the cracks is observed from the shape of the right lobes.

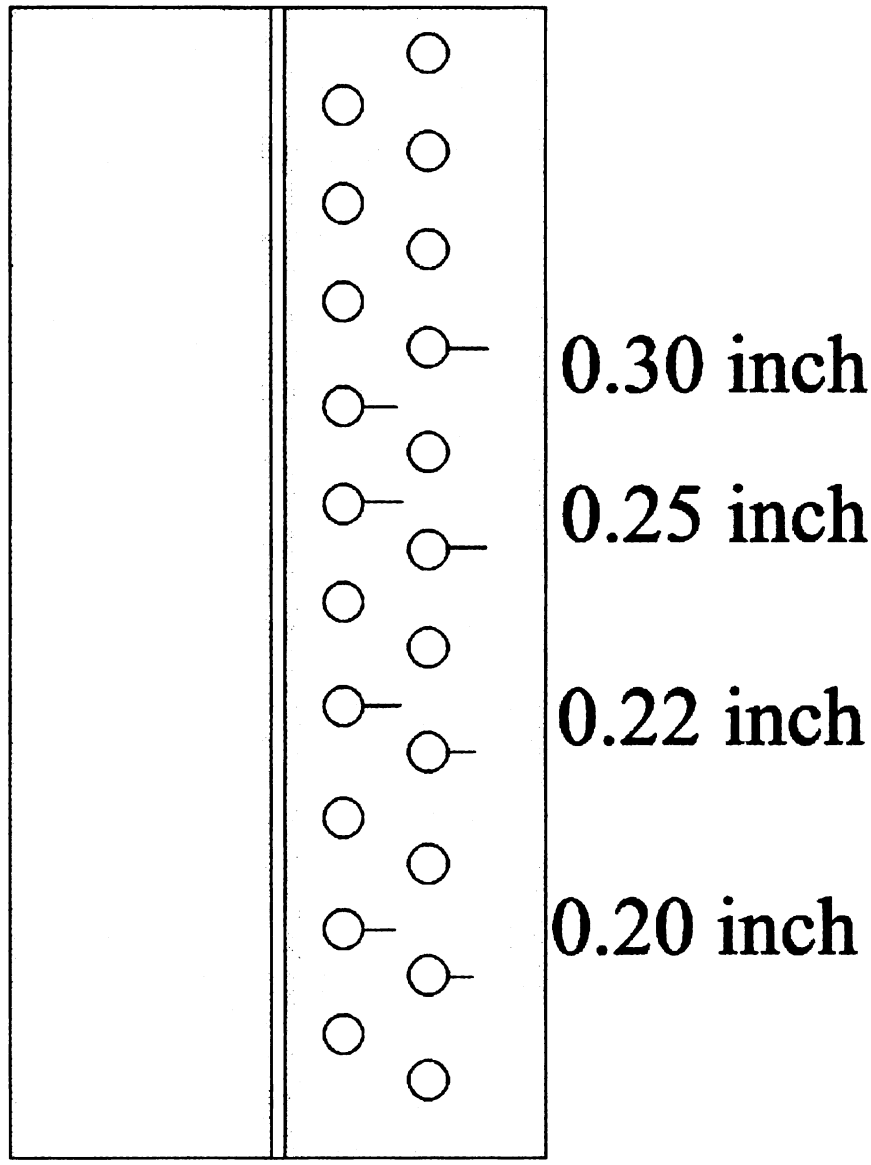


Figure 5.18 The test standard schematic

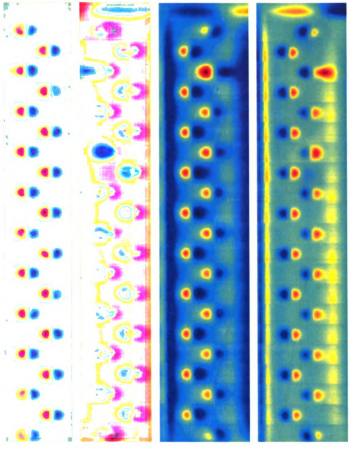

Figure 5.19 Raw GMR output images for the test standard at 400Hz: (from left to right) Steel in-phase, Steel quadrature, Titanium in-phase and Titanium quadrature components

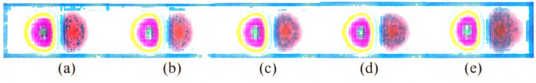


Figure 5.20 Raw output images for the test standard at 400Hz: (a) defect-free, (b) 0.20", (c) 0.22", (d) 0.25" and (e) 0.30" subsurface cracks

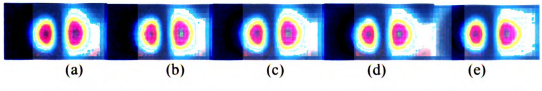


Figure 5.21 MAG images at 400Hz: (a) defect-free, (b) 0.20", (c) 0.22", (d) 0.25" and (e) 0.30" subsurface cracks

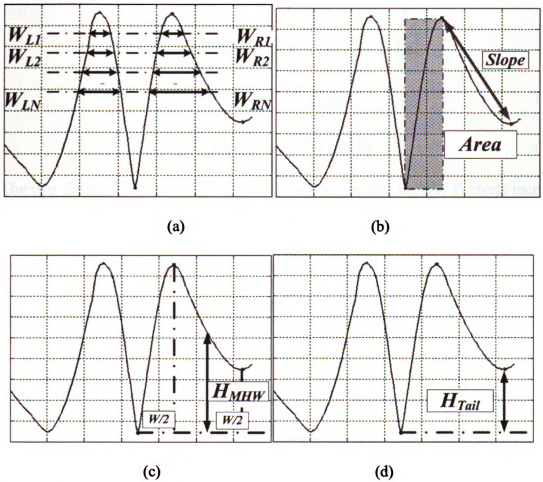


Figure 5.22 Definitions of features to quantify the MAG signals: (a) $F_1$ and $F_2$, (b) $F_3$, (c) $F_4$ and (d) $F_5$

Several features are extracted from the line plots across the center of the images in Figure 5.21. Equations 5.18 to 5.22 give the mathematical forms for those features, which are illustrated in Figure 5.22.

$$F_1 = \prod_{i=1}^{N} \frac{W_{Ri}}{W_{Li}} \tag{5.18}$$

$$F_2 = \sum_{i=1}^{N} (W_{Ri} - W_{Li}) \tag{5.19}$$

$$F_3 = \frac{Area}{|Slope|} = \frac{(X_3 - X_2)\cdot(Y_3 - Y_2)}{|Y_3 - Y_4|/|X_3 - X_4|} \tag{5.20}$$

$$F_4 = H_{MHW} \tag{5.21}$$

$$F_5 = H_{Tail} = Y_4 - Y_2 \tag{5.22}$$

The two dimensional scatter plots for classifying the test sample Ti rivets using the above features are shown in Figure 5.23. Although the MAG signals for outside and inside Ti rivets overlap, the features can separate the defective and defect-free data. However, this approach fails in the case of Steel rivets data due to the strong signal generated by the magnetic steel rivet.

Figure 5.23 MAG signals for the test standard Ti rivets and 2-D classification scatter plots

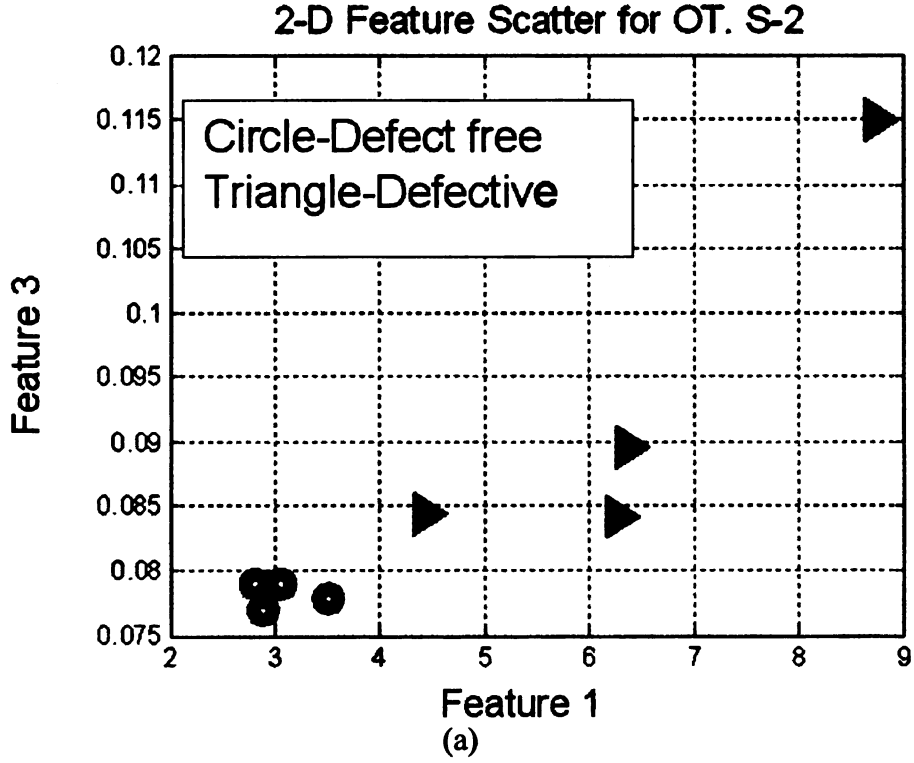

(a)

Figure 5.23 continued

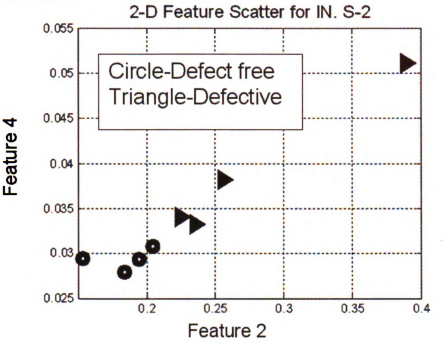


(b)

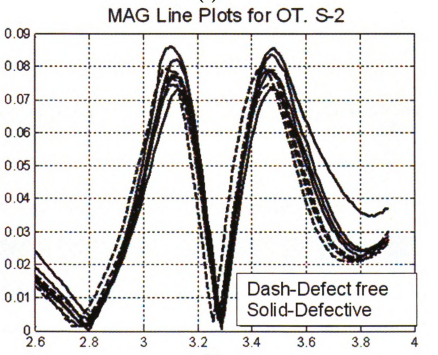


(c)

Figure 5.23 continued

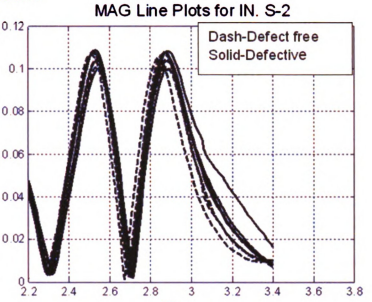


(d)

### 5.5.4 Optimum Detection Angle (ODA) Based Approach for experimental data

The detection angle based approach derives a weighted sum of the in-phase and quadrature components according to Equation 5.23.

$$< (S_I, S_Q), (\cos\theta, \sin\theta >= \left[\frac{A_o A_n}{2}\cos(\varphi_n)\right]\cos\theta + \left[\frac{A_o A_n}{2}\sin(\varphi_n)\right]\sin\theta \tag{5.23}$$

where $\theta$ is the DA. The operator <*,*> is the inner product.

(a) (b) (c) (d) (e)

Figure 5.24 GMR mixed images using ODA = 70 deg.: (a) defect-free, (b) 0.20", (c) 0.22", (d) 0.25" and (e) 0.30" subsurface cracks

The right hand of equation 5.23 is the "mixed" EC-GMR data. The optimum detection angle (ODA) $\alpha$ is calculated as:

$$\alpha = \arg\min_{\theta}(S_{pp}(\theta))$$

(5.24)

where $S_{pp}(\theta)$ is the peak to peak value in the mixed signal.

The mixed GMR images after applying the ODA $\alpha$ in Equation 5.23 are shown in Figure 5.24. Figure 5.25 showing the central line signals across the images shows significant separation between defective and defect-free rivet data. To quantify the difference between defect-free and defective mixed signals, two features, mean absolute error feature ($F_{MAE}$) and mean square error feature ($F_{MSE}$) are extracted as Equations 5.14 and 5.15 in the previous section. In Figure 5.26, the 2D scatter plots clear show better separation than that obtained using MAG approach.

Figure 5.25 Central line plots of images in Figure 5.24 (a) raw image-inside rivet (b) raw image-outside rivet, (c) mixed image-inside rivet (d) mixed image-outside rivet

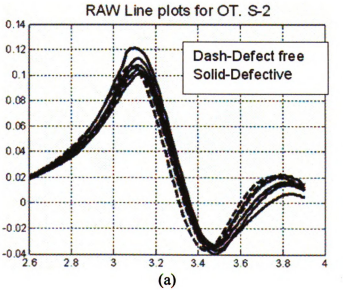

(a)

Figure 5.25 continued

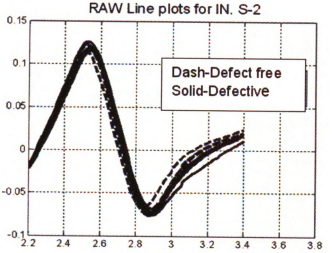


(b)

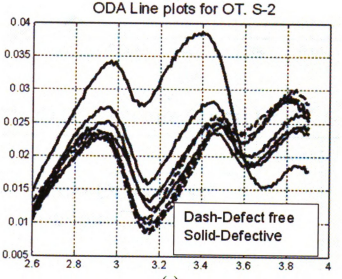


(c)

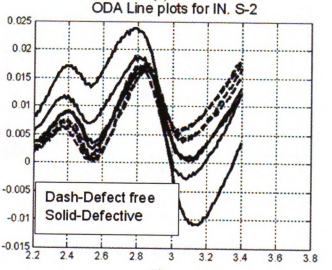


(d)

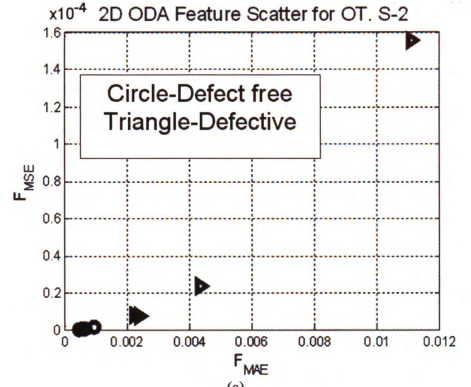


(a)

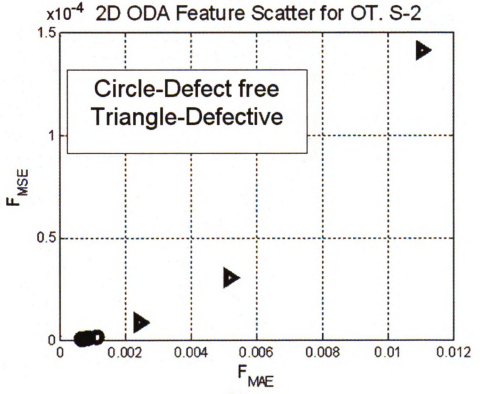


(b)

**Figure** 5.26 2D classification scatter plots for ODA approach: (a) OT and (b) IN

## 5.6 Discussion and Conclusion for Inversion of GMR imaging

The performance of MAG and ODA approaches is compared quantitatively using a signal to noise ratio $SNR_L$ metric defined as

$$SNR_L = \sqrt{\sum_{i=1}^{L} (F_i - m_{0i})^2 \Big/ \sigma_{0i}^{\,2}} \tag{5.25}$$

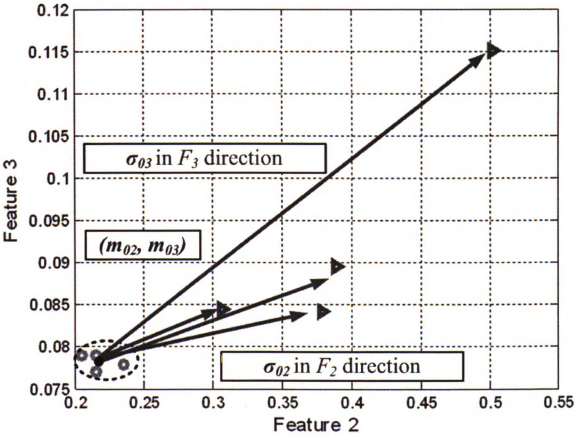


Figure 5.27 Illustration of $SNR_L$ definition

where $L$ is the dimensionality of signals, $m_0$ and $\sigma_0^{\,2}$ are the mean and variance of the defect-free data cluster as illustrated in Figure 5.27. The SNR

comparison between conventional ECT and GMR approaches is shown in Table 5.1. Dramatic improvement has been observed by applying the automated data analysis methods: MAG and ODA methods. This dissertation develops two innovative data analysis approaches for enhancing the GMR imaging data by increasing the SNR and hence maximizing the POD. Using these methods, GMR sensors show potential for detecting subsurface cracks in multi-layered structures. Automated crack detection is performed via optimum feature estimation and simple clustering.

Table 5.1 Signal to Noise Ratio Comparison between conventional ECT and GMR approaches

| TEST STANDARD | | SIGNAL TO NOISE RATIO (EQ. 5.25) | | | | |
|---|---|---|---|---|---|---|
| Thickness | Row | Methods | 0.30 inch | 0.25 inch | 0.22 inch | 0.20 inch |
| 0.16" | Outside | ECT | 3.00 | 1.50 | 1.50 | 1.50 |
| | | MAG | 45.0 | 18.0 | 14.0 | 9.60 |
| | | ODA | 317 | 49.8 | 16.4 | 17.1 |
| 0.16" | Inside | ECT | 2.50 | 1.50 | 1.00 | 1.00 |
| | | MAG | 20.6 | 8.20 | 4.40 | 4.00 |
| | | ODA | 292 | 64.5 | 17.1 | 18.2 |
| 0.25" | Outside | ECT | 2.00 | 1.00 | 1.00 | 1.00 |
| | | MAG | 30.1 | 11.4 | 7.70 | 5.50 |
| | | ODA | 114 | 13.3 | 4.60 | 11.4 |
| 0.25" | Inside | ECT | 2.00 | 1.50 | 1.00 | 1.00 |
| | | MAG | 7.20 | 4.60 | 2.50 | 3.30 |
| | | ODA | 44.1 | 9.70 | 4.10 | 5.10 |

# CHAPTER 6. POSITRON EMISSION TOMOGRAPHY IMAGING

## 6.1 Introduction

Positron Emission Tomography (PET) [1][3][7][8][15] imaging is a functional and metabolic imaging technique that generates images showing the functional details in patients by depicting the distributions of positron emitting radioisotopes. Neutron-deficient isotopes, e.g. $^{11}C$, $^{15}O$, $^{18}F$, $^{13}N$, that are incorporated into metabolically relevant compounds can decay by emitting positron, i.e. $\beta^+$ decay. Two 511keV photons are emitted in anti-parallel directions after the positron has been emitted from the $\beta^+$ decay and subsequently annihilated with an electron. If both of these annihilation photons are detected by the annihilation coincidence detection (ACD) of the PET system, the projection data is sorted in the Radon space, i.e. Sinogram, and reconstructed into a transverse slice of the image using filtered back-projection algorithm or the iterative methods [1][3][15]. Thus ACD sorts detected photons in the sinogram list-mode data, establishes the trajectories of the detected photons and finally forms the PET images. Modern PET scanners are multi-slice devices; permitting simultaneous 2D/3D acquisition of multiple slices over 15cm to 20cm of axial distance. PET imaging has proved to be effective and valuable

in clinical work and research particularly in cardiac and brain imaging, cancer detection and delineation and small animal studies [1][3][15].

The schematic diagram of a PET imaging with its physics is show in Figure 6.1. More details of the PET imaging system and a brief history of PET in medicine and positron-emitting tracers are discussed in the following sections.

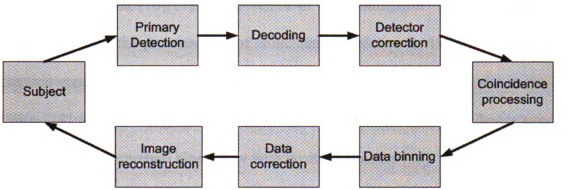


Figure 6.1 Schematic diagram of the PET imaging system with physics of PET

## 6.2 History of PET in Medicine

Positron emission from radioactive nuclei was discovered by Thibaud and Joliot in 1933 [10][11]. Subsequent research showed that after positron emission, two photons were emitted simultaneously at nearly opposite direction to each other [12]. The potential importance of positron-emitting radionuclides in medicine was suggested in 1946 [13]. The first use of positron in medicine is in the study in 1945 by Tobias et al. using $^{11}$C-CO in single photon mode [14] was to conduct an in-vivo studying of carbon monoxide.. The Massachusetts General Hospital (MGH) first in 1951

published an image of positron-emitting tracer study in man for localization of brain tumor [15]. The coincidence detection techniques were also employed at the same time.

In the late 1950s studies of metabolism in murine tumors with autoradiography, lung ventilation oxygen metalbolism in human were performed at the Hammersmith Hospital in London [16][17]. The inventor of the scintillation "Anger" camera, Hal Anger discussed the practicalities of coincidence detection in 1959 [18]. A circular "section scanner" was developed at Brookhaven National Laboratories also in the late 1950s [19] for localizing brain tumors, which appears to be the first device used to measure regional cerebral blood flow with positron emitters [20].

Due to the limitation of computational techniques, tomographic images and reconstruction algorithms were not developed until a decade later Kuhl et al. in Philadelphia explored transaxial SPECT in the 1960s and early 1970s [21][22]. Their approach was based primarily on reconstruction by back projection without pre-filtering compensation for the inherent blurring effect. Chesler adopted a filtered back projection approach to produce transaxial tomographic reconstructions in 1973 using data collected from the rotation MGH positron camera, presented convincing transaxial distributions of $^{13}$N-NH3 in the dog heart [23]. The development in Single Photon Emission Computed Tomography (SPECT): Anger cameras and scintillation probes helped in purchasing a PET scanner later. In 1974, a dedicated single-plane Positron Emissing Transaxial Tomography (PETT) was developed at the Mallinckrodt Institute of Radiology, St Louis The name of PETT was shortened to PET later.

Ter-Pogossian, Phelps, Hoffman, and Mullani had re-addressed the physical criteria that determined the accuracy of PET tomography [24][25] and optimized the physical design in order to minimize registration of scattered and random coincidences, and also to ensure adequate spatial sampling. In 1978, Phelps and Hoffman collaborated with Douglas and Williams and designed a commercial, single-plane PET scanner known as the Emission Computerized Axial Tomography (ECAT) [64]. In the late 1970s, PET made its biggest impact in realizing absolute quantifiable tomographic physiological data by minimizing the recording of scattered coincidences as well as random events. It is realized by using parallel delayed coincidence circuits [26]. In the early 1980s, a number of new radioactive tracers were introduced and most research was focused on 18F and 11C tracers. Till the year 1985, a number of different PET scanners had been developed including whole body scanners [15]. In the late 1980s, when block detector design was used, septa were placed between the transaxial planes in order to reduce the registration of scattered coincidences as well as the random ones. The dead time loss was also overcome by the shielding technique. Nevertheless, the counting statistics lost because of the small solid angle for coincidence detection and the sensitivity of 3D PET was restricted. The "open" mode PET was implemented by removing the septa and all possible coincidences were recorded. The basic sensitivity was increased by a factor of five while it brought new challenge for reconstructing the full volumetric 3D PET data. The value of 3D PET was evaluated using the criteria of Noise Equivalent Count (NEC) rate, as had been derived by Strother [63]. The use of 3D PET reduced the radiation dose required to achieve a significant statistical result. In 1990s, 3D PET/CT system was introduced and thought

to be a fundamental advance. As we see in the rich history of PET, a wide range of clinical research studies have been on going extensively but there still remains many challenges. Three different generations of PET scanners are shown in Figure 6.2 [80], in which the last one is the PET/CT fusion scanner developed by GE (Milwaukee, WI).

Figure 6.2 Three generations of PET scanner: the last is the PET/CT fusion system

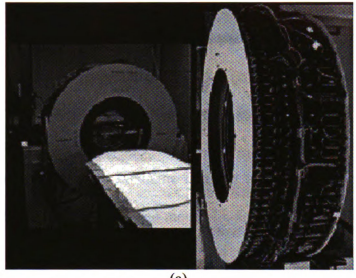

(a)


(b)

Figure 6.2 continued

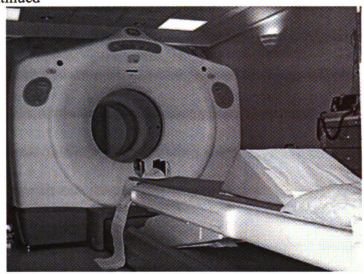

(c)

## 6.3 Physics and instrumentation of PET

PET and SPECT are both nuclear medicine imaging techniques. Similar to SPECT, PET is used to measure the functional and metabolic details of human body instead of anatomy. The main difference between PET and SPECT is that the injected or ingested radioisotopes used in PET emit positrons and generate two $\gamma$ rays in nearly opposite direction after positron-electron annihilation. Two photons are detected in PET instead of the single photon in SPECT. Consequently PET offers higher SNR and spatial resolution than SPECT.

The positron emitting radioisotopes must be synthesized using a cyclotron, and are structural analogs of a biologically active molecule, such as glucose, in which one or more of the atoms has been replaced by a radioactive atom [1]. Because of the short half-life of these nuclides, the cyclotron must be on-site to produce the radioisotopes, which is seen as one of the disadvantages of PET system. The most used radioisotope

is $^{18}$F-fluorodeoxyglucose (FDG) due to its relative long half-life, which is 109.7 minutes. Isotopes such as $^{11}$C, $^{15}$O, and $^{13}$N can also undergo radioactive decay by emitting positrons. Take $^{18}$F as an example, the radioactive decay is like Equation 2.1:

$$^{18}_{9}F \rightarrow ^{18}_{8}O + \beta^{+} + \nu \tag{6.1}$$

where $\beta^{+}$ is a positron and $\nu$ is a neutrino. The radioactive decay is illustrated in Figure 6.3.

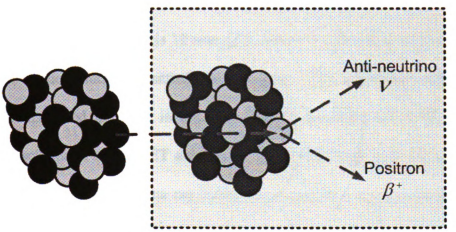


Figure 6.3 Illustration of radioactive decay in which the positron is generated

The positron travels a few millimeters in tissue randomly before it annihilates with an electron and results in the formation of two γ rays (or simply say photons) in nearly opposite direction with energy of 511keV each. The annihilation is expressed in Equation 6.2:

$$\beta^+ + e^- \rightarrow \gamma + \gamma$$

(6.2)

A PET system has a complete ring of scintillation crystals, usually Bismuth Germanate (BGO), surrounding the patients emitting 511kev photon pairs, which is illustrated in Figure 6.4. The dashed lines in Figure 6.4 represent the scintillation crystals detection ring with ACD, which forms the signal localization in the system. The green line is referred to as the line of response (LOR) along which the annihilation must have occurred. Ideally, two simultaneously emitting photons are detected at the crystals at the two ends of LOR within a certain time window (typical time window for BGO detectors is 12 nsec [3]), which is referred to as a coincidence event. Other issues, such as scatter, random noise, that introduce errors in this process, are discussed in detail in the next chapter on modeling of PET imaging system. The schematic of the PET detector structure with a detector element [80] is shown in Figure 6.5. The Gamma ray (Gamma photon) hits the scintillation crystal and is converted into optical photons, whose energy is proportional to the gamma ray energy. The photons are collected at the end of the crystal and passed into photomultiplier tubes (PMTs), where the light is converted to an electrical signal and amplified.

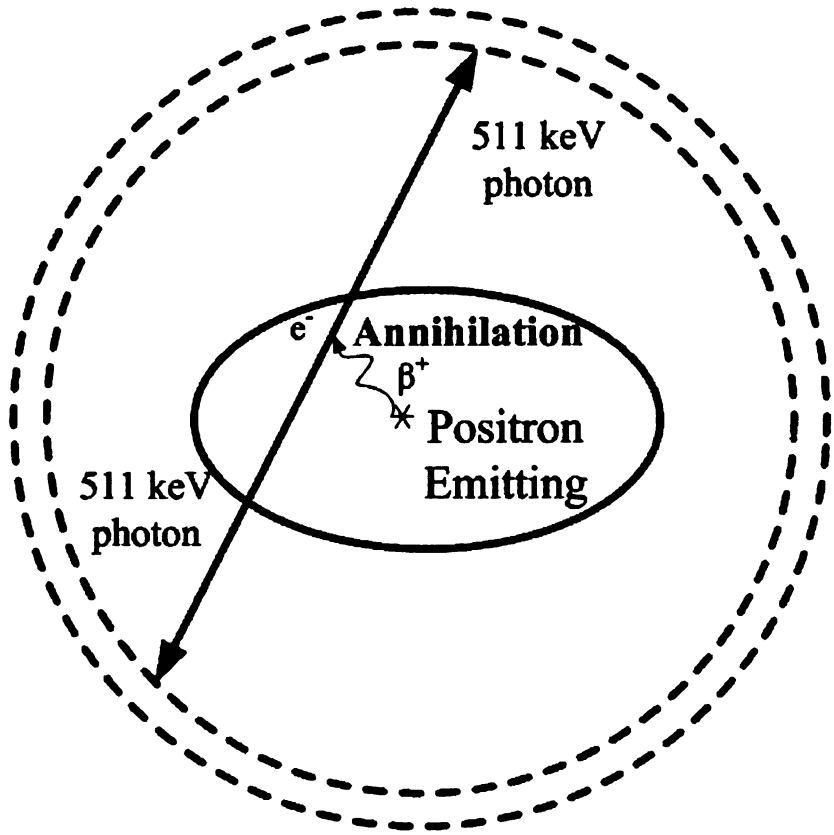


Figure 6.4 Illustrations of the overall photon emission and detection process of PET scanner

In contrast to SPECT, which requires collimation of single photon, PET gives much higher detection efficiency [1] than SPECT. Furthermore the energy of photons in PET is 511 keV, which is much higher than the 140 keV in conventional nuclear medicine. This in turn implies less attenuation in tissue and hence results in higher sensitivity of PET system. The resolution of a PET system depends on a number of factors and the typical values of the spatial resolution are 4.5 to 5mm [3].

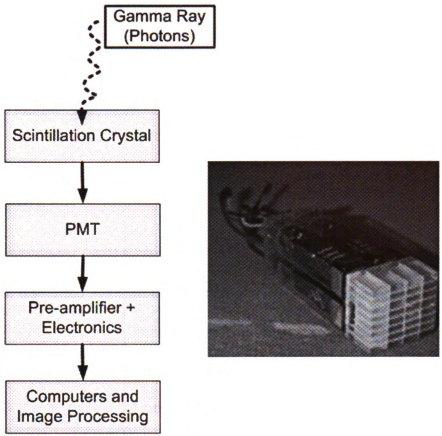


Figure 6.5 Schematic of the PET detector structure

To understand the physics of PET better, Table 6.1 [3] compares PET and SPECT systems in detail.

Table 6.1 Comparison between PET and SPECT

| | PET | SPECT |
|---|---|---|
| Principle of data collection | ACD | Collimation |
| Image reconstruction | Filtered back projection (FBP) or iterative methods | Filtered back projection (FBP) or iterative methods |
| Radionuclides | Positron emitters only | Any emitting x-rays, gamma rays, or annihilation photons |
| Spatial resolution | Relatively constant across transaxial image, best at center. Typically 4.5 to 5mm FWHM at center | Resolution in the radial direction is relatively uniform but the tangential resolution is degraded toward the center. Typically 10 mm FWHM at center for a 30 cm diameter orbit and Tc-99m. |
| Attenuation | More severe | Less severe |
| Cost | 1 Million to 2 Million | Typically 0.5 Million for double-head variable-angle |

## 6.4 Challenges in PET imaging

PET is widely used due to its uniqueness and is becoming more and more important in clinical and research work after its invention. However PET image acquisition takes a long period of time (usually greater than 10 minutes) for each scan while the patient is breathing. The respiratory motion that includes pulmonary and cardiac motion introduces severe artifacts in the final reconstructed PET images, as described further in the following sections. Hence for accurate interpretation of PET data, these artifacts have to be eliminated. Extensive motion correction techniques are investigated and can be found in the following literatures [82] [83] [84] [85][86] [87][89][91] [108][111]. We will discuss these issues in the next two Chapters.

# CHAPTER 7. FORWARD MODELS FOR POSITRON EMISSION TOMOGRAPHY IMAGING

## 7.1 Introduction

In this dissertation Monte Carlo (MC) methods are used for solving forward problem in PET imaging. MC simulation methods are finding increasing applications in nuclear medical imaging systems such as PET and SPECT [65] [66] [69]. The computational PET model developed in this dissertation is based on MC methods. The name "Monte Carlo" was coined by Von Neumann [66] and chosen during the WWII Manhattan Project [70] because of the similarity to "random" properties of casino games based on chance. They have been applied to simulate a process with random behavior and in which the physical parameters are hard and even impossible to measure and quantify. The availability of an accurate computational model using MC technique helps immensely in understanding the undesirable effects of several operational parameters such as blurring effects of patient movement due to respiratory or other physiological motions in PET.

In a statistical sense, the Monte Carlo method can be explained simply as an evaluation method for an integral:

$$I[f(x)] = \frac{1}{b-a}\int_a^b f(x)dx \tag{7.1}$$

Uniform random variables $X_1$, $X_2$,..., $X_N$ are generated in the interval (a, b) and substituted into:

$$\hat{I}[f(x)] = \frac{1}{N}\sum_{i=1}^{N} f(X_i) \tag{7.2}$$

Based on the Law of Large numbers (LLN), we get:

$$\hat{I}[f(x)] \approx E[f(x)] = \int_a^b f(x) \cdot \frac{1}{b-a} dx = I[f(x)] \tag{7.3}$$

In medical physics applications, the systematic development of MC methods did not start until 1948 by Kahn and Harris [71]. Fermi, Metropolis and Ulam used MC to estimate the eigenvalues of the Schrodinger equation during the same year. The applications of MC in this field increased after the review paper by Raeside [72] and several books [70] [73] [74]. The methods were applied to all aspects of nuclear medicine imaging, including Planner Gamma Camera (PGC) imaging, SPECT, PET, and multiple emission tomography (MET) [66]. However, MC methods did not find widespread use until high performance computers became more common in recent years.

In the PET system described in this dissertation, due to the complex detector geometries, inhomogeneous attenuation within the body or phantom structures and stochastic nature of nuclear medicine systems, analytical solutions are seldom possible and an accurate, fast, and efficient numerical model is necessary. This chapter first presents a 2D MC model, which simulates the radiation emission,

transport, and detection process of PET systems to generate data in the sinogram space. The reconstructed images are then obtained using filtered back projection (FBP) method [1] [75] to validate the model. A 3D MC model using the SimSET [68] is then introduced.

## 7.2 Monte Carlo Methods in PET

Monte Carlo (MC) methods are statistical methods that use random numbers to simulate any specified situation and physical process. The major components of MC method include

1. The probability density functions (pdf's) of the physical system, which is PET system;
2. Random number generators;
3. Sampling rules for the specific system pdf's;
4. Tallying or scoring methods to accumulate the outcomes and
5. Error estimation as a function of the number of trials and other quantities.

Details of the general principles of MC method are well established and described in several publications [70][72][73][74]. The following sections present a discussion of the general principles.

### 7.2.1 System Model

In a PET scanner system, the relationship between the measurement $\lambda_j$ and the object $f(\bar{x})$ can be described by a linear model that represents the summation or

integration of spatially varying detector sensitivity function $s(\bar{x})$ [76] representing the object. The sensitivity function is different for scatter-free or with scatter and random noise situations. The detector measurement can be represented mathematically as follows:

$$\sum_{j=1}^{N} \lambda_j = \int_{FOV} f(\bar{x}) \cdot s(\bar{x}) d\bar{x} \tag{7.4}$$

Where $\bar{x}$ is $R^m$, $m$ = 2 or 3 for m dimensional object function, FOV is the field of view. In PET image reconstruction, a number of approaches have been presented [77] to estimate the object $f(\bar{x})$ by assuming that a discrete number of PET scanning measurements are obtained accurately. In this Chapter, we present a forward probabilistic model that uses a known sensitivity function $s(\bar{x})$ to predict the simulated measurements which are then used as input for image reconstruction.

### 7.2.2 Random Number Generator

The random number generator (RNG) is an important and fundamental part of MC simulation models, in which the RNG is used to control decision making for physical events having a number of possibilities. Generally, the sequence of random numbers used in the MC model should have the following properties: uncorrelated, long period, uniformity, reproducibility and speed [66].

The sequences of random numbers are uncorrelated and independent. Actually all RNGs based upon mathematical algorithms are "pseudo-random" and are repeatable.

However the period of the RNG is long enough and has the appearance of randomness. The repetition only occurs after a very large set of random numbers are generated. Also the sequence should be uniform and unbiased. The reproducibility is important because we need to repeat the simulation when debugging the programs or transfer the programs to a different machine. Speed is of course a concern to make the whole simulation efficient and fast.

A large number of RNGs are available for implementation [78]. The most commonly used RNGs include Linear Congruential Random Number Generator (LCRNG), which is also tested in the dissertation, and Lagged-Fibonacci Random Number Generator (LFRNG). The LRRNG and LCRNG formulations are presented in Equation 7.5 and 7.6.

$$RN_{n+1} = (RN_{n-l-1} \otimes RN_{n-k-1}) \bmod(c), l > k \tag{7.5}$$

where the operation $\otimes$ may be one of the binary arithmetic operators, l and k are the lags and c is a power of 2.

$$RN_{n+1} = \frac{(a \cdot RN_n + b) \bmod(c)}{c} \tag{7.6}$$

where $a$ is the multiplier, $b$ is the additive constant or addend and $c$ is the modulus. The initial random number $RN_0$ is the seed. If $b$ is zero then the LCRNG is called a multiplicative congruential random number generator (MCRNG). The pseudo-code of MATLAB implementation for LCRNG is as follow:

```
IF n = 0
    RN(n+1) = SEED (real number from [0, 1])
ELSE
    RN(n+1) = LCRNG_iter(RN(n));
END
Function RN_n+1 = LCRNG_iter(RN_n)
    A = 7000; B = 55000; C = 260000;
    RN_n+1_temp = mod(floor(RN_n)*A+B, C);
    RN_n+1 = RN_n+1_temp./C
End
```

In the 2D model, a uniform RNG is used in deciding the rotation angle of LOR $\theta$ and photon path length d before scatter is used. The uniform RNG outputs are also used in deciding the annihilation position while sampling the cumulative distribution function (cdf) calculated based on the input 2D phantom intensity. The uniform RNG in MATLAB was also tested in the current model with good results.

### 7.2.3 Sampling Techniques

In MC simulation, the pdf's of the PET system needs to be randomly sampled so that the physical events can be described and evolution of the overall system can be simulated. The illustration of the basic idea of sampling is shown in Figure 7.1.

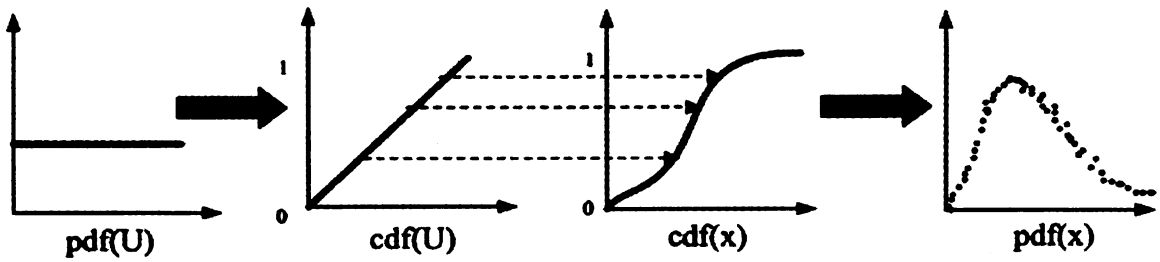


Figure 7.1 Illustration of sampling the cumulative distribution function (cdf) for simulating the annihilation event

The sampling methods include direct method, rejection method and mixed method which combines the two above methods [70]. In this dissertation, the simplest direct method is used since the inverse of the cumulative distribution function (cdf) for determining the annihilation position is easily obtainable using the true image intensity distribution. This cdf is then uniformly sampled to provide the pdf of the region where the annihilation occurs (discretized pixel index in this 2D model). The corresponding cdf for determining the annihilation position is calculated according to the 2D phantom intensity and distribution. This is reasonable because the more the radioactive uptake concentrated in the distribution; the higher the annihilation density. The cdf of the photon pair emitting angle is simply a straight line because the probability of emitting direction is distributed uniformly in $[0^\circ, 360^\circ]$.

## 7.3 Two dimensional (2D) model

In all the simulations described in Chapter 7, we assume that the patient is at rest, i.e. by holding breath and the simulated projection data will be consistent with the output

obtained using Equation (7.13). The simulated projection data are called "motion-free" sinogram. The "motion-encoded" sinogram [82] is generated to simulate the patient data with thoracic motion and these details are discussed in the following Chapter.

In the probabilistic model for motion-free case, the object $f(\bar{x})$ is a 2D phantom, which is defined as a nonnegative intensity function $\rho(R,\theta)$ and discretized in a bounded region $\Omega$. For the purpose of simplicity of mathematical calculations, all functions and equations are derived in the Radon space (RS) $\Re(R,\theta)$ coordinates. The 2D phantom $\rho(R,\theta)$ is treated as a known system input with intensity $\rho_i$, $i$ = 1, 2, ..., $M$ at each pixel, where $M$ is the total number of pixels in the bounded region $\Omega$. Any detector pair $D_j, j$ =1, 2, ..., $M$ is defined in the RS coordinates as a vector $(\bar{d}_{j1},\bar{d}_{j2})$, where $\bar{d}_{j1}=(-R_j,\theta_j)$ and $\bar{d}_{j2}=(R_j,\theta_j+\pi)$. The geometry and the new RS coordinate introduced in this dissertation with the discretized region and the detector pairs are illustrated in Figure 2(a). There are three different cases considered in the probabilistic model, namely, i) scatter-free, ii) single scattering and iii) random noise. Generally, in all three situations the relationship between the measurement $\lambda_j$ of jth detector pair and the 2D intensity function $\rho(R,\theta)$ is defined as

$$\sum_j \lambda_j = \iint_{\Omega} \rho(R_i,\theta_i) p_{ij} dR d\theta \tag{7.7}$$

where $p_{ij}$, the specific form of the detector sensitivity function $s(\bar{x})$ in our model, is the probability of a 511keV photon pair generated by annihilation at the ith pixel and detected by the $j$th detector pair. The value of $p_{ij}$ is calculated as the exponential of a line integral of the attenuation coefficient of each pixel along the photon emission path as follows:

$$p_{ij} = \frac{1}{\pi r^2} \exp\left(-\int_{\bar{d}_{j1}}^{\bar{d}_{j2}} \mu(R_i, \theta_i) dl\right) \tag{7.8}$$

where the attenuation coefficients $\mu$ is also predefined in the bounded region $\Omega$, shown in Figure 7.2(a) and r is the radius of the PET scanner. However, the sensitivity function in Equation 7.8 for different scenarios is calculated differently according to the apparent lines of response (LORs) for different situations. By applying MC technique, the integral in the Equation 7.7 is evaluated by generating a large number of trials and then evaluating the summation. The sinogram data is generated by $\lambda_j$ and then used to reconstruct the phantom using the FBP method. The illustrations of scatter-free, single scatter and random noise models are shown in Figure 7.2(b) to 7.2(d). In the single scattering case, the photon path length d before the scattering is calculated using MC technique according to Equation 7.9, where U is a uniform random number in (0, 1).

$$d = -\frac{1}{\mu}\ln(1-U) = -\frac{1}{\mu}\ln U \tag{7.9}$$

The scattering angle $\theta_s$ and the photon energy after scattering $E_s$ are calculated based on Klein-Nishina cross-section equation and the sampling algorithm originally developed by Kahn [71]. $E_{in}$ and $E_s$, the energy before and after the scattering and the photon path $l_s$ after the scattering are calculated through Equations 7.10 to 7.12.

$$E_{in} = 511e^{-\bar{\mu}d} keV \tag{7.10}$$

$$E_s = 511keV/(2-\cos\theta_s) \tag{7.11}$$

$$l_s = \sqrt{d^2\cos^2\theta_s - d^2 + R^2} - d\cos\theta_s \tag{7.12}$$

Figure 7.2 (a) 2D MC Model Geometry, (b) scatter-free (c) single scatter and (d) random noise

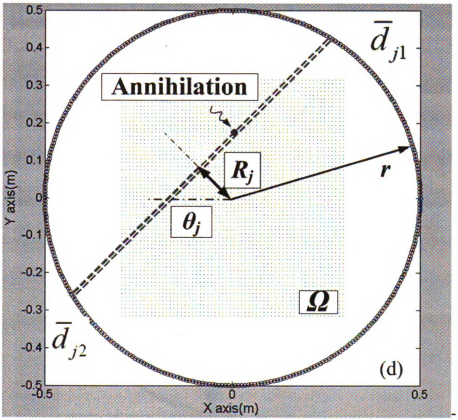


(a)

Figure 7.2 continued

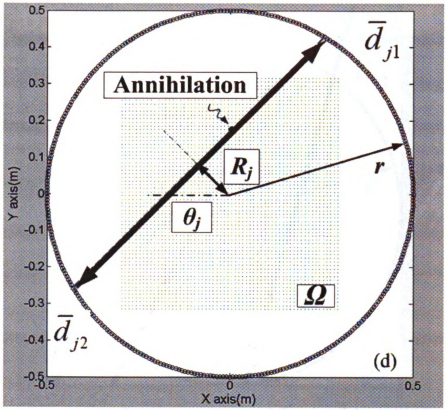


(b)

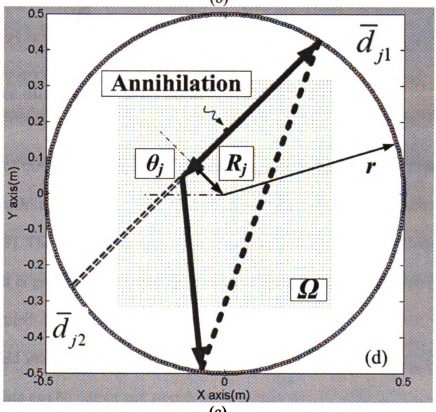


(c)

Figure 7.2 continued

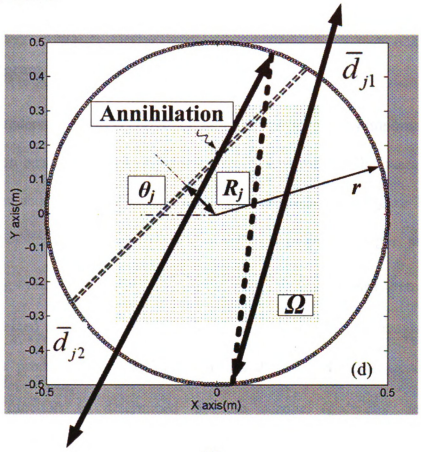


(d)

## 7.4 Three dimensional (3D) model

A number of three dimensional MC models can perform accurate simulations of PET systems, such as SimSET [68], Geant4 Application for Tomographic Emission (GATE) [79]. The emission images were integrated into the simulation similar the 2D case, which is generated by applying the motion models. The attenuation images are also generated by assigning the appropriate attenuation coefficients in the 3D phantom and incorporated in to the model. Finally the projection data, sinogram or list mode data can be output and stored. More details are provided in Chapter 8.

## 7.5 System Data Acquisition

### 7.5.1 Sinogram

In order to understand motion correction in projection space, it is important to discuss the projection or sinogram data representation. A schematic of the overall procedure for projection acquisition and sorting in sinogram are depicted in Figure 7.3, in which two groups of lines of response (LORs) at different projection angles are shown. A PET imaging system is described by a linear model so that the measurement $\lambda_i$, the photons detected at the *j*th detector pair, is represented by the integral along the LOR of the product $f(\bar{x})$ (radioactivity ) and $s(\bar{x})$ (detector sensitivity). The sensitivity function is determined by the scanner geometry and detector characteristics. Mathematically, the detector measurement also called the ray sum is represented simply in Equation 7.4.

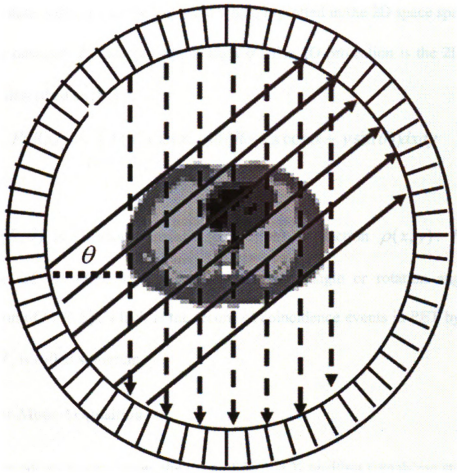


Figure 7.3 Projection data acquisition and sorting in sinogram: dashed lines and solid lines represent the projections at an angle of -90 deg. and an arbitrary angle, where the angle is between -90 deg. and 90 deg.. Each projection reprents one complete view of the object at one particular angle by lines of response (LORs)

The collection of $\lambda_i$ with the same angle $\theta$ is the projection $P(R_i,\theta)$, where $R_i$ is the trans-axial distance between each ray and the system geometric center. Each point of the object $f(\bar{x})$ is included in only one ray of each projection, and the sum over all rays for all the projections, $\sum_{j=1}^{N}\lambda_j$ is proportional to the total radioactivity distribution of the 2D slice of the object. This entire collection of

projection data is defined as the sinogram which is plotted in the 2D space spanned by trans-axial distance $R_i$ and projection angle $\theta$. The 2D projection is the 2D Radon transform described as [81]:

$$P(R,\theta) = \int_{FOV} f(x,y)s(x,y)\delta(R-(x\cos\theta + y\sin\theta))dxdy \tag{7.13}$$

where $P(R,\theta)$ is a Radon transform (projection) of function $\rho(x,y)$. $R$ is the coordinates of the LOR (ray) and $\theta$ is the view angle or rotation angle. The organization of $P(R,\theta)$, which is the record of coincidence events in PET by storing $R$ and $\theta$, is called sinogram.

### 7.5.2 List-Mode Acquisition

In the list-mode data acquisition, the pairs of *X*- and *Y*- position signals are stored in a list, which is time dependent. The position signals can be obtained using position circuits of the scintillation detectors from pulses in photomultiplier tubes (PMTs). Gated signal indicators can also be included in the list-mode data. For example, if the ECG signal is monitored in the gated cardiac PET imaging, the "trigger" signals are also stored in the list. The acquisition of a gated cardiac image sequences is illustrated in Figure 7.4. It should be noted, that gated acquisition is one of the three types of frame-mode acquisition in nuclear medicine [3].

After the acquisition, the list mode can be reconstructed to obtain PET images for display, or converted into projection data (sinogram). The illustration of list-mode acquisition is shown in Figure 7.4 with the gated timing signals also being stored.

The advantage of list-mode acquisition is that it is flexible for data manipulation and image formation. The disadvantage is that it requires more disk storage space.

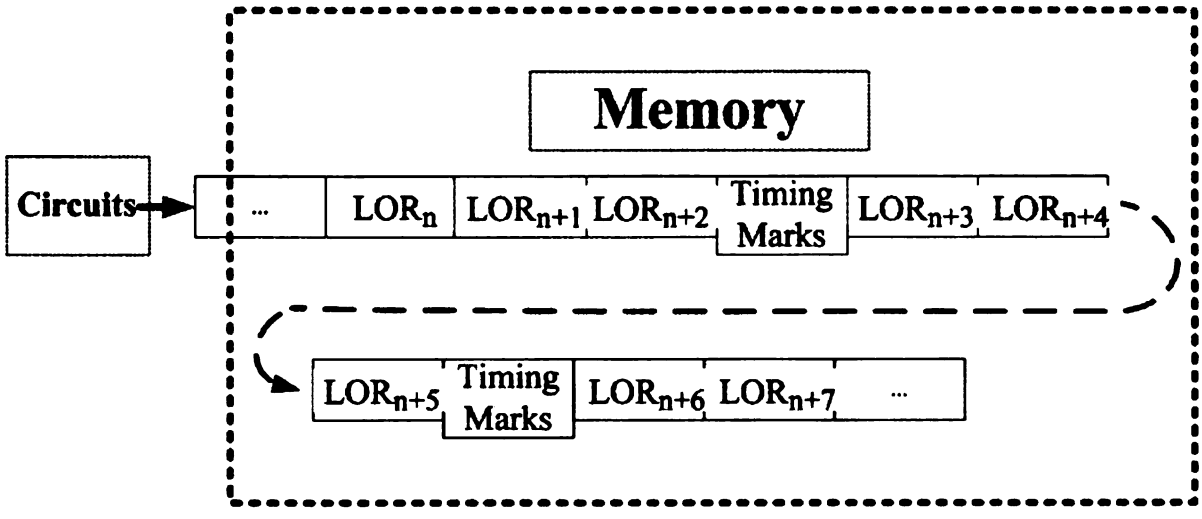


Figure 7.4 Illustration of list-mode acquisition

## 7.6 PET Image Performance and Quality

There are several factors affecting the PET image quality besides the patient motion and breathing noise. Figure 7.5 illustrates three different coincidences in PET imaging, which is also modeled in the 2-D geometry presented in this Chapter. Scatter and random noise reduces the image contrast to noise ratio (CNR) as we can see in the simulation results, are therefore one of main sources of PET imaging noise.

Figure 7.5 (a) True, (b) scatter and (c) random coincidences affecting the PET Image Quality

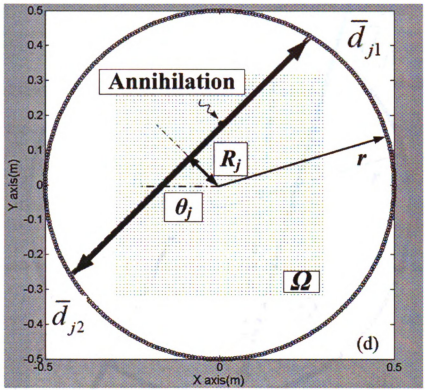


(a)

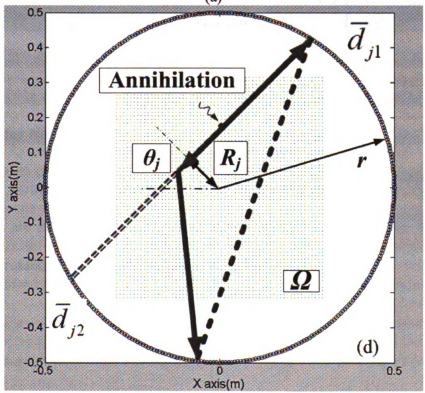


(b)

Figure 7.5 continued

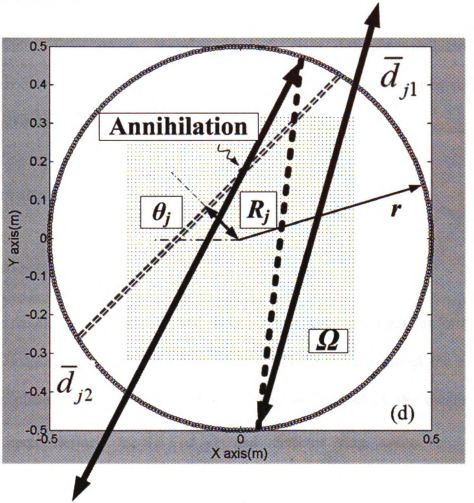


(c)

### 7.6.1 Scatter Noise

The scatter coincidence means one or both of the emitting photons from a single annihilation are detected by ACD, which gives "misplaced" LOR. The scatter noise can be suppressed with energy resolution and collimation.

### 7.6.2 Random Noise

The random noise means emission photons from different annihilations are simultaneously detected by ACD, which gives the "false" LOR. It can be suppressed with small coincidence time and collimation.

## 7.7 Results and Discussion

### 7.7.1 2D results

We have developed a reliable 2D MC model in MATLAB environment for the study of PET imaging with different noise levels [155]. In the 2D model the simulated object is placed in a discretized region $\Omega$ and surrounded by the detectors with detector pair defined as $(\overline{d}_{j1}, \overline{d}_{j2})$ and detector ring radius $r$, detailed configuration is shown in Figure 7.6.

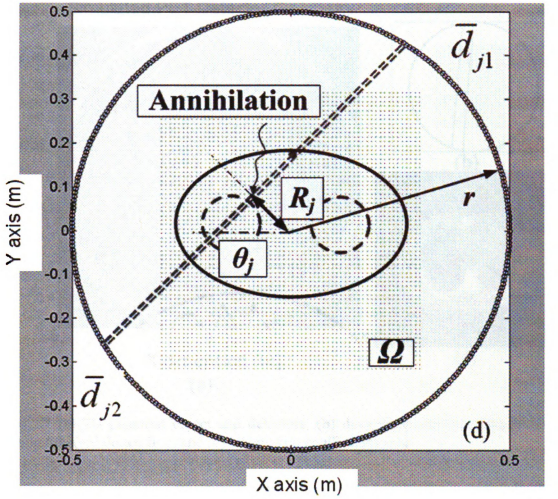


Figure 7.6 2D Monte Carlo Model for patient motion study with discretization grids illustrated

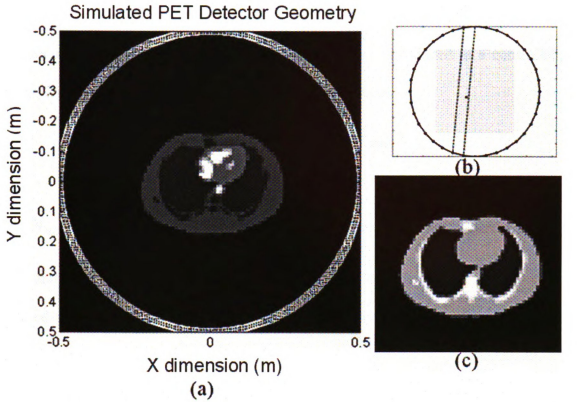


Figure 7.7 (a) 2D phantom object and detectors, (b) discretized solution domain with detection tube(red dotted line) and (c) attenuation coefficients map


Figure 7.8 Simulation results with one million trials: (a) true image (b) simulated sonogram and (c) reconstructed image

The 2D phantom and the detectors are shown in Figure 7.7(a). The discretized region $\Omega$ has the dimension $600mm \times 640mm$ and the radius of the PET scanner is 0.5m, as illustrated in Figure 7.7(b). The simulated sinogram and the reconstruction result

are shown in Figure 7.8(b) and Figure 7.8(c) respectively. Two types of noise, namely, 1) scatter noise and 2) random measurement noise were introduced in a controlled manner. The noise level was defined by the parameter $\alpha$ as:

$$\alpha = N_{noise}/(N_{noise} + N_{true}) \tag{7.14}$$

where $N_{noise}$ is the number of noise (scatter or measurement noise) events and $N_{true}$ is the number of true annihilation events. The values of $\alpha$ = 0, 0.2, 0.4 and 0.6 were simulated and the results are shown in Figure 7.9(a) showing effect of noise due to single scatter. Figure 7.10(a) shows the effect of measurement noise. A comparison of the line plots in Figures 7.9(b) and 7.10(b) show the general similarity of true and simulated signals. The difference for $\alpha$ = 0 case is due to the small number of simulations used in this feasibility study.

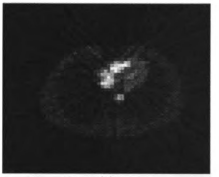

(a)

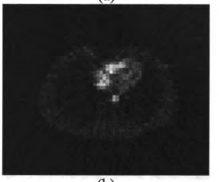

(b)

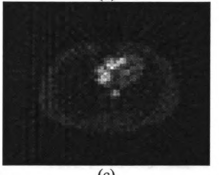

(c)

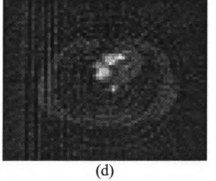

(d)

Figure 7.9 Reconstructed images at different scatter noise level from (a) to (d): reconstructed images at alpha = 0, 0.2, 0.4 and 0.6

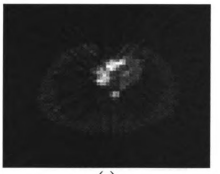

(a)

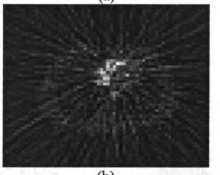

(b)

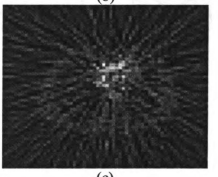

(c)

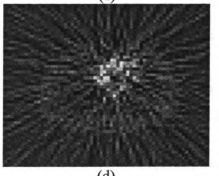

(d)

Figure 7.10 Reconstructed images at different random noise level from (a) to (d): reconstructed images at alpha = 0, 0.2, 0.4 and 0.6

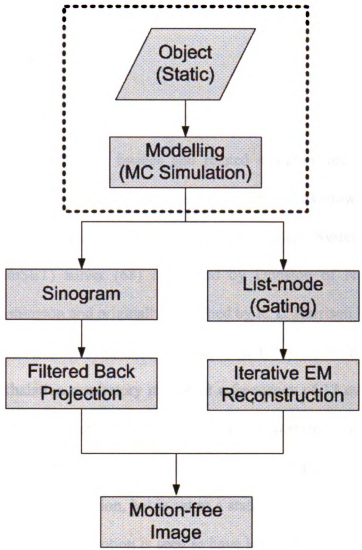


Figure 7.11 Motion-free PET images modeling and image reconstructions procedure

The basic idea of PET modeling without motion is illustrated in Figure 7.11. The "static" object is passed into the models and generated the projection data, either sinogram or list-mode data. After applying the proper reconstruction schemes, the motion-free images are obtained. This approach is presented and validated in this Chapter, which is very important before introducing any motion into this frame. An

updated schematic will be presented in Chapter 8, which incorporates the motion detection and correction algorithms.

### 7.7.2 3D Results

Although only 2D sliced PET images and related sinogram are analyzed in this dissertation, a more realistic 3D human torso is constructed as shown in Figure 7.12. This scenario has been modeled using the Simulation System for Emission Tomography (SimSET) solver [68] developed by Division of Nuclear Medicine University of Washington and originally published by R. L. Harrison [156].

For the 3D human torso model, the lungs are modeled as cylindrical objects with inhalation and exhalation respiratory motion at a frequency of 12 cycles per minute; the heart is modeled as spherical object with diastole and systole cardiac motion at a frequency of 60 cycles per minute. The elliptical chest wall shape is also changing in phase with the respiratory motion, but is set to a static cylindrical object here for the sake of simplicity. Also this motion is seen to have little effect on the final sinogram data of internal organs. The spine is also simulated using a static cylindrical shape without motion.

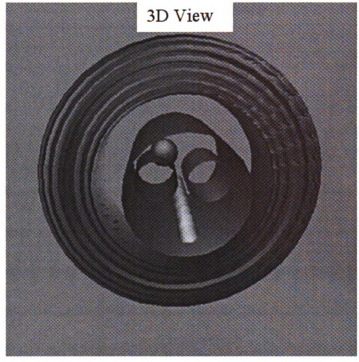


Figure 7. 12 3D view of the human torso model in the motion model, the chest wall, lungs, heart and spine are simulated with 3D objects with varying shape at various frequencies

## 7.8 Motion Models

The pulmonary and cardiac motion are intrinsically non-rigid deformable and difficult to be characterized using simple models. In the previous study for CT respiratory motion, the non-linear synthetic motion functions were applied [142]. Because PET images have less anatomical details than CT images, we apply a linear motion function for approximating the changing anatomical shapes of internal organs, i.e. lungs and heart. The motion patterns for the lungs are modeled linearly and a quasi-linear function is used to model the motion of heart as illustrated in Figure 7.13.

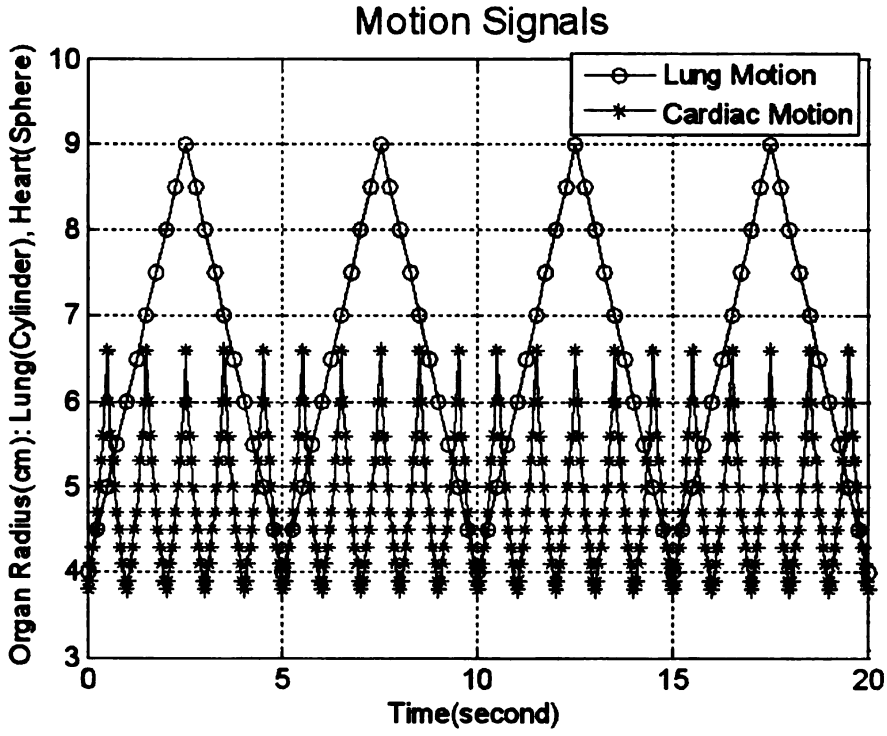


Figure 7. 13 Motion signals for both pulmonary (circle & solid line) and cardiac (star & solid line) motion

We generate twenty-one phases for each cycle of pulmonary and cardiac motion. In the motion model, the lung radius $R_l$ varies from 4cm (minima of the circle & solid line) to 9cm (maxima of the circle & solid line) with a spatial step size of 0.5cm and the temporal step size of 0.25s. The heart outer wall radius $R_c$ varies from 3.6cm to 6.6cm with uneven spatial step size and 0.05s temporal step size (the star & solid line in Figure 7.13). The cross section of the 3D human torso model is depicted in Figure 7.14, in which the chest wall size $R_{tx}$ and $R_{ty}$ remain the same throughout the motion cycles.

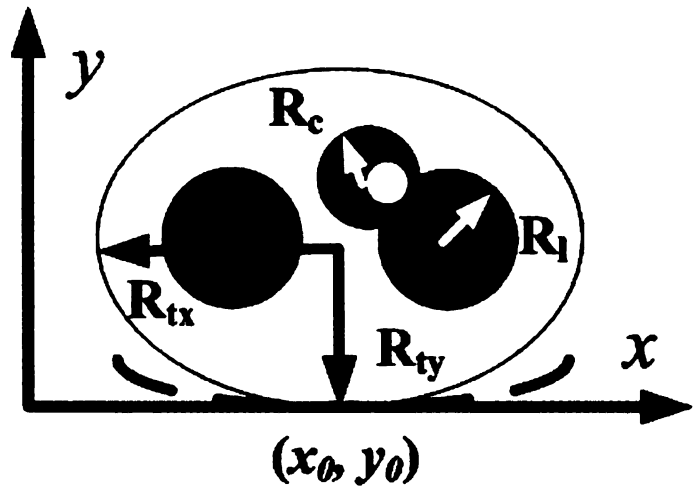


Figure 7. 14 Cross section of the 3D human torso modeled as cylindrical and elliptical objects with different sizes

In contrast to the simple x- and y- direction scaling method, a 2D algorithm incorporating elastic deformation factors is introduced in this dissertation. The cardiac motion, lung motion and chest motion are treated independently with different contraction frequencies. $R_c$, $R_l$, $(R_{tx}, R_{ty})$ are the periodic radius of heart, lung and human torso respectively and defined in equation (7.15) to (7.17):

$$R_c = \frac{R_{cMAX} - R_{cMIN}}{2}\sin(2\pi f_c t + \phi_c) + \frac{R_{cMAX} + R_{cMIN}}{2} \tag{7.15}$$

$$R_l = \frac{R_{lMAX} - R_{lMIN}}{2}\sin(2\pi f_l t + \phi_l) + \frac{R_{lMAX} + R_{lMIN}}{2} \tag{7.16}$$

$$R_t = \frac{R_{tMAX} - R_{tMIN}}{2}\sin(2\pi f_t t + \phi_t) + \frac{R_{tMAX} + R_{tMIN}}{2} \tag{7.17}$$

where $R_{MAX}$ and $R_{MIN}$ are the maximum and minimum radius for the organs and torso size. $f_c, f_l, f_t$ are the frequencies for the cardiac motion, lung motion and chest motion, in which the cardiac motion frequency is about 60 beats per minute, and the latter two frequencies are assumed to be equal to the respiratory motion frequency which is about 12 cycles per minute.

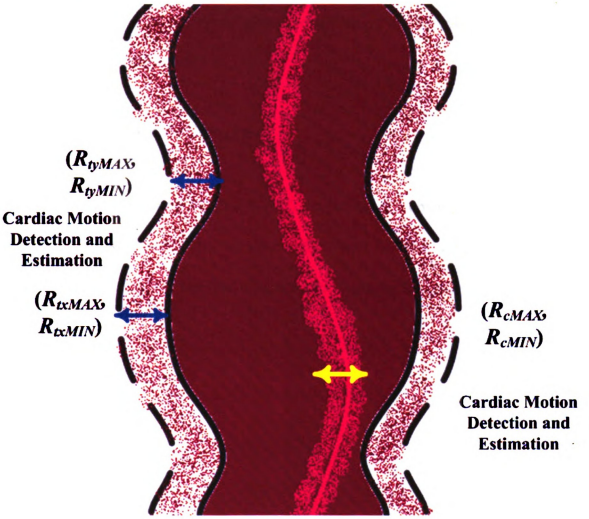


Figure 7.15 Illustration of motion encoded sinogram with motion detection and estimation

The motion-encoded sinogram is illustrated in Figure 7.15, in which the motion effects are exaggerated and shown as dotted region. The width of the motion-encoded region is estimated and the motion information is extracted.

There are several approaches to evaluate motion in sinogram space. In the $R_{MAX}$ and $R_{MIN}$ estimation and organ boundary detection, the maximum and minimum radius (amplitude of the motion) can be estimated according to the width of the motion blurred region in the sinogram.

## 7.9 Motion Effects on Sinogram

Mathematically, the sinogram data for 2D projection are obtained using Equation 7.13. For the sake of simplicity, we assume the object function $\rho(x, y)$ is a product of $f(x, y)$ and $s(x, y)$. The following derivations are for 2D sinogram only.

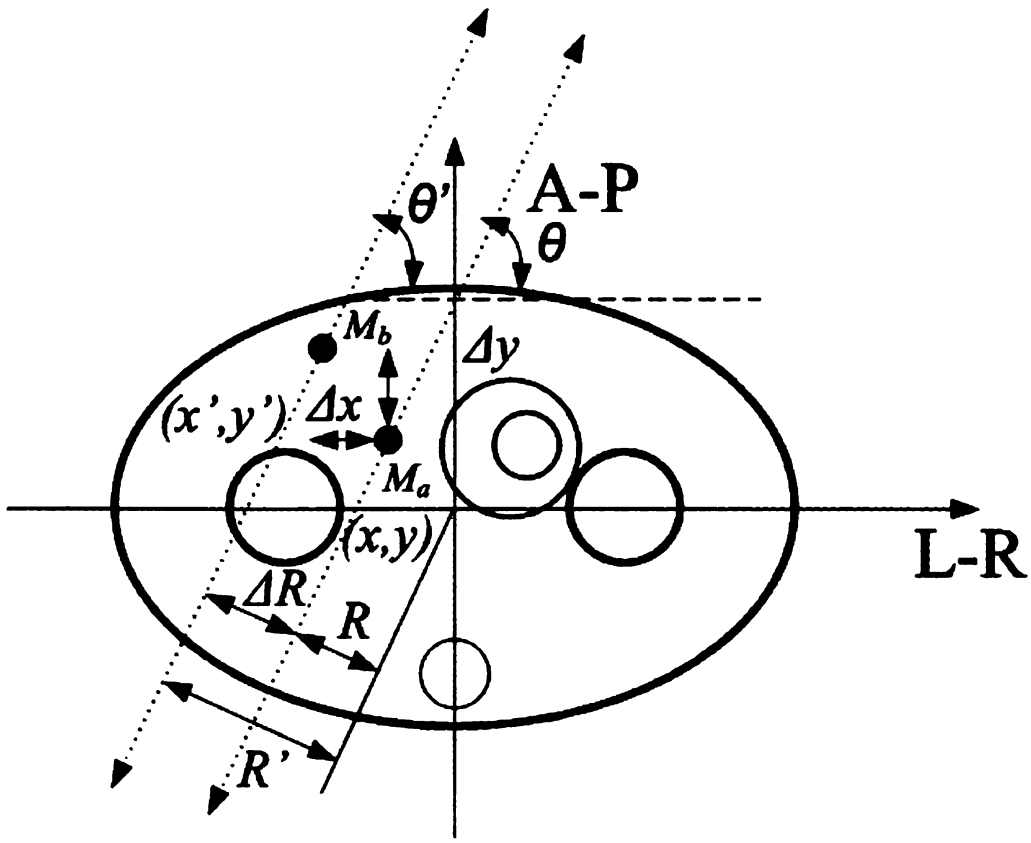


Figure 7.16 Mathematical parameters illustration for motion models

We start with one point at a spatial location $(x, y)$ on the moving organ of interest $M_a$. After a period of time, it is moved to a new location whose coordinates are represented by $(x', y') = (x + \Delta x, y + \Delta y)$ where $\Delta x$ and $\Delta y$ are the motion in L-R and A-P directions that need to be compensated. The corresponding sinograms are represented as $P(R, \theta)$ and $P(R', \theta')$ at two different times with the relationship as:

$$R = x\cos\theta + y\sin\theta \tag{7.18}$$

$$R' = (x + \Delta x)\cos\theta' + (y + \Delta y)\sin\theta' = R + \Delta R \tag{7.19}$$

By choosing $\theta = \theta'$ when sorting the sinogram data in the data acquisition process, the effect of motion reduces to simply scaling in trans-axial direction as:

$$\Delta R = \Delta x \cos\theta + \Delta y \sin\theta \tag{7.20}$$

For the points on the organs, the following relationship should also be satisfied:

$$\Delta B = \sqrt{K_x \cdot \Delta x^2 + K_y \cdot \Delta y^2} \tag{7.21}$$

where $K_x$ and $K_y$ depend on the shapes of organs only. $\Delta R$ and $\Delta B$ are the changes in spatial location and anatomical boundaries obtained using the fast CT protocol. From Equations 7.20 and 7.21, we can calculate the motion in the two dimensional space with the knowledge of motion-corrupted sinogram and CT scans or analytical Radon transform. The correction terms are expressed by Equation 7.22:

$$\{\Delta x, \Delta y\} = \Phi(\Delta \overline{R}, \Delta \overline{B}) \tag{7.22}$$

where $\Delta \overline{R}, \Delta \overline{B}$ are estimated using simulated motion corrupted sinogram and motion models hypothesized in Chapter 8. $\Phi$ is the function incorporating the mathematical operations presented in motion correction section.

## 7.10 Motion Synthesis Results

The torso phantom is discretized in 3D using brick elements in the solution domain

$\Omega$ with a resolution of 2.5 × 2.5 × 4 mm in the lateral, anterior-posterior and superior-inferior directions respectively.

Discretizing a complete respiratory cycle into twenty-one temporal phases, six phases of the lung motion in the first half cycle are shown in Figure 7.17 (exhalation minima to inhalation maxima). The radius of lungs $R_l$ varies from 40 mm to 90 mm in 10 mm steps. The radius of the heart outer wall $R_c$ is 40 mm with the vessel radius set to 20 mm. The chest wall radius is set to be 240 mm (L-R) and 160 mm (A-P). The spine cylinder is 20 mm in radius.

The material properties and attenuation coefficients are assigned appropriately in each object and surrounding air. The amount of radioactivity in each object and air are also defined so that the dose concentration in heart, bone, body, blood, lungs and air is in descending order. The trans-axial and azimuthal directions in the sinogram are grouped into 288 bins (720 mm FOV) and 360 bins (half circle FOV, $5^\circ \cdot bin^{-1}$). The number of bins determines the resolution in the sinogram space and hence the reconstruction resolution. The acceptance angle for the PET detector is set to be $5^\circ$ and minimum acceptance photon energy is 53 keV for a 511 keV emitted photon pair.

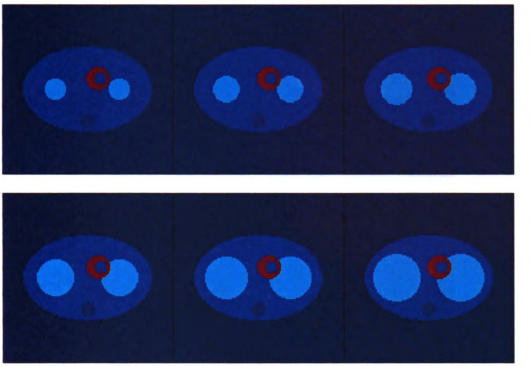

Figure 7. 17 Six respiratory phases with different lungs sizes for input phantom images: exhalation minima (upper left) and inhalation maxima (lower right)

Figure 7.18 Sliced simulation results from 3D model: (a)-(b) sinogram and (c) corresponding reconstructed images using FBP

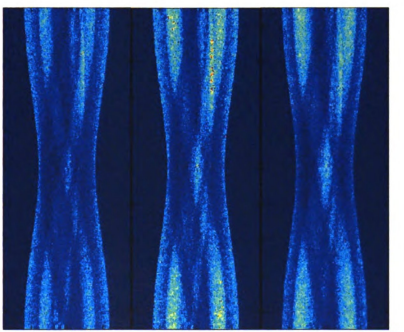

(a)

Figure 7.18 continued

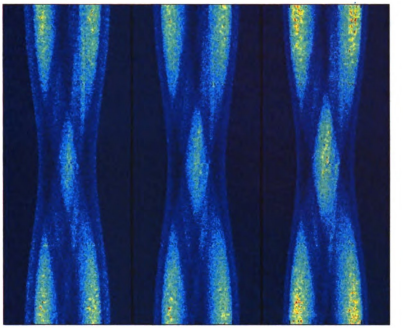

(b)

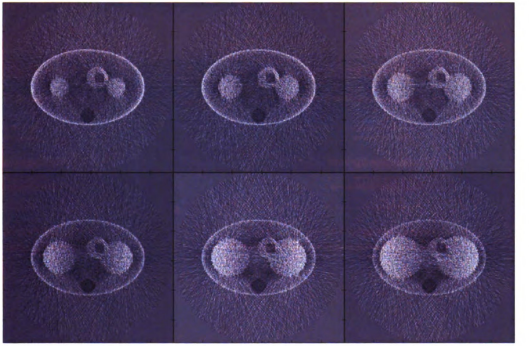

(c)

The reconstructed PET images using FBP are shown in Figure 7.18(b) with the corresponding sinogram data in Figure 7.18(a). The radioactivity concentration in the

lungs is artificially set to be high for the purpose of enhancing the motion effects in sinogram data. Attenuation correction has not been applied since only geometry dependent motion is of interest. It is clearly seen that pulmonary motion changes the pattern of sinogram intensity distribution derived in Section 7.9 in the trans-axial direction (R-axis). The torso-air boundaries in the sinogram remain the same since the chest wall was assumed to be static under the simplification hypothesis. The motion corrupted image is obtained by a weighted sum of all the sinograms at different phases for multiple cycles.

# CHAPTER 8. INVERSE PROBLEMS IN POSITRON EMISSION TOMOGRAPHY IMAGING

## 8.1 Introduction

Patient motion, including body movement, head movement and thoracic motion due to respiratory and cardiac cycles, is a major source of artifacts in nuclear medicine imaging [124][125][126][129][131][134][135]. In the past few years extensive research has been conducted for the purpose of motion correction for PET imaging [83][84][85][87][88][89][91][101][102][104][106][107][108][110][116][127][133] [138][139][140][146][147].

We propose a new approach to correct for thoracic motion in PET images using sinogram data in the projection space. This approach involves detecting motion components in the projection space and correcting them before image reconstruction is performed. This sinogram based method employs the entire projection data set, in contrast to the multiple acquisition frames (MAF) [127] and gating [101][116] methods, which involve time averaging for increasing the SNR. Once motion compensation is performed in sinogram space, standard reconstruction algorithms [15][143][144] can be applied to obtain a reconstructed image free from motion effects.

The methodology presented in this dissertation extends the motion correction in

projection space to 3D where the elastic organ deformation and thoracic motion are simulated using motion models presented in Chapter 7. The objective of this work is to not only compensate for motion in PET imaging but also retain the high SNR, which will benefit the subsequent diagnosis of lesions/tumors, treatment planning and therapy. For simplicity, in the later sections, we use the term "motion" to stand for "thoracic motion" unless we mention the specific motion type, such as respiratory, cardiac, body, or head motion.

## 8.2 PET imaging with motion

Thoracic motion effects on PET imaging data can be traced back to two types of sources: the cardiac cycle, namely, motion of heart at about 1 second per cycle and respiratory cycle, namely, motion of the organs in the abdominal region including lungs, stomach, liver and spleen. The period for the respiratory motion is about 5 seconds per cycle. Patients usually lie in the PET gantry for a few minutes, which is much longer than the cycle period. Consequently, the acquired PET data usually containing tens of millions of events are degraded by the thoracic motion. The "motion corrupted" PET image data leads to errors in diagnosis, treatment planning, dose estimation and subsequent therapy. In the worst case scenario a small tumor could go undetected due to blurring in the motion-corrupted images. Failure of early detection and diagnosis can in turn decrease the probability of therapy success. Also motion effects can cause error in estimating the stage of a tumor since the size of lesions and tumors are wrongly reconstructed without motion correction. Significant

volume changes of lung lesions were observed by Nehmen et al. leading to misdiagnosis [101]. In the fusion of PET and CT images investigated by Osman et al., mis-localizations of lesions and tumors were found to be due to motion [116]. The impact of motion can be reduced in several ways as reported in previous studies. In the case of respiratory motion there are several ways to diminish motion artifacts as discussed in Section 8.3. Typical motion artifacts are shown in Figure 8.1 [89].

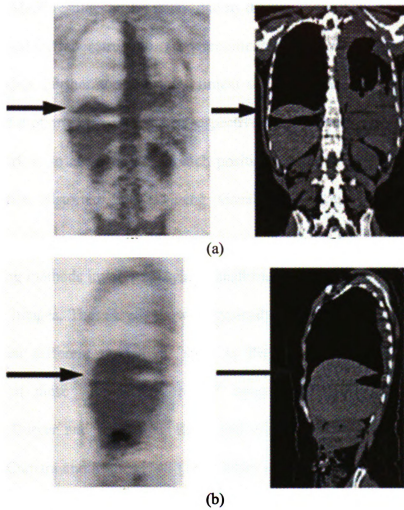


Figure 8.1 Motion artifacts in PET in comparison to CT images: (a) coronal view and (b) sagittal view

## 8.3 Current motion correction approaches

In the case of respiratory motion several methods to diminish motion artifacts have been reported in the previous studies with their associated advantages and limitations. Multiple acquisition frame (MAF) methods proposed by Picard and Thompson involve regrouping the projections into multiple subsets after detecting motion [127]. However the MAF results can be noisy due to the small numbers of projections in each frame, used for reconstruction. To overcome this problem, higher radiation dose might be needed. Furthermore, normal clinical setup does not allow acquisition of MAF data and motion correction in a retrospective way. One common approach used in clinical work is to acquire data in each position, multiple times and discard the apparent motion distorted images using visual examination by radiologists or technicians.

Post-processing methods involve applying transformations and image registrations on reconstructed images. These methods were typically proposed to improve the image fusion between different modalities, such as PET/CT, PET/MRI and the latest performance of these approaches for PET images can be found in [104][150] published by Berger and McGough. Rigid and affine transformations results were presented by Camara and Mattes [148][149]. More systematic introduction of nuclear medicine image registration in post-processing stage is found in Maintz [151] and Hill's review articles [152]. Post-processing methods in the image space, however, must be off-line and constrained by the time frames of reconstruction and registration algorithms. This procedure is time consuming due to the nonlinear, elastic nature of

organ and thoracic cavity deformation. The intrinsically distorted projection data used in subsequent reconstruction also render compensation techniques in post-processing stage unreliable.

Breath-hold methods which involve holding breath during data acquisition with fast imaging techniques [145][146] and new scanning protocols is an on-going research area and the latest techniques were just published by Nehmeh [147]. However, hold the breathing for long times can make patients uncomfortable; especially those subjects having lung lesions and/or respiratory complications.

Gating methods performs a respiratory-gated acquisition employing external signals dependent upon the state of respiration, e.g. abdominal belt, skin marker, etc. proposed by Nehmen et al. [101] and Visvikis et al. [116]. For cardiac motion, an external signal, e.g. the electrocardiagram (ECG) signal can be obtained simultaneously to perform a gated acquisition. The PET data for a heart beat cycle is stored in gated frames to eliminate the motion artifacts. Improvements in reducing the blurring due to motion using gating methods have been demonstrated. Gating with breathing cycle by tracking external source points situated over the patients and respiration correlated dynamic PET have been developed recently. Apparently, gating methods require a priori information on respiratory and cardiac cycles, which implies need for additional hardware and complex implementation and synchronization. A posteriori gating by estimating the respiratory frequency from acquired PET dynamic data was published by Visvikis [117]. By using the low number of events detected by ACD in a phase-of-interest in the entire cycle for image reconstruction, the image quality suffers from the low statistics like MAF as well.

Model-based motion compensation methods that incorporate motion models directly into the image reconstruction were studied by Jacobson and Fessler [84], Qiao [112], and Li [153] recently. Progresses of these techniques are published by Reyes [107]. The main problem in these approaches is the need for a 4D CT scan for constructing the motion model at each phase of the motion cycle. Further, these techniques are associated with the reconstruction algorithms rather than motion compensation in the projection space.

Recent research on the 5-dimensional (5D) models that incorporate two more independent variables, i.e. tidal volume and breathing air flow besides the three spatial dimensions are developed at Washington University in St. Louis School of Medicine. This approach has been validated for computed tomography (CT) studies, also referred to as 5-D CT [154] where motion correction for PET imaging research is undergoing.

## 8.4 Motion Correction in Projection Space

The overview of the motion correction scheme is shown in Figure 8.2. The methods proposed in this dissertation are depicted in the center box of this scheme figure. The filtered back projection is implemented for sinogram projection data correction. The iterative expectation maximization (EM) reconstruction methods will be implemented for further list-mode projection data correction (See Chapter 9 Conclusions and Future work).

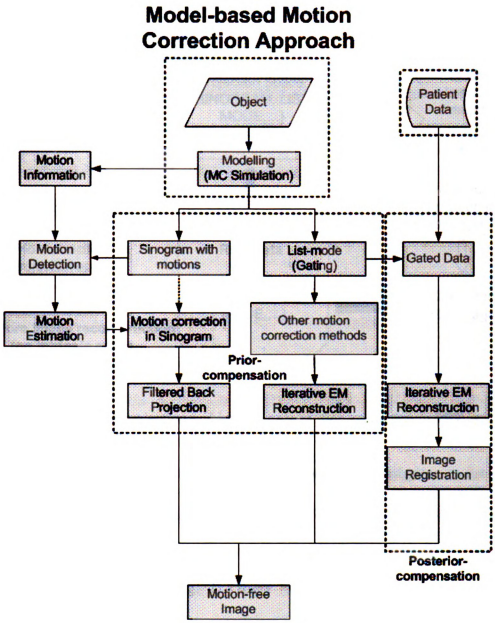


Figure 8.2 Overview of motion correction scheme

To overcome the limitations of existing motion correction techniques, this dissertation proposes an innovative projection space correction approach prior to reconstruction. A schematic of the proposed approach contrasted with image space correction approach is illustrated in Figure 8.3.

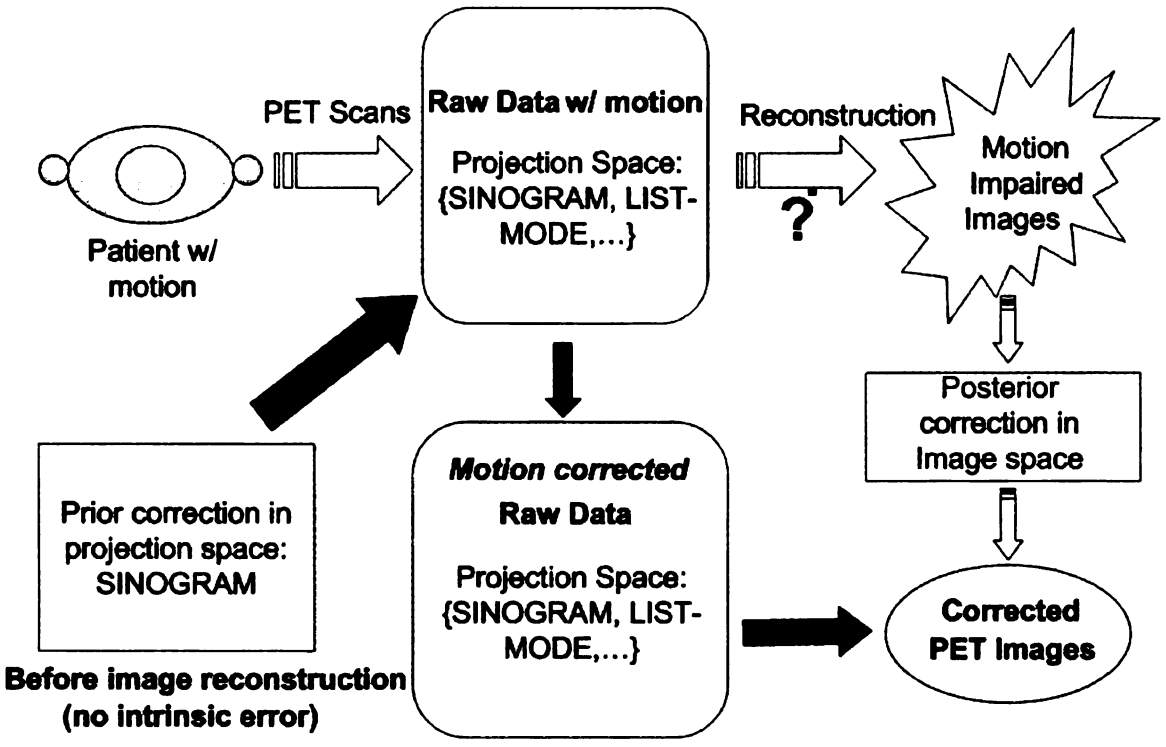


Figure 8.3 Schematic of projection and image space motion correction in PET imaging

Compensating for motion in the raw data/projection space (sinogram or list mode), has several advantages: 1) Implementing the processing algorithms in PET scanner hardware can make this approach fast and potentially real time in contrast to image space registration and processing; 2) Offers higher accuracy since intrinsic errors introduced in image reconstruction is eliminated; 3) In contrast to the gating techniques, correction in projection space retains the full statistics and thus improves the image resolution and target to background (T/B) ratio levels. Particularly, cancer imaging, tumor detection or delineation applications will be enhanced using this approach.

## 8.5 Motion Tracking, Estimation and Extraction

To understand the motion better, we introduce some fiducial points with 3D radius equals to 5mm × 5mm × 4mm that are attached to the lung-blood interface. In order to track the motion in both L-R and A-P directions, three fiducial points $f_a$, $f_b$, and $f_c$ are assigned as illustrated in Figure 8.4, in which the distance from the phantom center to the lung center is $D_l$ and the lung radius is $R_l$.

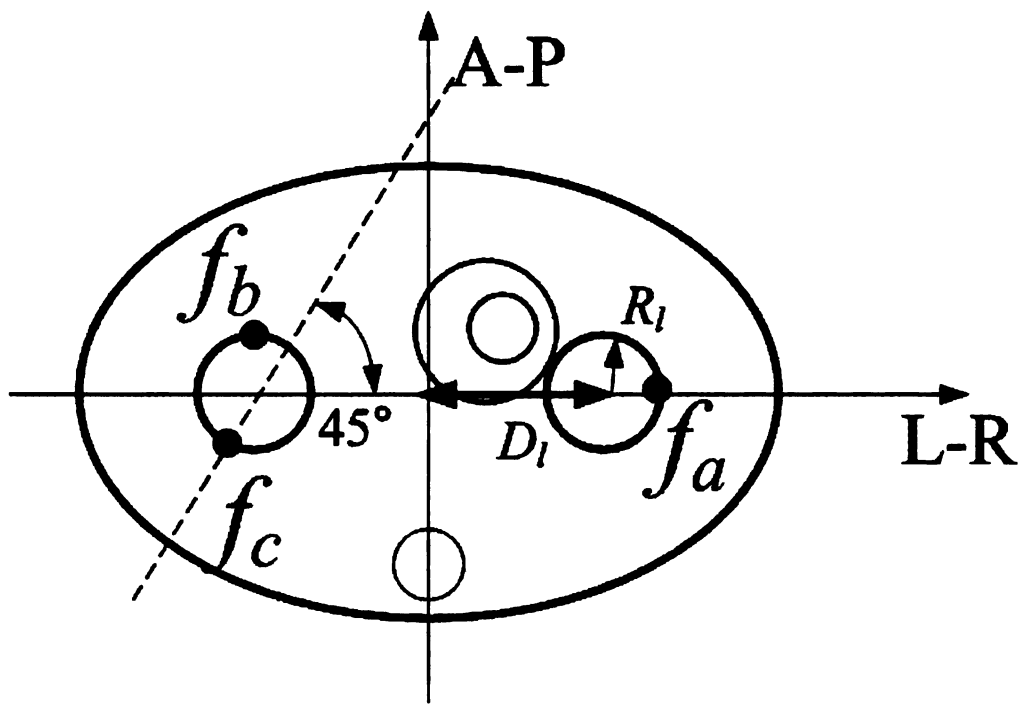


Figure 8.4 Fiducial points allocation for motion tracking

Since in most practical reconstructions, 3D PET volumetric data also needs to be approximately rebinned into a 2D format, it is reasonable to assume that no fiducial point is needed in the S-I direction (i.e. for out-of-plane motion). The coordinates (L-R, A-P, S-I) for the fiducial points used in this dissertation are obtained as follows:

$$f_a = (D_l + R_l, 0, 0) \tag{8.1}$$

$$f_b = (-D_l, R_l, 0) \tag{8.2}$$

$$f_c = (-D_l - R_l \cos 45^\circ, -R_l \sin 45^\circ, 0) \tag{8.3}$$

The simulation result with fiducial points $\{f_a, f_b, f_c\}$ is shown in Figure 8.5, in which the radioactivity at these points are set to be relatively high. The tracking of lung motion in the sinogram shown in Figure 7.16 can be simplified to tracking of the high-intensity pixels associated with the fiducial points. The motion pattern is estimated and extracted such that $\Delta\overline{R}, \Delta\overline{B}$ in Equation 7.19 can be predicted.

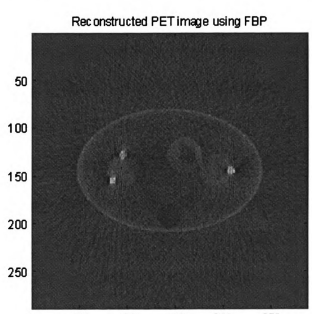


Figure 8.5 Reconstructed image with fiducial points for motion tracking and estimation

Motion extraction in sinogram is based on prior information providing the starting point for searching motion, as illustrated in Figure 8.6. The analytical Radon transform is used to generate the sinogram of just fiducial points using Equation 7.13. Fast CT acquisition protocol, namely, the breath-hold helical CT scans that offer rich anatomical information which provides "landmarks" that serve the same purpose as fiducial points used in these studies. Figure 8.6(a) is the simulated prediction for the three fiducial points in one particular breathing phase that is obtained using fast Radon projection method. The correlated PET sinogram data is shown in Figure 8.6(b), in which lines of strong intensity indicate the locations of the fiducial points. It is clearly demonstrated that the prior information obtained using CT can serve as a reasonable starting point for motion tracking. We adopted fast Radon transform simulation in our study to mimic the fast CT acquisitions. By incorporating more motion phases and information, boundaries of the organ of interest can be estimated using fast radon transform simulator. Figure 8.7 shows the effect of motion on the sonogram; Figure 8.7(a) is obtained by considering just two phases, i.e. extreme inhalation and exhalation time instances and Figure 8.7(b) is obtained with twenty-one phases characterizing the full respiratory cycle. The intensity distribution of the sinogram not only reveals the boundaries of organs but also provides the information for further compensation in the same projection space. The motion blurring effect is clearly seen in Figure 8.7(b) at the outer boundaries of the bands, which is due to the motion at the organ-blood interface.

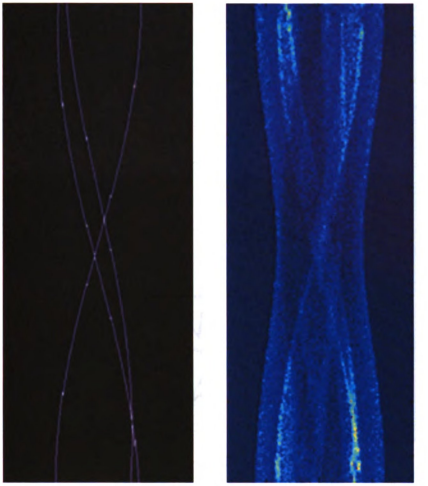

(a) (b)

Figure 8.6 Motion extraction in sinogram based on prior information obtained using fast Radon transform result in (a) and high intensity extraction in simulated sinogram (b)

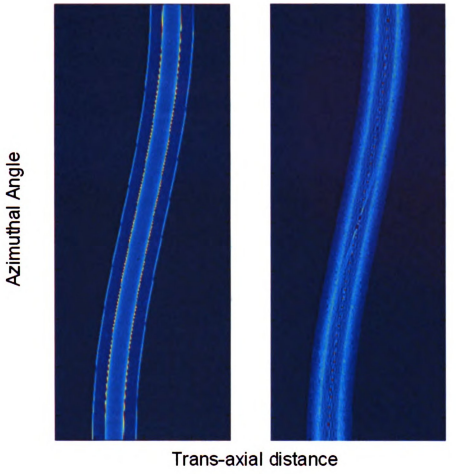


Figure 8.7 Motion effect estimation in sinogram for right lung PET image in noise-free case

Once the organ of interest is defined, e.g. the right lung in Figure 8.7, the radon transform simulator and MC simulator results are combined using maximum correlation method to provide motion corrupted organ boundary $\hat{M}$, reference organ boundary $\hat{S}$ and the center for the ROI $\hat{R}_c$. To simplify the mathematical equations, $\hat{M}$, $\hat{S}$, and $\hat{R}_c$ are all integer numbers and defined as fraction of the total length trans-axial distance vector (number of data points in the $R$ direction of sinogram projection space).

For different azimuthal angles in the sinogram, the estimated boundaries and center coordinates are different. In the following derivations, the angle dependent term is omitted but actually the estimated variables $\hat{M}$, $\hat{S}$, and $\hat{R}_c$ are all functions of azimuthal angle, i.e. $\hat{M}(\theta)$, $\hat{S}(\theta)$ and $\hat{R}_c(\theta)$. For an angle $\theta_i$, the intensity plots in the motion corrupted and reference projection are illustrated by the dashed-line and solid-line respectively in Figure 8.8.

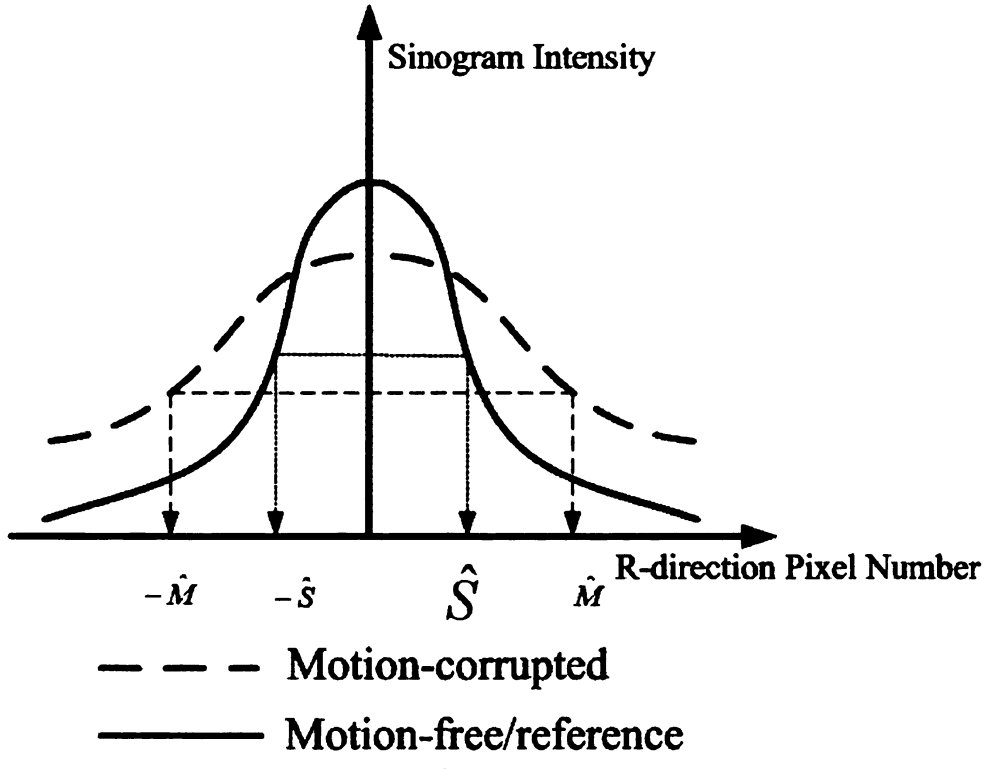


Figure 8.8 Illustration of the line plots of motion-corrupted and motion-free sinogram intensity with boundaries estimation labeled

## 8.6 Motion Correction Implementation and Results

Let the reference sinogram (target), motion-corrupted sinogram and motion-corrected

sinogram be represented as $P(R,\theta)$, $\tilde{P}(R,\theta)$ and $\hat{P}(R,\theta)$ respectively. The resolutions in the trans-axial distance direction ($R$ direction of sinogram projection space) are denoted as $\Delta R$ and $\Delta\tilde{R}$ for reference and motion-corrupted sinogram. The width of ROI in the above two cases are easily obtained when $\Delta\overline{B}$ is estimated by equations 8.4 and 8.5:

$$W = 2\Delta R\hat{S} \tag{8.4}$$

$$\tilde{W} = 2\Delta\tilde{R}\hat{M} \tag{8.5}$$

Since $\hat{M}$ and $\hat{S}$ are integers representing the motion-corrupted and reference ROI boundaries, we can label each data point in projection space from center to the boundaries as $j = 1,2,...,\hat{M}-1$ and $k = 1,2,...,\hat{S}-1$. Since we discretized the range of azimuthal angle (projection angel) ($-90^\circ$ to $90^\circ$) into $N_A$ bins, we can represent any pixel intensity in the sinogram as $P_{\theta_i}(R_j)$ or $P_{\theta_i}(R_k)$, where $i = 1,2,...,N_A$.

The motion correction algorithm can be expressed in a closed form function shown in Equation 8.6 for each projection angle $\theta_i$:

$$\hat{P}_{\theta_i}(R_{\hat{S}-k}) = \tilde{P}_{\theta_i}\left(\frac{W}{\tilde{W}-W}\cdot R_j\right) + \Delta P_{\theta_i,\hat{M}-j} \tag{8.6}$$

Substitute Equation 8.4 and 8.5 into Equation 8.7 and we get (derived in Section 8.8).

$$\hat{P}_{\theta_i}(R_{\hat{S}-k}) = \tilde{P}_{\theta_i}\left(\frac{\Delta R \cdot \hat{S}}{\Delta \hat{R} \cdot \hat{M} - \Delta R \cdot \hat{S}} \cdot R_j\right) + \tilde{P}_{\theta_i}(R_j) - \frac{1}{N}\sum_{l=0}^{N-1}\tilde{P}_{\theta_i}(R_{M-j+l}) \tag{8.7}$$

where $j = \left|\frac{\hat{M}-1}{\hat{S}-1} \cdot k\right|$ and $|\bullet|$ is the rounding operator to get closest integers. The first term involves a scaling operation and mapping from the corrupted sinogram to the target one. The averaging term $\frac{1}{N}\sum_{l=0}^{N-1}\tilde{P}_{\theta_i}(R_{M-j+l})$ is applied to make sure the corrected sinogram intensity distribution is smooth. Additional details and pseudo codes for the correction algorithm are attached in the Appendix.

Typical sinogram images before and after motion correction are shown in Figure 8.9(a) and 8.9(b), respectively. The sinogram intensity is smeared with wider ROI as shown in figure 8.9(a) which is due to the cumulative motion effects in the respiratory cycles. The corresponding reconstructed images are shown in Figure 8.10.

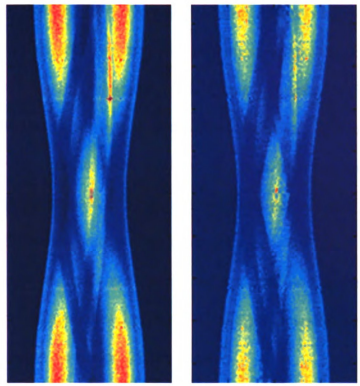

(a) (b)

Figure 8.9 Sinogram before and after the motion correction. The cumulative motion effects with widen ROI can be seen in (a) due to five cycles of respiration simulated

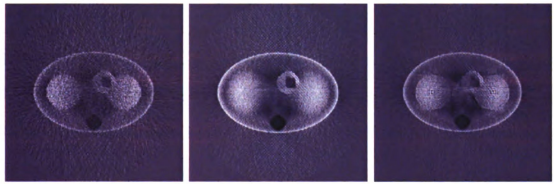

Figure 8.10 Reconstructed PET images: (a) target image at one particular respiratory phase, (b) motion blurred image and (c) corrected image using the scaling-mapping algorithm

The reference/target image is shown in Figure 8.10(a). Figure 8.10(b) and 8.10(c) are motion-corrupted image after five cycles of respiration and motion-corrected image using the scaling-mapping algorithm. The image blurring effect is clearly demonstrated by the model. It should also be mentioned that additional procedures were conducted in the image space, such as image de-blurring, non-linear image registration, etc for the purpose of better anatomical delineation and multi-modality image fusion. The scaling-mapping method presented here not only performs innovative motion tracking, estimation and extraction, but also overcomes difficulties in the image space manipulation and preserves clear organ boundaries by reducing the motion contamination in the raw projection space.

## 8.7 Discussion and Conclusion

There are several issues and practical constraints of the proposed algorithm that deserve to be mentioned:

1) Standardized uptake value (SUV) Accuracy

The SUV accuracy is achieved by the conservation law, i.e. keeping the sorted photon pairs number constant, for the radioactive event counts in the sinogram. The SUV based on patient's body weight is the most common parameter extracted from nuclear medicine images for quantitative evaluation, which is related to the injected dose per body mass and defined in Equation 8.8.

$$SUV_{bw} = \frac{C(t)}{InjectedDose/PatientsWeight}$$

(8.8)

where $C(t)$ is the tissue radioactivity concentration in kBq/ml at time t. The patient motion introduces the artifacts that decrease the tissue radioactivity concentration term which can be demonstrated by the spreading effect of the corrupted sinogram in Figure 8.9(a). Using the prior-correction method and the conservation law by maintaining the total radioactive event counts in one scanning session, the SUV is the same or is very close to that of motion-free images taken with patient holding breath. This is one advantage for the correction in projection space because it is difficult to manipulate the image pixel intensity in image space to get the accurate estimate of SUV.

2) Residual Artifacts

Some residual artifacts can still be seen in the projection space corrected image in Figure 8.10(c) on the reconstructed organ boundaries and the low intensity region in the image center. A possible reason for these artifacts might be due to the Filtered Back Projection (FBP) method used. A more accurate but time consuming iterative reconstruction algorithm such as Expectation Maximization (EM) iterative reconstructions need to be investigated to reduce the residual artifacts.

3) 3D Volumetric Data

In real applications we encounter 3D volumetric data. The 3D PET acquisition with the inter-slice septa removed greatly increases the scanner sensitivity and image signal to noise ratio (SNR). The patient motion is inherently in three dimensions and the 3D radioactive isotope distribution results in the 3D projection data. However,

since the computational load for 3D data processing is much greater than that of 2D, this requires use of rebinning. The method for converting the projections from 3D data into 2D approximations is widely used and one sinogram per transverse slice is obtained. The out-of-plane motion tracking and estimation is simplified in this dissertation by in-plane motion using three fiducial points tracking. The fully 3D iterative approaches are also available and the out-of-plane motion correction is expected to be taken care of in the list-mode space.

## 8.8 Scaling-mapping method pseudo codes

The derivation of motion correction algorithm and its pseudo codes are attached here.

LOOP A: FOR $i = 1,2,...,N_A$

LOOP B: FOR $j = 1,2,...,\hat{M}-1$

Intensity difference at jth R direction pixel in motion-corrupted sinogram (updating step calculated in Equation 8.9)

$$\Delta P_{\theta_i,\hat{M}-j} = \tilde{P}_{\theta_i}(R_j) - \frac{1}{N}\sum_{l=0}^{N-1}\tilde{P}_{\theta_i}(R_{\hat{M}-j+l}) \tag{8.9}$$

LOOP C: for $k = 1,2,...,\hat{S}-1$

Updating target sinogram by linear mapping pixels from motion-corrupted space to reference space by equation (8.10):

$$j = \left| \frac{\hat{M} - 1}{\hat{S} - 1} \cdot k \right|$$

(8.10)

Corrected projection data is calculated as equation 8.11 as:

$$\hat{P}_{\theta_i}(R_{\hat{S}-k}) = \tilde{P}_{\theta_i}\left(\frac{W}{\tilde{W} - W} \cdot R_j\right) + \Delta P_{\theta_i, \hat{M}-j}$$

(8.11)

END LOOP C (Trans-axial correction)

IF $\frac{W}{\tilde{W} - W} \cdot R_j < \hat{S}$

CONTINUE (Forced to end Loop B)

END LOOP B

END LOOP A (Azimuthal correction)

Equation 8.11 can also be rewritten using all the known quantities in a closed-form as:

$$\hat{P}_{\theta_i}(R_{\hat{S}-k}) = \tilde{P}_{\theta_i}\left(\frac{W}{\tilde{W} - W} \cdot R_j\right) + \Delta P_{\theta_i, \hat{M}-j}$$

$$= \tilde{P}_{\theta_i}\left(\frac{\Delta R \cdot \hat{S}}{\Delta \hat{R} \cdot \hat{M} - \Delta R \cdot \hat{S}} \cdot R_j\right) + \tilde{P}_{\theta_i}(R_j) - \frac{1}{N}\sum_{l=0}^{N-1} \tilde{P}_{\theta_i}(R_{M-j+l})$$

(8.12)

where $j = \left| \frac{\hat{M} - 1}{\hat{S} - 1} \cdot k \right|$ and $\lfloor \bullet \rfloor$ is the rounding operator to get closest integers.

# CHAPTER 9. CONCLUSIONS AND FUTURE WORK

## 9.1 Accomplishments and Conclusions

(a) Formulated a general mathematical model-based approach for noninvasive imaging in NDE and biomedical application

(b) Implemented qualitative and quantitative image analysis procedures

(c) Developed computational models for simulating MOI and GMR NDE techniques. Used these models to conduct a parametric study for optimization of sensors and systems

(d) Results of parametric study and data classification algorithms were used in estimating Probability of Detection (POD) curves for the NDE techniques

(e) Developed computational models based on Monte Carlo (MC) technique for simulating PET imaging

(f) Developed and incorporated motion models into the MC-PET model

(g) Developed motion compensation techniques for correction in sinogram space

## 9.2 Future Work

In this dissertation, a new patient motion compensation method in projection space-the sinogram is proposed and initial results validate this approach using Monte Carlo simulation that incorporates respiratory motion. Innovative motion tracking, estimation, and extraction is presented with the knowledge of prior anatomical

information and forward Radon transform. The respiratory motion artifacts are significantly reduced by correcting the motion of each 2D sliced image from the entire 3D volumetric PET data after rebinning procedure. Future work is needed to improve the reconstructed image quality by using the iterative reconstruction algorithms with huge size list-mode data. More realistic motion models need to be tested so the robustness of this approach can be evaluated.

Besides the organ boundary extraction and detection based correction, there are other approaches need to be investiaged: a) Sinogram stratification and motion frequency estimation. The sinogram is possibly stratified into different layers based on the intensity. Due to the higher intensity in the sinogram data means more appearances of the organ (dose distribution). The motion frequency is able to be estimated based on the intensity distribution of the blurred regions; b) Gradient-based method for motion vector estimation. In this method, the motion vectors also need to be estimated using gradient-based method if the stratification of sinogram is correct and accurate; c) List-mode based motion correction methods. Since projection data is stored as list-mode, which is large in size, efficient methods need to be proposed to process and correct the motion in list-mode. The list mode data can be simply treated as "time tagged" projection data, so it can also be converted into sinogram and then corrected.

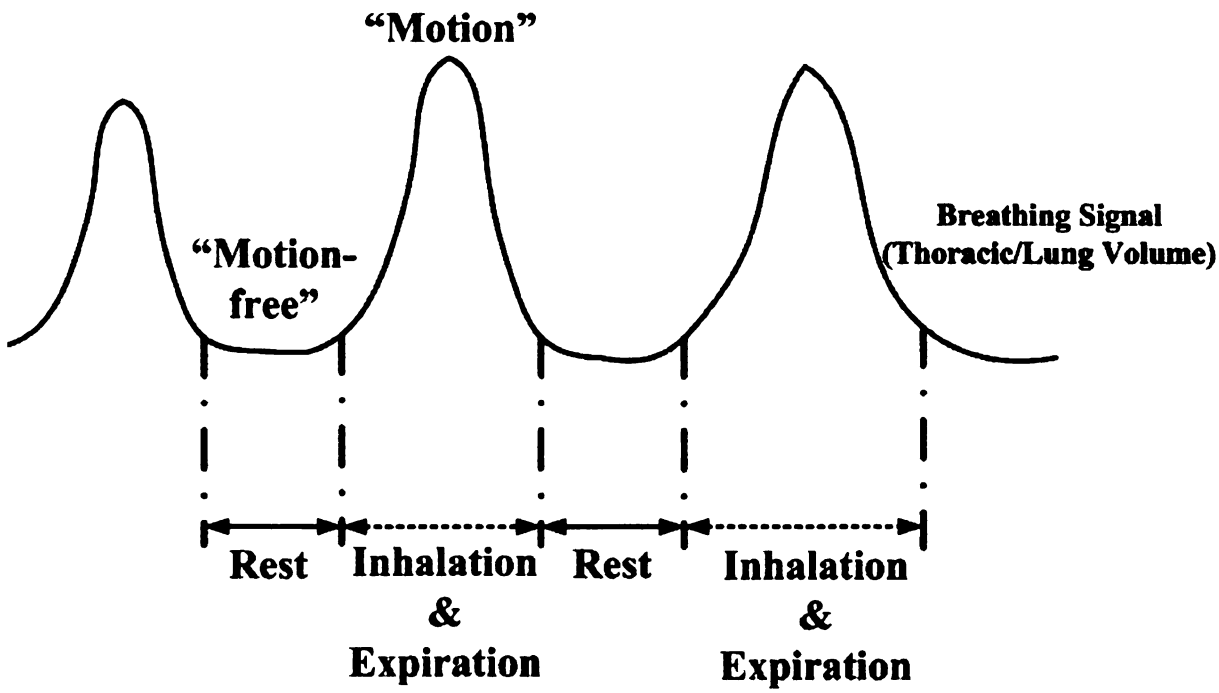


Figure 9.1 List-mode correction using rest motion phase

When the list-mode data is acquired with some external hardware, which can output the breathing signal, it can be corrected by only averaging the "motion-free" part of data, as we can see in Figure 8.11. The rest duration is about one half of the whole respiratory cycle, and the "motion-free" data can be averaged after the start and end time of this rest periods are detected. The inhalation and expiration phase data of the breathing cycle needs to be discarded.

The other future work includes:

(a) EM imaging sensors and system optimization through POD studies.

(b) More quantitative feature extraction for EM imaging data.

(c) More accurate motion models development to describe the patient motion not limited in the lungs and heart, but extended to upper abdominal regions.

(d) Quantitative comparison of motion correction methods between sinogram approach and current correction results through commercial software and real patient data.

(e) Model-based attenuation correction for PET/CT after motion correction.

# REFERENCES


[1] A. Webb, Introduction to Biomedical Imaging, Wiley-Interscience, 2003.

[2] R. C. Gonzalez, and R. E. Woods, Digital Image Processing, 2nd Ed., Prentice Hall, 2002.

[3] J. T. Bushberg et al., The Essential Physics of Medical Imaging, 2nd Ed., Lippincott Williams & Wilkins, 2002.

[4] M. Bertero et al., Introduction to Inverse Problems in imaging, Institute of Physics Publishing, Bristol and Philadelphia, 1998.

[5] C. T. A. Johnk, Engineering Electromagnetic Fields and Waves, 2nd Ed., John Wiley & Sons, 1976.

[6] N. N. Rao, Elements of Engineering Electromagnetics, Prentice Hall, 2000.

[7] http://www.jlab.org

[8] http://en.wikipedia.org/wiki/Positron_emission_tomography

[9] J. B. West, Respiratory physiology: The Essentials, 6th Ed., Lippincott Williams & Wilkins, 2000.

[10] J. Thibaud, L'annihilation des positrons au contact de la matiere et la radiation qiu en resulte, *C R Acad Sci*, 197(1933), 1629-1632.

[11] F. Joliot, Preuve experimentale de l'annihilation des electons positives, *C R Acad Sci*, 197(1933), 1622-1625.

[12] R. Beringer, et al., *Phys. Rev.* 61(1942), 222.

[13] J. Mitchell, Applications of recent advances in nuclear physics to medicine, *Brit. J. Radiol.*, 19(1946), 481-497.

[14] C. Tobias et al., The elimination of carbon monoxide from the body with refernce to the possible conversion of CO to CO2, *Amer. J. Physiol.*, 145(1945), 253-263.

[15] P. E. Valk, Positron Emission Tomography: Basic Science and Clinical Practice, P. E. Valk, D. L. Bailey, et al. (eds.), Springer, 2003.

[16] N. A. Dyson et al., The preparation and use of Oxygen-15 with particular reference to its value in the study of pulmonary malfunction, 1958 Peaceful Uses of Atomic Energy, Geneva, 1958, 103-115.

[17] C. T. Dollery, Metabolism of oxygen-15, *Nature*, 189(1960), 1121.

[18] H. Anger, Scintillation camera and positron camera in: Medical Radioisotope Scanning, Vienna: IAEA, (1959), 59-73.

[19] S. Rankowitz et al., Positron scanner for locating brain tumors, *IRE International Convention Record*, 10(1962), 49.

[20] Y. L. Yamamoto et al., Study of quantitative assessment of section microregional blood flow in man by multipole positron detecting system using Krypton-79, BNL Med. Dept. Circ. Brookhaven, Report no. 28, 1966.

[21] D. E. Kuhl et al., Image separation radioisotope scanning, *Radiology*, 80(1963), 653-662.

[22] D. E. Kuhl et al., Quantitative section scanning using orthogonal tangent correction, *J. Nucl. Med.*, 14(1973), 196-200.

[23] D. A. Chesler et al., Transverse section imaging of myocardium with 13NH4, *J. Nucl. Med.* 14(1973), 623.

[24] M. M. Ter-Pogossian et al., A positron emissin transaxial tomograph for nuclear imaging, *Radiology,* 114(1975), 89-98.

[25] M. E. Phelps et al., Application of annihilation coincidence detection to transaxial reconstruction tomography, *J. Nucl. Med.*, 16(1975), 210-224.

[26] N. A. Dyson, The annihilation coincidence method of localizing positron emitting isotopes and a comparison with parallel counting, *Phy. Med. Biol.*, 4(1960), 376-390.

[27] G.L. Fitzpatrick, Flaw Imaging in Ferrous and Nonferrous Materials Using Magneto-Optic Visualization, U.S. Patents 4,625,167, 4,755,752, 5,053,704 and associated foreign patents.

[28] G.L. Fitzpatrick et al., Magneto-optic/Eddy Current Imaging of Aging Aircraft: a New NDI Technique, *Material evaluation*, 1993, 1402-1407.

[29] G.L. Fitzpatrick et al., Magneto-Optic/Eddy Current Imaging of Subsurface Corrosion and Fatigue Cracks in Aging Aircraft, *Review of Progress in Quantitative Nondestructive Evaluation*, 15(1996).

[30] K. Zvezdin and V. A. Kotov, Modern magneto-optics and magneto-optical materials, Institute of Physical Publishing, Bristol and Philadelphia, 1997.

[31] P. Ramuhalli et al., Enhancement of magneto-optic images, The 9th International Workshop on Electromagnetic Nondestructive Evaluation, Saclay, France, 2003, 199-205.

[32] U. Park, L. Udpa, G. C. Stockman, Motion-based Filtering of Magneto-Optic Imagers, *Image and Vision Computing*, 2004, 243-249.

[33] U. Park, L. Udpa, G. C. Stockman, B. Shih, J. Fitzpatrick, Real-time Implementation of Motion-based Filtering in Magneto-Optic Imager, 30th Annual Review of Progress in Quantitative Nondestructive Evaluation, Green bay, Wisconsin, 2003.

[34] L. G. Shapiro, G. C. Stockman, Computer Vision, Prentice Hall, 2001.

[35] Y. Fan et al., Automated rivet inspection for aging aircraft with magneto-optic imager, *Electromagnetic Nondestructive Evaluation (IX), IOS Press*, 2005, 185-194.

[36] Y. Deng et al., Automatic classification of MOI for aircraft rivet inspection, Proceedings of 12th International Symposium on Applied Electromagnetics and Mechanics, Bad Gastein, Austria, 2005.

[37] S. Udpa, L. Udpa, "Eddy Current Nondestructive Evaluation," Encyclopedia of Electrical and Electronics Engineering, John G. Webster, Editor, John Wiley, 1999

[38] S. Udpa, Nondestructive Testing Handbook, Electromagnetic Testing, American Society for Nondestructive Testing, Technical Editor, Columbus, 2004

[39] J. Salon and J. Schneider, "A Comparison of Boundary Integral and Finite Element Formulations of the Eddy Current Problems," *IEEE Transactions on Power Systems*, 100(1981), 1473-1479

[40] N. Ida, Numerical Modeling for Electromagnetic Non-Destructive Evaluation Chapman & Hall, McGraw Hill, 1984

[41] O. Rübenkönig, The Finite Difference Method (FDM) - An Introduction, Albert Ludwigs University of Freiburg, 2006

[42] Y. K. Na and M. A. Franklin, "Detection of subsurface flaws in metals with GMR sensors," *Review Of Progress in Quantitative Nondestructive Evaluation*, 760(2005), 1600-1607.

[43] L. Xuan, "Finite Element and Meshless Methods in NDT Applications," Ph. D Dissertation, Iowa State University, 2002

[44] Paul Rutherford, Boeing Phantom Works, Seattle, WA

[45] J. Jin, The Finite Element Method in Electromagnetics, New Your: Wiley, 2002

[46] Y. Tian et al., Simulation of the world federation's first eddy current benchmark problem," *Review Of Progress in Quantitative Nondestructive Evaluation*, 700(2004), 1560-1566

[47] Z. Zeng et al., "Probability of Detection Model for Gas Transmission Pipeline Inspection", *Research in Nondestructive Evaluation* 3(2004).

[48] L. Xuan et al., "Developments of a Meshless Finite Element Model for NDE

Applications," Proceedings of the 29th Annual Review of Progress in Quantitative Nondestructive Evaluation, Bellingham, WA, 2002

[49] Z. Zeng et al., "Modeling microwave NDE using the element-free Galerkin method," *Electromagnetic Nondestructive Evaluation (IX)*, IOS Process, 2005, 41-48

[50] L. N. Trefethen and D. Bau, Numerical Linear Algebra, SIAM, 1997

[51] T. Dogaru and S. T. Smith, *IEEE. Trans. Magn.* 37(2001), 3831-3838.

[52] T. Dogaru et al., Deep crack detection around fastener holes in airplane multi-layered structures using GMR-based eddy current probes," in *Review of Progress in QNDE*, NY 700(2004), 398-405.

[53] A. Jander, C. Smith and R. Schneide, Magnetoresistive Sensors for Nondestructive Evaluation, in 10th SPIE International Symposium, 2005.

[54] N. Nair, V. Melapudi, H. Jimenez, X. Liu, Y. Deng, Z. Zeng, L. Udpa, T. Moran and S. Udpa, *IEEE. Trans. Magn.* 42(2006), 3312-3314.

[55] L. Xuan et al, "Finite Element Model for MOI Applications Using A-v Formulation," *Review of Progress in Quantitative Nondestructive Evaluation*, 557(2001), 385-391.

[56] G. L. Fitzpatrick, "Imaging Near Surface Flaws in Ferromagnetic Materials Using Magneto-Optic Detectors," *Review of Progress in Quantitative Nondestructive Evaluation*, 1985.

[57] R. Albanese et al, A Comparative Study of Finite Element Models for Magneto Optic Imaging Applications, 6th International Workshop on Electromagnetic Nondestructive Evaluation, Budapest, Hungary, 2000.

[58] Z. Zeng et al., Application of Taguchi Methodology for Optimizing Test Parameters in Magneto-Optic Imaging, Proceedings of the 29th Annual Review of Progress in Quantitative Nondestructive Evaluation, 22(2003), 651-658.

[59] B. E. C. Koltenbah, "Demodulation Algorithm for the Boeing Magnetoresistive Sensors Program", Boeing Physical Sciences Research Center.

[60] T. Belytschko, Y. Krongauz, D. Organ, M. Fleming, and P. Krysl, "Meshless methods: an overview and recent developments," *Comput. Methods Appl. Mech. and Engr.*, 139(1996), 3-47.

[61] J. Dolbow and T. Belytschko, "An introduction to programming the meshless element free Galerkin method," *Archives in Computational Mechanics*, 5(1998), 207-241.

[62] L. Xuan, Z. Zeng, B. Shanker, and L. Udpa, Element-free Galerkin method for static and quasi-static electromagnetic field computation, *IEEE Trans Magn.*, 40(2004), 12-20.

[63] S. C. Strother, et al., Measuring PET scanner sensitivity: relating countrates to image signal-to-noise ratios using noise equivalent counts, *IEEE Trans Nucl. Sci.*, 37(1990), 783-788.

[64] CW. Williams, et al., Design and performance characteristics of a positron emission computed axial tomography-ECAT-II, *IEEE Trans Nucl. Sci.*, 1979, 619-627.

[65] L. Lupton and N. Keller, Performance Study of Single Slice Positron Emission Tomography Scanners by Monte Carlo Techniques, *IEEE Trans on Med. Imag.* 2(1983), 154-167.

[66] H. Zaidi, Relevance of accurate Monte Carlo modeling in nuclear medical imaging, *Med. Phys.* 26(1999), 574-608.

[67] http://www.bme.unc.edu/~wsegars/NCAT_instructions.htm

[68] http://depts.washington.edu/simset/html/user_guide/user_guide_index.html

[69] C. J. Thompson, J. Moreno-Cantu and Y. Picard, PETSIM: Monte Carlo simulation of all sensitivity and resolution parameters of cylindrical positron imaging systems, *Phys. Med. Biol.*, 37(1992), 731-749.

[70] M. Ljungberg, et al., Monte Carlo Calculations in Nuclear Medicine: Applications in diagnostic imaging, Institute of Physics Publishing, Bristol and Philadelphia, 1998.

[71] H. Kahn, Use of different Monte Carlo sampling techniques, Monte Carlo Methods, H. A. Meyer (edited), Wiley, New York, 1956.

[72] D. E. Raeside, Monte Carlo principles and applications, *Phys. Med. Biol.*, 21(1976), 181-197.

[73] R. L. Morin, Monte Carlo Simulation in the radiological sciences, CRC, Boca Raton, FL, 1988.

[74] I. Lux, et al., Monte Carlo Particle Transport Methods: Neutron and Photon Calculations, Chemical Rubber Company, Boca Raton, FL, 1991.

[75] R. Lewitt and S. Matej, Overview of Methods for Image Reconstruction from Projections in Emission Computed Tomography, *Proceedings of the IEEE*, 91(2003), 1588-1611.

[76] S. Vandenberghe, et. al., Reconstruction of 2D PET data with Monte Carlo generated system matrix for generalized natural pixels, *Phys. Med. Biol.*, 51(2006), 3105-3125.

[77] M. Defrise, et al., Image Reconstruction Algorithms in PET, Positron Emission Tomography: Basic Science and Clinical Practice, P. E. Valk, D. L. Bailey, et al. (eds.), Springer, 4(2003), 91-114.

[78] G. Marsaglia and A. Zaman, Some portable very-long-period random number generators, *Comput. Phys.* 8(1994), 117–121.

[79] http://opengatecollaboration.healthgrid.org/

[80] http://www.gehealthcare.com/

[81] S. Deans, The Radon Transforms and some of it applications, Wiley, New York, 1983.

[82] W. Lu et al., Tomographic motion detection and correction directly in sinogram space, *Phys. Med. Biol.*, 47(2002), 1267-1284.

[83] P. Bruyant, et al., Correction of the respiratory motion of the heart by tracking of the center of mass of thresholded projections: a simulation study using the dynamic MCAT phantom, *IEEE Trans. Nucl. Sci.*, 49(2003), 2159-2166.

[84] M. Jacobson, et al., Joint estimation of image and deformation parameters in motion-corrected PET, *IEEE Nucl. Sci. Symp. Conf. Rec.* 5(2003), 3290-3294.

[85] A. Rahmim, et al., Motion compensation in histogram-mode and list-mode reconstructions: beyond the event-driven approach, *IEEE Trans. Nucl. Sci.* 51(2004), 2588–2596.

[86] F. Lamare, et al., Incorporation of elastic transformations in list-mode based reconstruction for respiratory motion correction in PET, *IEEE Nucl. Sci. Symp. Conf. Rec.* 3(2005), 1740-1744.

[87] L. Liveratos, et al., Rigid-body transformation of list-mode projection data for respiratory motion correction in cardiac PET, *Phys. Med. Biol.* 50(2005), 3313-3322.

[88] B. Thorndyke, et al., Reducing respiratory motion artifacts in positron emission tomography through retrospective stacking, *Med. Phys.* 33(2006), 2632-2641.

[89] M. Dawood, et al., Lung motion correction on respiratory gated 3-D PET/CT images, *IEEE Trans. Med. Imaging* 25(2006), 476-485.

[90] T. Li, et al., Model-based image reconstruction for four-dimensional PET, *Med. Phys.* 33 (2006), 1288-1298.

[91] F. Lamare, et al., Respiratory motion correction for PET oncology applications using affine transformation of list mode data, *Phys. Med. Biol.* 52(2007), 121-140.

[92] W.P. Segars. Development of a new dynamic NURBS-based cardiac-torso (NCAT) phantom., PhD dissertation, The University of North Carolina, May 2001.

[93] C. J. Groiselle, et al., Monte-Carlo Simulation of the Photodetection Systems Prototype PET Scanner Using GATE: A Validation Study, 2004 IEEE Nuclear Science Symposium Conference, 5(2004), 3130-3132.

[94] J. C. Yanch, et al., Physically realistic Monte Carlo simulation of source, collimator and tomographic data acquisition for emisssion computed tomography, *Phys. Med. Biol.* 37(1992), 853-870.

[95] Y. K. Dewaraja, et al., 3-D Monte Carlo-Based Scatter Compensation in Quantitative I-131 SPECT Reconstruction, *IEEE Trans. Nucl. Sci.*, 53(2006), 181-188.

[96] G. W. Goerres, et al., PET-CT image co-registration in the thorax: influence of respiration, *Eur. J. Nucl. Med. Mol. Imaging* 29(2002), 351-360.

[97] J. Kybic, et al., Fast parametric elastic image registration, *IEEE Trans. Image Processing,* 12(2003), 1427-1442.

[98] F. Lamare, et al., Validation of a Monte Carlo simulation of the Philips Allegro/GEMINI PET systems using GATE, *Phys. Med. Biol.* 51(2006), 943-962.

[99] J. R. McClelland, et al., A continuous 4D motion model from multiple respiratory cycles for use in lung radiotherapy, *Med. Phys.* 33(2006), 3348–3358.

[100] S. A. Nehmeh, et al., Four-dimensional (4D) PET/CT imaging of the thorax, *Med. Phys.* 31(2004), 3179–3186.

[101] S. A. Nehmeh et al, Effect of respiratory gating on quantifying PET images of lung cancer, *J. Nucl. Med.*, 43(2002), 876-881.

[102] S. A. Nehmeh et al, Reduction of respiratory motion artifacts in PET imaging of lung cancer by respiratory correlation dynamic PET: Methohology and comparison with respiratory gated PET, *J. Nucl. Med.*, 44(2003), 1644-1648.

[103] M. Osman et al, Clinically significant inaccurate localization of lesions with PET/CT: frequency in 300 patients, *J. Nucl. Med.*, 30(2003), 240-243.

[104] K. Berger, K. Khurshid, R. McGough, J. L. Seamans. CTAC Misregistration in PET/CT Cardiac Imaging: Correction with a Dedicated CTAC/PET Alignment Visualization Application, and Automated Registration Algorithm, and ECG- Gated CTAC. 12th Annual American Society of Nuclear Cardiology Scientific Session, San Diego, CA, 2007.

[105] T. Pan, et al., Attenuation correction of PET images with respiration-averaged CT images in PET/CT, *J. Nucl. Med.* 46(2005), 1481–1487.

[106] J. Qi, et al., List Mode reconstruction for PET with motion compensation: a simulation study, *Proc. IEEE Int. Symp. Biomed. Imaging*, 2002, 413–416.

[107] M. Reyes et al, Model-based respiratory motion compensation for emission tomography image, reconstruction, *Phys. Med. Biol.*, 52(2007), 3579-3600.

[108] M. Reyes et al, Respiratory motion correction in emission tomography image

reconstruction, MICCAI 2005, J. Duncan and G. Gerig (Eds.), 2005, 369-376.

[109] W. Lu et al, Motion-encoded dose calculation through fluence/sinogram modification, *Med. Phys.* 31(1), 2005, 118-127.

[110] W. Lu et al, Reduction of motion blurring artifacts using respiratory gated CT in sinogram space: A quantitative evaluation, *Med. Phys.*, 32(11), 2005, 3295-3304.

[111] F. Qiao et al, Region of interest motion compensation for PET image reconstruction, *Phys. Med. Biol.*, 52(2007), 2675-2689.

[112] F. Qiao, et al., A motion-incorporated reconstruction method for gated PET studies, *Phys. Med. Biol.* 51(2006), 3769–3783.

[113] A. Reader, et al., One-pass list-mode EM algorithm for high-resolution 3D PET image reconstruction into large array, *IEEE Trans. Nucl. Sci.* 49(2002), 693–699.

[114] H. Schoder, et al., Clinical implications of different image reconstruction parameters for interpretation of whole-body PET studies in cancer patients, *J. Nucl. Med.* 45(2004), 559–566.

[115] W. Segars, et al., Modelling respiratory mechanics in the MCAT and spline-based MCAT phantoms, *IEEE Trans. Nucl. Sci.* 48(2001), 89–97.

[116]D. Visvikis et al, A posteriori respiratory motion gating of dynamic pet images, *IEEE Nucl. Sci. Symp.* Conf. Rec., 5(2003), 3276-3280.

[117] D. Visvikis, et al., Evaluation of respiratory motion effects in comparison with other parameters affecting PET image quality, *IEEE Nucl. Sci. Symp.Conf. Rec.* 6(2004), 3668–3672.

[118] L. A. Shepp and Y. Vardi, Maximum likelihood reconstruction for emission tomography, *IEEE Trans. Med. Img.*, 2(1982), 113-122.

[119] P. J. Green, Bayesian reconstructions from emission tomography data using a modified EM algorithm, *IEEE Trans. Med. Img.* 9(1), 1990, 84-93.

[120] H. M. Hudson et al, Accelerated image reconstruction using ordered subsets of projection data, *IEEE Trans. Med. Img.*, 13(4), 1994, 601-609.

[121] http://www.owlnet.rice.edu/~elec539/Projects97/cult/report.html

[122] D. Visvikis, et al., Influence of OSEM and segmented attenuation correction in the calculation of standardised uptake values for [18F] FDG PET, *Eur. J. Nucl. Med.* 28(2001), 1326–1335.

[123] J. M. Ollinger, Model-based scatter correction for fully 3D PET, *Phys. Med. Biol.* 41(1996), 153-176.

[124] A. Gottschalk, P. V. Harper, F. F. Jimenez, and J. P. Petasnick, "Quantification of the respiratory scanning with the rectilinear focused collimator scanner and the gamma scintillation camera," *J. Nucl. Med.*, 7(1966), 243–251.

[125] M. V. Green, J. Seidel, S. D. Stein, T. E. Tedder, K. M. Kempner, C. Kertzman, and T. A. Zeffiro, "Head movement in normal subjects during simulated PET brain imaging with and without head restraint," *J. Nucl. Med.*, 35(1994), 1538–1546.

[126] M. Menke, M. S. Atkins, and K. R. Buckley, "Compensation methods for head motion detected during PET imaging," *IEEE Trans. Nucl. Sci.*, 43(1996), 310–317.

[127] Y. Picard, and C. J. Thompson, "Motion Correction of PET Images Using Multiple Acquisition Frames," *IEEE Trans. Medical Imaging*, 16(1997), 137-144.

[128] P. E. Kinahan, D. W. Townsend, T. Beyer, and D. Sashin, "Attenuation correction for a combined 3D PET/CT scanner', *Med. Phys.*, 25(1998), 2046-2053.

[129] B.M.W. Tsui, W.P. Segars, and D.S. Lalush, "Effects of Upward Creep and Respiratory Motion in Myocardial SPECT," *IEEE Trans. Nucl. Sci.*, 47(2000), 1192-1195.

[130] P. P. Bruyant et al., "Correction of the Respiratory Motion of the Heart by Tracking of the Center of Mass of Thresholded Projections: A Simulation Study Using the Dynamic MCAT Phantom," *IEEE Trans. Nucl. Sci.*, 49(2002), 2159-2166.

[131] DR Gilland, BA Mair, JE Bowsher, and RJ Jaszczak. Simultaneous reconstruction and motion estimation for gated cardiac ECT. *IEEE Trans. Nucl. Sci.*, 49(2002), 2344–2349.

[132] R. R. Fulton et al., "Correction for Head Movements in Positron Emission Tomography Using an Optical Motion-Tracking System," *IEEE Trans. Nucl. Sci.*, 49(2002), 116-123.

[133] W. Lu et al., "Tomographic motion detection and correction directly in sinogram space," *Phys. Med. Biol.*, 47(2002), 1267-1284.

[134] S. S. Vedam et al., "Quantifying the predictability of diaphragm motion during respiration with a noninvasive external marker," *Med. Phys.*, 30(2003), 505-513.

[135] M. Osman et al, "Clinically significant inaccurate localization of lesions with PET/CT: frequency in 300 patients," *J. Nucl. Med.*, 30(2003), 240-243.

[136] Cao et al., "Three-dimensional motion estimation with image reconstruction for gated cardiac ECT," *IEEE Trans. Nucl. Sci.*, vol. 50, pp. 384-388, 2003.

[137] Paul Bühler, Uwe Just, Edmund Will, Jörg Kotzerke, and Jörg van den Hoff, "An Accurate Method for Correction of Head Movement in PET," *IEEE Trans. Medical Imaging*, 23(2004), 1176-1185.

[138] E. Gravier and Y. Yang, "Motion-compensated reconstruction of tomographic image sequences," *IEEE Tran. Nucl. Sci.*, 52(2005), 51-56.

[139] W. Lu et al., "Reduction of motion blurring artifacts using respiratory gated CT in sinogram space: A quantitative evaluation," *Med. Phys.*, 32(2005), 3295-3304.

[140] R. Zeng et al., "Respiratory motion estimation from slowly rotating x-ray projections: Theory and simulation," *Med. Phys.*, 32(2005), 984-991.

[141] F. Lamare et al. "List-mode-based reconstruction for respiratory motion correction in PET using non-rigid body transformations," *Phys. Med. Biol.*, 52(2007), 5187-5204.

[142] R. Zeng et al., "Estimating 3-D Respiratory Motion From Orbiting Views by Tomographic Image Registration," *IEEE Trans. Medical Imaging*, 26(2007), 153-161.

[143] R. L. Wahl et al., Principles and Practice of Positron Emission Tomography, Lippincott Williams & Wilkins, 2002.

[144] D. L. Bailey et al., Positron Emission Tomography: Basic Sciences, Springer-Verlag London Limited, 2005.

[145] D. Mah et al., "Technical aspects of the deep inspiration breath-hold technique in the treatment of thoracic cancer," *Int J Radiat Oncol Biol Phys,* 48(2000), 1175-1185.

[146] K. E. Sixel et al., "Deep inspiration breath hold to reduce irradiated heart volume in breast cancer patients," *Int J Radiat Oncol Biol Phys,* 49(2001), 199-204.

[147] S. A. Nehmeh et al., "Deep-Inspiration Breath-Hold PET/CT of the Thorax," *J. Nucl. Med.*, 48(2007), 22-26.

[148] O. Camara et al., "Evaluation of a thoracic elastic registration method using anatomical constraints in oncology", 2nd. Joint Conf. of the IEEE Engineering in Medicine and Biology Society, 2002.

[149] Mattes D, Haynor D, Vesselle H, Lewellen T and Eubank W, PET-CT image registration in the chest using free-form deformations, *IEEE Trans. Med. Imaging,* 22(2003), 120-128.

[150] K. Khurshid et al., "Automated cardiac motion compensation in PET/CT for accurate reconstruction of PET myocardial perfusion images," *Phys. Med. Biol.*, 53(2008), 5705-5718.

[151] J. B. A. Maintz et al., "A survey of medical imaging registration," *Medical Image Analysis*, 2(1998), 1-37.

[152] D. L. G. Hill et al., "Medical image registration," *Phys. Med. Biol.*, 46(2001), 1-45.

[153] T. Li, et al., "Model-based image reconstruction for four-dimensional PET," *Med.*

*Phys.*, 33(2006), 1288-1298.

[154] D. A. Low et al., "Novel breathing motion model for radiotherapy," *Int. J. of Rad. Onc. Bio. Phys.*, 63(2005), 921-929.

[155] Y. Deng et al., "A Monte Carlo model for positron emission tomography imaging," *Int. J. of Appl. Electrom.*, 28(2008), 79-85.

[156] R. L. Harrison et al., "A public-domain simulation system for emission tomography: photon tracking through heterogeneous attenuation using importance sampling," *J. Nucl Med.*, 34(1993), 60P.

[157] H. Anger, Scintillation camera and positron camera in: Medical Radioisotope Scanning, Vienna: IAEA, (1959), 59-73.

[158] CW. Williams, et al., Design and performance characteristics of a positron emission computed axial tomography-ECAT-II, *IEEE Trans Nucl Sci*, 1979, 619-627.

[159] L. Lupton and N. Keller, Performance Study of Single –Slice Positron Emission Tomography Scanners by Monte Carlo Techniques, *IEEE Trans on Med. Imag.* 2(1983), 154-167.

[160] R. Lewitt and S. Matej, Overview of Methods for Image Reconstruction from Projections in Emission Computed Tomography, *Proceedings of the IEEE,* 91(2003), 1588-1611.

[161] S. Vandenberghe, et. al., Reconstruction of 2D PET data with Monte Carlo generated system matrix for generalized natural pixels, *Phys. Med. Biol.*, 51(2006), 3105-3125.

[162] M. Defrise, et al., 4-Image Reconstruction Algorithms in PET, Positron Emission Tomography: Basic Science and Clinical Practice, P. E. Valk, D. L. Bailey, et al. (eds.), Springer, 4(2003), 91-114.

[163] G. Marsaglia and A. Zaman, Some portable very-long-period random number generators, *Comput. Phys.* 8(1994), 117–121.